Università degli Studi di Pavia
Dottorato di Ricerca in Fisica - xxx Ciclo

A Model for the Fast and Accurate Dose Evaluation in Hadrontherapy

Alessia Embriaco

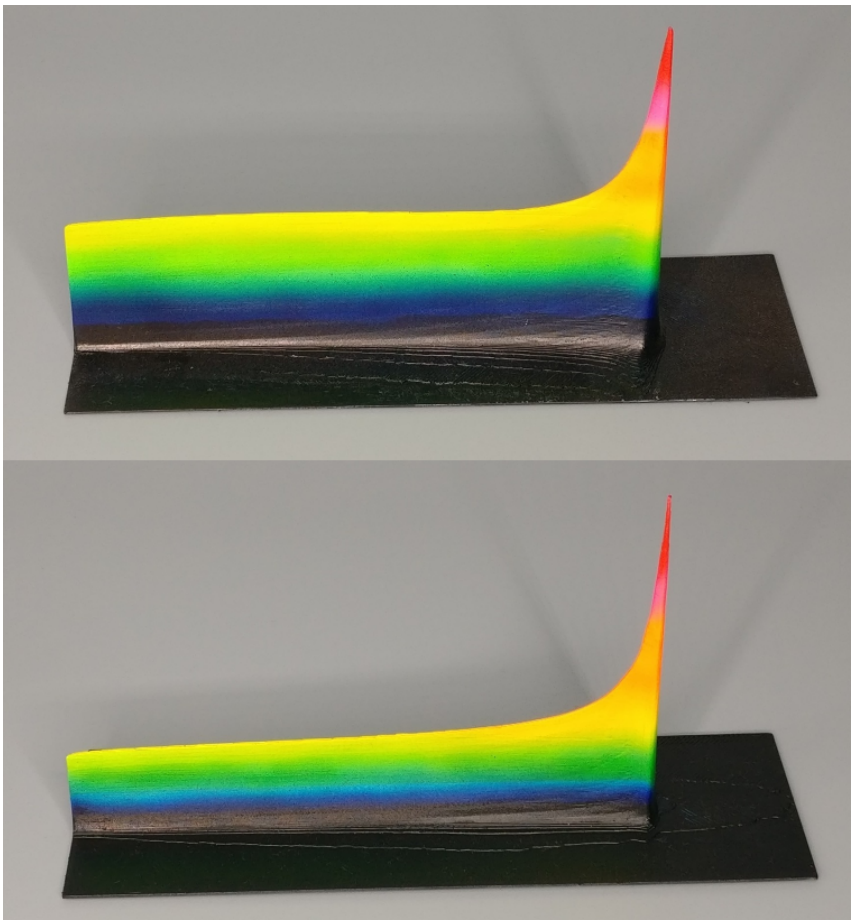

Tesi per il conseguimento del titolo

Full Title:
A Model for the Fast and Accurate Dose Evaluation in Hadrontherapy

Alessia Embriaco

2018

University of Pavia

Department of Physics

Istituto Nazionale di Fisica Nucleare

Dottorato di Ricerca in Fisica - XXX Ciclo

A Model for the Fast and Accurate Dose Evaluation in Hadrontherapy

dissertation submitted by

Alessia Embriaco

Submitted to the Graduate School in Physics in partial fulfillment of the requirements for the degree of

DOTTORE DI RICERCA IN FISICA
DOCTOR OF PHILOSOPHY IN PHYSICS

Supervisor: Prof. Alberto Rotondi (University of Pavia)

Referee: Prof. Paolo Russo (University of Naples)

Referee: Dr. Francesca Fiorini (University of Oxford)

Cover: Three-dimensional prints of the energy deposited in water by proton (top) and He (bottom) beams obtained by a Monte Carlo calculation with FLUKA (courtesy of Andrea Fontana, INFN-Pavia).

A Model for the Fast and Accurate Dose Evaluation in Hadrontherapy
Alessia Embriaco
PhD thesis - University of Pavia
Pavia, Italy, January 2018

Sotto l'azzurro fitto del cielo
qualche uccello di mare se ne va;
né sosta mai: perché tutte le immagini portano scritto
"più in là".

Eugenio Montale
Maestrale, Ossi di seppia (1925)

Contents

Introduction

Radiation therapy is currently one of the most promising techniques in the cancer treatments. Given the success and effectiveness of hadrontherapy, in the past decades the use of heavy particles as projectiles, in particular protons and carbon ions, has gained popularity and the number of centers is growing around the world.
However, hadrontherapy requires a good knowledge of the physical interactions of the particles and continuous efforts to develop and improve tools for treatment planning.
Monte Carlo simulations are considered the gold standard for accurate computations, but the high computation time limits their application in the clinical practice. As alternative, a number of analytical models has been developed in the past to try to reduce the calculation time: they are now widely used in clinical applications, due to their acceptable accuracy and computation time.
The most common approach is the pencil beam algorithm, where the dose can be divided into a central axis and an off axis term. In general, the pencil beam algorithm uses pre-calculated look-up tables for the depth dose evaluation, while the lateral profile is modelled with a Gaussian or double Gaussian distribution.
In this context, we propose a new model developed at the University of Pavia and the INFN Pavia Unit. The model, called MONET (MOdel of ioN dosE for Therapy), evaluates the three-dimensional (3D) energy deposition distribution for protons in a water phantom. In this work, the code is extended to calculate the energy distribution of Helium ions and renamed MONETα.
MONET evaluates the lateral and longitudinal terms starting from first principles.
For the lateral profile, it is based on the Molière theory of multiple Coulomb scattering, considering the energy loss and the effects of compounds. The nuclear interactions are added using a Cauchy Lorentz parametrization, obtained through the fit of FLUKA simulations. For the passage from the projected to a two-dimensional (2D) lateral distribution, an algorithm, that allows in the case of cylindrical symmetry to reconstruct the radial distribution starting from the projected one, has been implemented.

For the longitudinal profile, a new calculation of the average energy loss has been implemented. The calculation of the straggling is based on the convolution of energy loss with a Gaussian distribution, while the nuclear contributions are included using a linear parametrization.
The total energy distribution is evaluated in a 3D mesh by calculating at each depth the 2D lateral profile and by scaling it at the value of the energy deposition.
The results of the MONET code for protons and Helium ions are compared with FLUKA, which is currently used in many hadrontherapy centers and is continuously validated with experimental data. Based on the comparison with simulations, we can conclude that MONET is an accurate tool for the evaluation of the energy deposition for proton and Helium ions in water.
The first chapter of the thesis presents the advantages of hadrontherapy with a focus on the most common dose evaluation tools used in treatment planning.
The second chapter contains the implementation of the lateral model for protons and ^4He ions. MONET is based on the Molière theory of multiple Coulomb scattering and a Cauchy Lorentz parametrization for the nuclear interactions.
In the third chapter, the evaluation of the depth dose distribution will be presented considering the average energy loss, the straggling effects and the nuclear interactions.
In the fourth chapter, the results obtained with the MONET code for the energy deposition of a proton beam are compared with the FLUKA simulation in case of single Gaussian beam. Finally, the dose deposition in a lateral scan will be evaluated in order to simulate a more realistic case. In this case, the results of field size factor test will be compared to the FLUKA one.
In the fifth chapter, the results of MONETα and the FLUKA simulation for ^4He ions will be shown, considering again the single Gaussian beam and the field size factor test in case of a lateral scan.
In the last Chapter, the conclusion and the future perspectives of this PhD project will be presented.

Chapter 1

Physical Modelling for Particle Therapy

In this chapter, the attention will be on the importance of the development and improvement of analytical algorithms for treatment planning.
In the first section, the rationale of hadrontherapy will be shown focusing on the physical and biological advantages of heavy particles compared with photons. Thereafter, an overview of the motivations of using charged particle used for therapy will be presented, focusing in particular protons and ^4He ions.
In the second part of the chapter, a review on the most common dose evaluation tools for treatment planning will be presented.
Among these, I will also introduce the MONET code, which is the results of the studies presented in the thesis.

1.1 Hadrontherapy

Radiation therapy is one of the key tools in the fight against cancer. Approximately 2/3 of the patients are treated with radiotherapy, over 80% is irradiated with X ray. Only about 0.8% of the patients are treated with charged particles, but their number is increasing [5]. In the past decades, hadrontherapy gained popularity in cancer therapy. From 1954 to 2014, the number of patient treatments with charged particle is about 137000: 87% with protons, 11% with Carbon ions and the remaining with Helium ions, pions and other ions [1].
The idea of using charged particle was introduced by Robert R. Wilson in a paper entitled "Radiological use of fast protons" in 1946. The advantage of using heavy particles is due to their depth-dose profile (Fig. 1.1): the energy deposited increases with depth and reaches a distinct peak named Bragg peak, at the end of their range. The Bragg peak position can be changed by the initial kinetic energy of the beam: this feature can be used to optimize the conformity of the dose with a great reduction of the total dose out of target. In the treatment plan, the Bragg peak must be extended to cover the whole

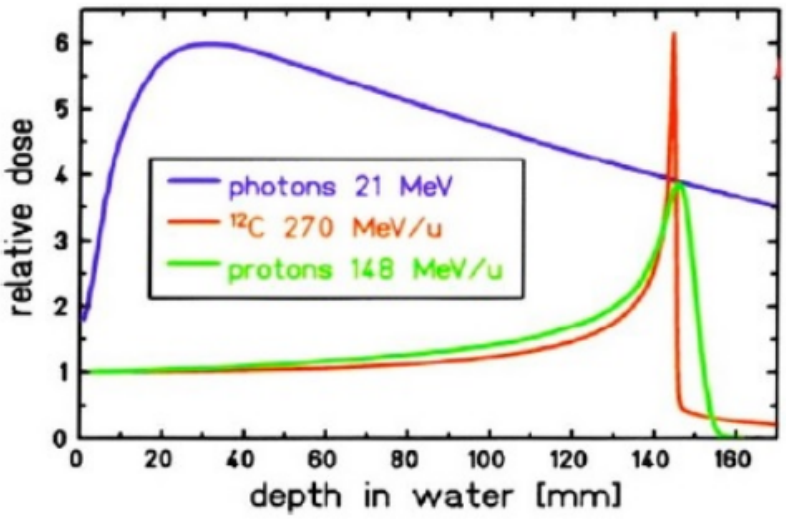

Figure 1.1: Depth dose distribution [2]: comparison between photons, protons and carbon ions in water.

cancer volume (Fig. 1.2), producing the so called SOBP (Spread Out Bragg Peak). This structure can be created by passive modulation of the primary beam or by changing the energy in the active beam scanning.
In conventional radiotherapy, it is necessary to irradiate the patient from many different angles to increase the dose to the tumor and to minimize it in the normal tissue. The IMRT (Intensity Modulated RadioTherapy) is the most advanced delivery technique for X ray with an excellent tumor coverage, but also the healthy tissues receive a non negligible dose. On the contrary, only few beams are necessary in hadrontherapy, limiting the dose to the healthy tissue.

1.1.1 Physics of hadrontherapy

The study of the interaction of heavy particles with human tissue is essential for the optimization of the dose in the target volume. When a therapeutic ion beam passes through the body of a patient, the main physical interactions are:

- the electromagnetic interactions, which generate the characteristic energy deposition and a broadening lateral profile,
- the nuclear interactions, which produce a wealth of secondary particles, primarily electrons, protons but also ions.

The longitudinal profile is mainly dominated by the inelastic collision with atomic electrons, while the lateral profile is determined by the elastic scattering on target nuclei. The nuclear interactions reduce the fluence of the primary

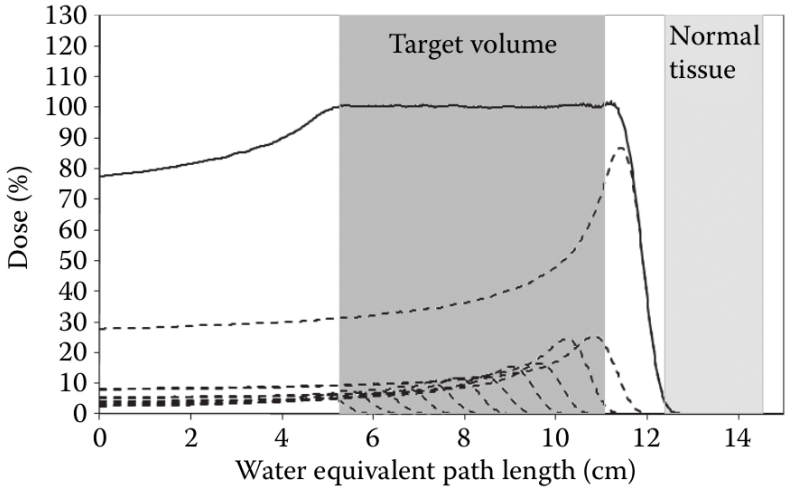

Figure 1.2: From [3]: Spread Out Bragg Peak (SOBP) depth–dose distribution (solid line), showing the component Bragg peaks (dashed lines).

particles and contribute both to longitudinal and lateral profiles. These interaction create target fragments, which give a contribution to the dose. For particles heavier than protons, also the fragmentation of the projectile is possible. These fragments have a velocity similar to that of the primary particle, but having lower mass and higher range, they generate a longitudinal tail after the Bragg peak. The angular distribution of the fragments is narrow in the primary beam direction and only the lighter among them contributes to the tail of lateral profile. The lateral penumbra can be reduced by increasing the mass of the ion.

For the application of charged particle to cancer treatment, it is necessary that these processes are understood and modelled with high accuracy.

1.1.2 Biological effects of hadrontherapy

The biological effects of radiation result principally from damage to DNA, which is the critical target in a cell. There is substantial evidence that the damage to the DNA molecules is decisive for mutation induction, carcinogenic transformation and killing of most cell types. One can separate the effect of radiation on DNA between direct and indirect damage. The direct damage refers to ionizations on the DNA, induced by the primary or secondary particles. The indirect damage is provoked by radicals, produced from the reaction of incident particles in water. In charged particle therapy, the probability of direct damage is higher than the probability of indirect damage.
The most common DNA damages induced by radiation are:

- the single strand break: it can be easily repaired thanks to the double-stranded nature of the DNA molecule. It is the principal damage in the

case of X ray radiations.

- the double strand break: the breaks in two strands are opposite one another or separated by a few base pairs. It is the most serious damage and the repair is more difficult. It is the principal damage of heavy particles.

The damage can lead to dysfunction and loss of genetic material: pieces of DNA may join to form chromosomal aberrations, which can cause subsequent cell death [1].
The overall effect depends on the radiation quality and on the deposited dose. In this context, LET [2] is the key parameter to link the physical property with biological effects of the radiation. It indicates the quality of radiation and its ionization density. Looking at Fig. 1.3, low LET radiations have tracks with primary events well separated in space (sparsely ionizing), on the contrary high LET particles have tracks very close in space (densely ionizing). The charged particles, compared to photons, are considered as high LET particles due to their dense energy deposition along the track, that produce more localized DNA damages.

The study of cell survival show that heavy charged particles have an increased relative biological effectiveness (RBE) compared to conventional radiotherapy. The RBE is the most relevant quantity for describing cell killing and is defined as the ratio of:

$$RBE = \frac{D_{ref}}{D} \tag{1.1}$$

where D_{ref} is the dose of X ray, giving the same biological effect as D, the dose delivered by another particle type. The RBE for charged particles shows that to obtain the same cell survival the dose required is lower than with photons. The RBE is a complicated radiobiological concept depending on several factors: LET, dose rate, fractionation, particle mass, biological endpoint, cell cycle phase, cell type, oxygen concentration [4]. The RBE increase with increasing LET up to a maximum value (Fig. 1.4), specific for the particle type.

Another crucial parameter is the rate of oxygenation of the irradiated cells. In fact, cells with a low oxygenation rate (hypoxic cells) are more radioresistant than those with a normal oxygenation rate. Unfortunately, hypoxic cells are located in the tumours. The effect is parameterized by the Oxygen Enhancement Ratio (OER) which is defined by:

$$OER = \frac{D_{hypoxic}}{D_{normal}} \tag{1.2}$$

[1] The term cell death has been used to indicate the loss of reproductive capacity of the cell.

[2] The Linear Energy Transfer (LET) is defined as the average energy locally imparted in the target by the particle, per unit track length (usually expressed in $KeV/\mu m$).

where $D_{hypoxic}$ is the dose needed to kill the hypoxic cells and D_{normal} is the dose in case of normal oxygenated cells. The RBE value increases with the size of the ion and the OER value decreases with the size of the ion. In fact, hadrontherapy is ideal against hypoxic tumors. The irradiation with high LET particles also reduces angiogenesis and the cell migration [6].
In hadrontherapy, charged particles have low LET in the entrance region (for proton in water is about 1 $KeV/\mu m$), but the LET increases in the SOBP (2-6 $KeV/\mu m$) [7]. The increase of LET corresponds to an increased RBE [8] and this effect is significant in the last few mm of SOBP.
The use of heavy ions with very high LET (like He, Ne, O, C and Ar) was justified by the hypoxia. However, the LET for heavy ions in the entrance region is quite high and produces an increased NTCP (Normal Tissue Complication Probability). The Carbon ion, with a LET in the entrance around 11-13 $KeV/\mu m$ and 40-90 $KeV/\mu m$ on the SOBP, seems to be a good heavy ion candidate for hadrontherapy.
The increased biological effectiveness of heavy charge particles is a great advantages compared to X ray, but the main problem is the high uncertainty in the RBE value. For protontherapy, the RBE assumes the constant value of 1.1: it is a practical but incorrect approximation. This choice is an open topic much debated and simulations and models are currently being published [9] [10] [11] [12] [13]. In proton therapy, there is a great effort to increase the

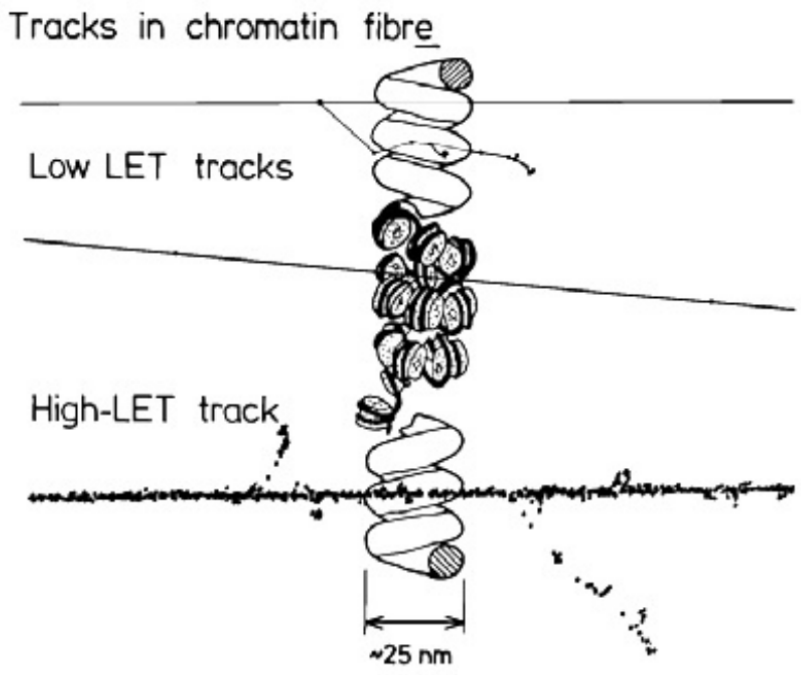

Figure 1.3: Interaction of high and low LET radiations thought a section of chromatin fiber.

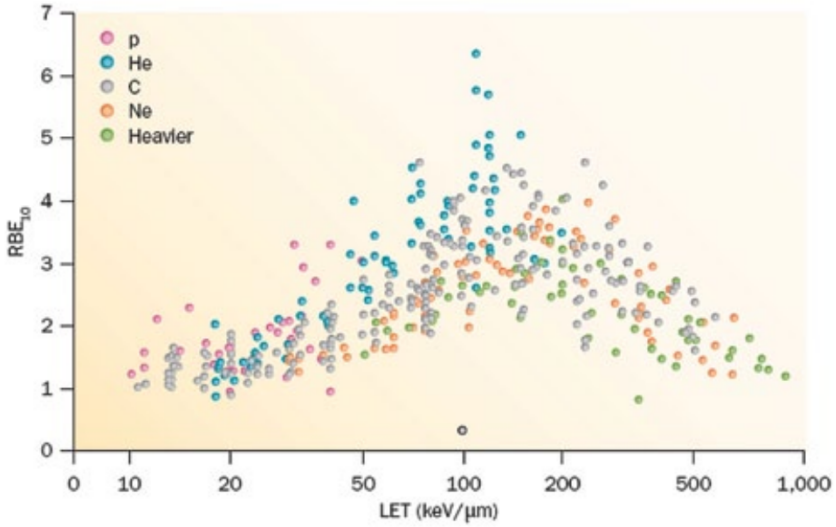

Figure 1.4: RBE versus linear energy transfer (LET). The different colors indicate different ions, from protons to heavy ions [5].

accuracy of the RBE calculation, with the final objective of implementing biological models in the available TPS.
In Carbon ion therapy, the plans are optimized using two different models: the LEM (Local Effect Model, developed at GSI), which predicts the RBE starting from the corresponding clinical photon data and a model developed at NIRS, based on in vitro cell killing experiments [14] [15]. Recently, NIRS has introduced a modified microdosimetric model (MKM) [16].
In addition, more and more research is dedicated to the study of the effect of RBE for normal tissue. For example, overdosages to the tumors are acceptable, but they can lead to toxicity in the normal tissue. To this aim, more experiments are needed for a safe dose evaluation in the target volume.

All these effects will provide biological improvement to the physical advantages of using heavy particle in the cancer treatments.

1.2 Particles for therapy

In particle therapy, the most commonly used particles are protons and carbon ions. They present some differences both in physical and biological interactions.
The lateral scattering and the energy straggling are more pronounced for protons than for carbon ions. However, carbon ions shows a fragmentation tail beyond the Bragg peak, due to their fragmentation.
Protons have a similar biological effectiveness compared to photons, except in the distal part of the SOPB. Carbon ions have a non constant depth profile

of RBE: in the entrance region they have low RBE value, while at the end of their range the RBE increases with values between 2 and 5. This is the main advantage of carbon ions compared with protons.
In conclusion, protons are more suitable for tumors near the organs at risk, for example uveal melanoma, while carbon ions are used for radioresistant tumors, due to their higher RBE and OER.
Nowadays, the effectiveness of other ions [17] [18], such as ^4He and ^{16}O, is under also investigation.

1.2.1 The rediscovery of Helium beams

Recently, Helium beams have been rediscovered as a good compromise between protons and ^{12}C ions [17].
Helium ions have been introduced between 1975 and 1992 at LBNL (Lawrence Berkeley National Laboratory, USA) for the treatment of patients with carcinoma [19]. From 1975, a systematic study of ^4He advantages in the dose localization was implemented [20]. The patients treated with ^4He have indicated promising results in treatment of uveal melanoma [21] and skull base tumor [22] [23]. Helium beam can be also used for the treatments of pediatric patients [24]: the children are usually treated with protons rather than photons to reduce the integral of dose and reduce the risk of inducing secondary tumors.

From a physical and biological point of view, ^4He ions seem to fill the gap between protons and ^{12}C [25]. The most important advantages of ^4He beams are a reduction of:

- multiple Coulomb scattering compared to protons [24],
- energy straggling compared to protons [26],
- projectile fragmentation than Carbon ions,
- the relative biological effectiveness (RBE) in the Bragg peak region compared to ^{12}C [27].

Comparison with Proton beam

The comparison between proton and ^4He ions [28] shows some significant advantages in the longitudinal and lateral dose distribution.
The Helium ions, having four times the mass of protons, are less affected by multiple Coulomb scattering (Fig.1.5). Helium features a smaller lateral beam profile compared to protons, this leads to a more concentrated lateral beam reducing the dose deposition in the plane perpendicular to the beam direction. The range of particles is proportional to the ratio of the mass number A and the square of the atomic number Z ($R \sim A/Z^2$), so we can expect a similar range for helium ($A = 4$, $Z = 2$) and proton ($A = Z = 1$). The results of

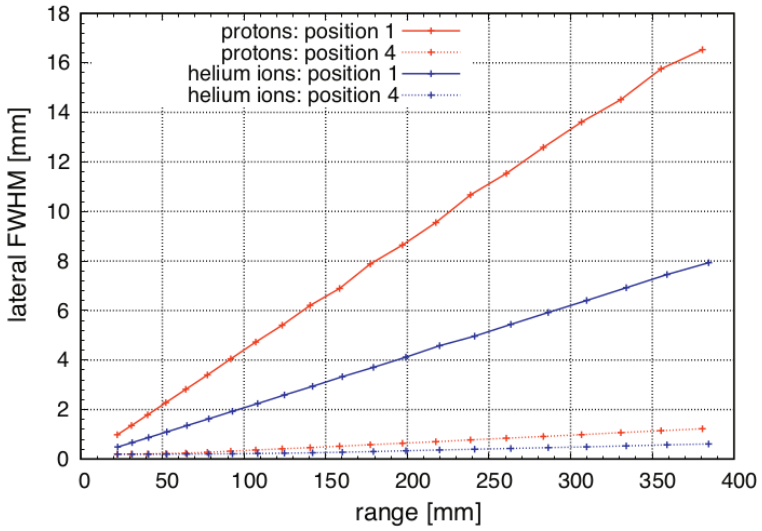

Figure 1.5: Figure from [28]: the FWHM of the lateral profile as a function of depth for protons and helium ions.

the comparison between NIST data and simulation show a deviation less than 1.3%.
The effect of energy straggling is less evident for ^4He ions due to the four times higher mass compared with protons: the width of Bragg peak is about 50% of proton beams [18], as shown in Fig.1.6.
The longitudinal profile of Helium beam shows a fragmentation tail, while for protons there is no considerable energy deposition behind the Bragg peak. In fact, the nuclear interactions of Helium ions produce the fragmentation of the projectile reducing the number primary particles, while the number of secondaries is increased. The charged fragments, having lower mass, deposit their energy behind the Bragg peak. The study of fragmentation is important not only for the precise dose evaluation in treatment planning, but also for the biological effects that is different for the secondary particles.
Less beam broadening and reduced energy straggling enable a more precise and accurate treatments, increasing the conformity of the dose distribution and sparing the surrounding healthy tissue.

Helium ions has linear energy transfer (LET) range similar to protons [29], but offer an improved RBE and oxygen enhancement ratio, allowing for less demanding biological modeling compared to ^{12}C ions. Radiobiological experiments for ^4He ions show a higher RBE (1.6) and the OER at 10% survival was found to decrease from 2.9 to 2.6 in the peak region, when compared to protons [30]. Therefore, Helium ions show advantageous features for radioresistant hypoxic tumors. Particle therapy with ^4He could offer an improved dose distribution compared to protons, keeping the evaluation of biological effects

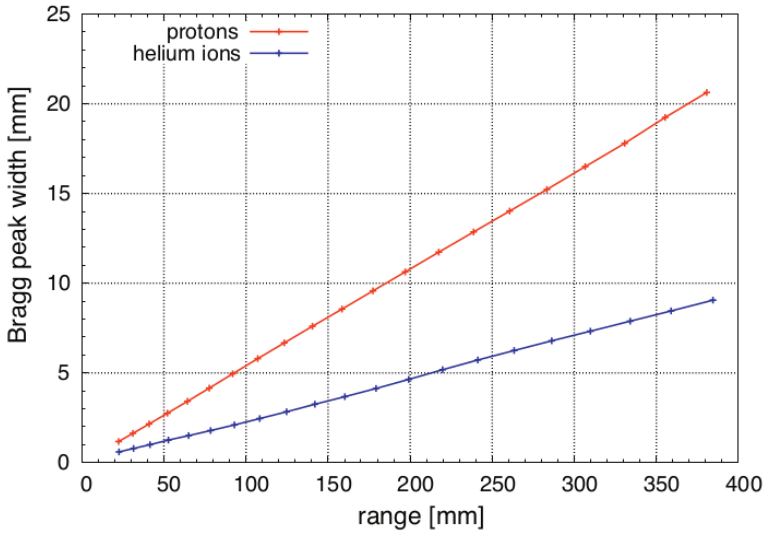

Figure 1.6: Figure from [28]: the Bragg peak width as a function of depth for protons and helium ions.

at a safe level concerning the uncertainties in treatment delivery.

Therefore, from the physical and biological point of view, ^4He seem to be a promising candidate for particle therapy.
The facilities HIT (Heidelberg Ion beam Therapy center, Germany), MIT (Marburg Ion beam Therapy center, Germany), CNAO (Centro Nazionale Adroterapia Oncologica, Italy) and MedAustron (Wiener Neustadt, Austria) can also provide ^4He ions and allow the application of Helium in cancer therapy. However, for a future applications of ^4He ions in particle therapy, the physical and radiobiological characteristics of the interaction with biological matter need to be further investigated.

1.3 Dose calculation

Charge particle therapy requires continuous efforts to develop and improve tools for treatment planning.
In this Section, I illustrate the principal dose calculation tools used for the evaluation and the validation of treatments. Monte Carlo simulations are the gold standard for accurate computations of dose distribution for charged particle therapy. Due to the high computation time for the simulations their application in clinical practice is limited so that a number of analytical models have been developed to try to overcome this problem.

1.3.1 Treatment planning systems

Before the treatment, oncologists contour the tumor (PTV, CTV and surrounding OAR) from the CT images of the patients. Medical physicists create the treatment plan. The treatment plan is achieved with the Treatment Planning System (TPS): it is a sophisticated software, whose main task is to calculate optimal treatment solutions. Typically a TPS acquires patient anatomical data, converts the data from CT in water-equivalent material, simulates and optimizes the absorbed and effective dose distribution in the region of interest and defines the best beam parameters for the tumor irradiation.
The TPS software searches for the optimal treatment solution in an iterative way. Starting from an initial hypothesis on the beamlets intensities, the program computes the deposited dose and estimates the corresponding biological effect. If the result satisfies the prescription, then the TPS can terminate the execution and return to the physicist the information on the used beams.
In the TPS, the algorithms for calculation and optimization of the dose requires most of the time. In order to improve the computation speed, the TPS softwares are based on external databases which describe the interactions of ions in water, for different beam energies.

1.3.2 Monte Carlo simulations

The most accurate solution is to evaluate the dose distribution with Monte Carlo (MC) simulations, which are becoming more and more available for the treatment planning.
MC simulations follow the interaction on a particle by particle, using models or experimental cross section for all interactions: electromagnetic and nuclear, also including the radioactive decay of the produced fragments. Moreover the Monte Carlo code consider inhomogeneities using the material properties as element composition, density and ionization potential. The simulation tracks also the secondary particles, which allow a good description of nuclear fragments.
Monte Carlo codes, like FLUKA [31], Geant4 [32], MCNP [33] or PHITS [34], are used to benchmark treatment planning system (TPS) in hadrontherapy and are considered as the powerful quality assurance tool. Geant4 has been used at the Massachusetts General Hospital in Boston for TPS comparison in proton therapy [35] [36]. The FLUKA code is now used in CNAO and HIT center [37] [38] for the validation of treatment with proton and Carbon ions.
Due to the statistical nature of MC codes, a large number of primary particles need to be simulated to obtain accurate results, but the necessary computation time has been prohibitively slow for the clinical application. Fast Monte Carlo codes dedicated to proton therapy have been developed: the codes presented by Li [39], Tourosky [40] and VMCpro [41].
It is likely that the future of dose evaluation lies in Monte Carlo. In recent years, the graphics processing units (GPUs) have been employed to overcome

the high computational time [42] [43] [44] [45] [46]. Nowadays, the efficiency of MC simulation is not yet optimized for clinical practice.
There are hybrid tools that combine aspects of Monte Carlo simulations and analytical models. There are many way to improve algorithms by adding MC components, with a significant decrease of calculation time. A example of MC-based treatment planning (MCTP) tool for proton therapy was proposed by Mairani et al. in [47], where the dose predictions are obtained with the FLUKA code. An extension of the MCTP tool for carbon ions was shown in [48].

1.3.3 Analytical models

Currently, TPS softwares for proton therapy are based on fast analytical dose algorithms. The reasons to use analytical algorithms and to continue to improve them are:

- the analytical calculations are still faster then MC simulations. This is a crucial parameters during the treatment planning to obtain a overview of the dose distribution.
- the analytical calculations is enough accurate in regions without critical heterogeneities.

A solution for the dose distribution obtained by both passive and active beams is the implementation of pencil beam models, where the total dose is given by a superposition of many pencil beams. In the treatment planning, the pencil beam algorithms [49] are accepted and diffused for the description of the beam characteristics of heavy particles.
The assumption of pencil beam models is the approach proposed by Hogstrom in [50] [49]. The dose $D(r, z, E)$, where r describes the lateral distance, z is the depth and E is the initial energy of a beam of N particles can be divided into a central axis term $d(E, z)$ and an off axis term $L(r, z, E)$ [51]:

$$D(r, z, E) = N \times d(E, z) \times L(r, z, E) \tag{1.3}$$

The longitudinal contribution $N \times d(E, z)$ is the integrated dose in a depth z, evaluated using Monte Carlo simulation [37] or analytically [52] [53]. In general, the pencil beam algorithm uses calculated look-up tables of the depth dose distribution in water, like the model presented in [54]. An alternative use of Monte Carlo is the implementation of MC-generated dose distribution to be used as look-up tables in the pencil beam algorithms.
Using the water equivalent range algorithm, the dose values are converted to other biological material considering the anatomical heterogeneities of the patients.
In proton therapy, the uncertainty due to the multiple Coulomb scattering on the traversing distribution is the most important effect that limit the accuracy

of analytical calculation of the dose distribution [54].
For the lateral contribution $L(r, z, E)$, several approaches have been proposed. The single Gaussian is however the typical choice in clinical practice. In many pencil beam algorithms [55] [56] [57], the lateral profile is modelled with a Gaussian distribution.
The pencil beam algorithm with Gaussian lateral model was originally developed for dose evaluation in electron therapy [50] [58] [59] and now is used in proton therapy [49] [54] [57] [60] [61] [62] [63]. However a real lateral profile carry a low dose envelope which can extend up to several centimeters from central axis: the halo. The halo consist of large angle scattering or secondary particles produced by nuclear interactions [64]: this lead to extend tails in the spatial distribution of the beam. In the current TPS, the halo is neglected by single Gaussian model with an error on the order of 5%.
To improve the accuracy of the treatment plan, a description of low dose contributions is usually added. At the same time, it is important to limit the calculation time and the complexity in a reasonable window.
The simpler idea proposed by Pedroni [65] is obtained by adding a supplementary Gaussian function, to account for a low dose envelope, to the single one. The double Gaussian model is used in many beam models, for example [65] [51] [66] [67] and the improvement in accuracy and calculation time is good.
We have investigated different models for the parametrization of the lateral dose distribution [67], focusing on the high accuracy of dose calculation and the fast computing time for proton therapy. The alternative proposed function are the triple Gaussian, the Gauss-Levy, double Gaussian and a Cauchy Lorentz function. In addition to these functions, we proposed new parametrization, called Gauss Rutherford, which consists of a Gaussian core to describe the multiple scattering effect and a Rutherford-like hyperbole to represent single scattering. The Gauss Rutherford function has been applied for the description of the lateral profile of ^4He ions with an excellent agreement, as presented in [68] [69].

In conclusion, the dose calculation algorithms have been widely used in clinical applications for treatment planning, due to their acceptable accuracy in most clinical settings.

1.3.4 Models for ^4He ions

In addition to approximated analytical functions, in order to estimate the energy deposition of ^4He ion beams, the implementation of physical models is ongoing, in an effort to improve the accuracy without using MC codes.

H. Fuchs et al. developed a pencil beam algorithm in [70].
The dose deposition is determined using a look-up table (LUT), derived from MC simulation. The analyzed energies are between 50 and 250 MeV/A are pre-calculated with GATE 6.1 in water, with and increments of 10 MeV/A.

The energies between these LUT values are interpolated using cubic-spline function. The extension to other materials different than water is based on the algorithm of water-equivalent depth scaling.
In the lateral beam profile, the multiple Coulomb scattering is implemented with the Fermi-Eyges theory, developed by Gottschalk in [55][71]. The nuclear interactions are added using a new Voigt function, which is a convolution of a Gaussian and a Lorentzian function, and implemented in an off-line fitting procedure by a LUT approach.
The dose deposited in a voxel of 500 μm^3 was compared with the MC simulations in case of homogeneous and heterogeneous phantoms, showing an excellent agreement. The pencil beam algorithm has a flexible design which makes a promising candidate for integration in a TPS.

An alternative model is TRiP98, developed for in-house clinical use at GSI in the 90s[52] [72] [73] [74] [75]. It was implemented as a prototype for the commercial Siemens SynGo PT planning system and now it is used for research purposes. TRiP98 has table-driven design that allows to import new data sets as depth dose distribution or RBE tables.
The energy loss distribution is described by a model that includes the energy straggling and the nuclear interaction in order to reproduce the experimental data with accuracy. The lateral profile is assumed as Gaussian form and symmetric in x and y planes. The prediction of the TRiP98 was approved by the experimental data for Carbon ions.
TRiP98 is well suited to serve as research prototypes, in particular for 4D treatment planning [76], as well as for so called adaptive treatment planning, aimed at the improvement of dose optimization in case of spatio-temporal variation of organ geometry. The latest version of TRiP98 [75] features a new model for ^4He ions and the comparison with measurement show a good agreement [18] [25] [68].

The necessary step for the application of ^4He ions in cancer therapy is the development of new algorithms for TPS or extensions of existing versions. The measurements available in literature present a gap in the therapeutic energy range [18] and a new database of experimental data [25] [77] is ongoing for the treatment planning verification and development.

1.4 The MONET code

MONET (MOdel of ioN dosE for Therapy) is a code develop in this thesis for the computation of the 3D dose distribution for proton and ^4He beams in water [78]. The advantages of MONET are the lateral and longitudinal term calculation based on first principles, the fast calculation time and the accuracy.
For the lateral profile, MONET is based on the Molière theory of multiple

Coulomb scattering, taking into account the energy loss and the effects of compounds. In order to include also the nuclear interactions, we add the Cauchy-Lorentz function, where the two parameters are obtained by a fit to a FLUKA simulation [79]. We have implemented the Papoulis algorithm [80] for the passage from the projected to a 2D lateral distribution.
For the longitudinal profile, we have implemented a new calculation of the average energy loss that is in good agreement with simulations and other formulas [53] [81]. The inclusion of the straggling is based on the convolution of energy loss with a Gaussian function [53] [57]. In order to complete the longitudinal profile, also the nuclear contributions are included in the model using a linear parametrization with only two parameters.
The total dose profile is calculated in a 3D mesh by evaluating at each depth the 2D lateral distribution and by scaling it at the value of the energy deposition.
Concerning the electromagnetic part, the model is completely analytical and is based on well known and validated theories. The nuclear interactions are parameterized using functions with few parameters, adjusted on the Monte Carlo calculations.

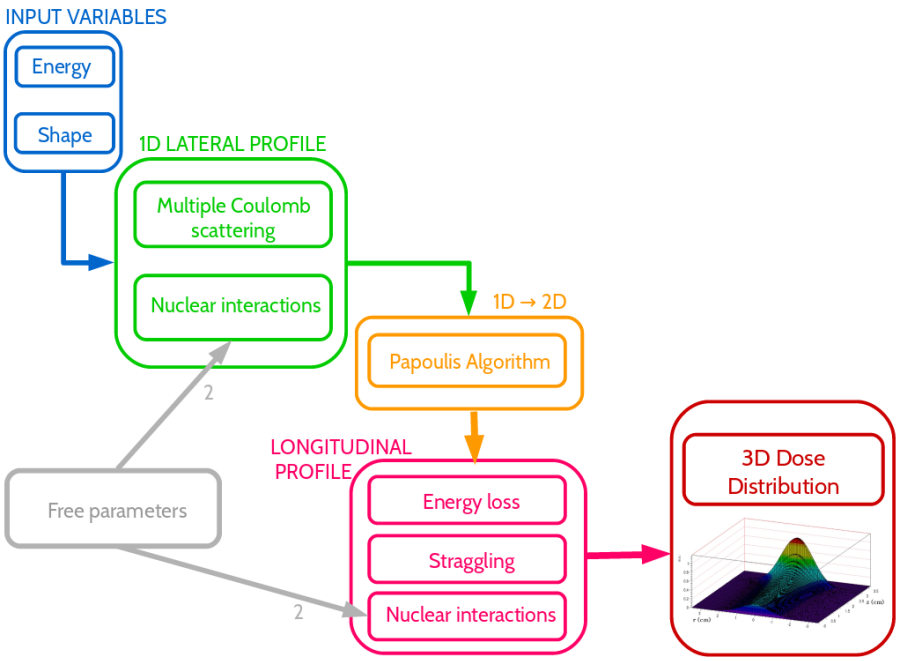

Figure 1.7: The workflow of the MONET code.

The workflow of the code is reported in figure 1.7, where the input variables are the energy and the beam shape.
The first step of the MONET code is the evaluation of lateral distribution taking into account the Multiple Coulomb scattering and the nuclear interaction.

Afterwards, starting from the 1D lateral profile the model reconstruct the 2D radial distribution.
The last step is the calculation of energy deposition and the scaling of the 2D lateral distribution at this value. In this way, the code is able to evaluate a 3D dose distribution.
In Chapter 2, the implementation of lateral profile will be shown, based on Molière theory for the multiple Coulomb scattering and a Cauchy Lorentz function for the nuclear interactions.
In Chapter 3, the implementation of longitudinal profile, considering the average energy loss, straggling and nuclear interaction, will be presented.
All results are compared with the FLUKA MC code, which is currently used in many hadrontherapy centers and has been recently validated with experimental data.

Chapter 2

The Lateral Profile

The accurate evaluation of the lateral dose profile is an important issue in the field of hadrontherapy. The lateral profile requires a correct calculation particularly for fields with many pencil beams and more accurate beam profile models are needed.
The beam spread is generated by the combination of two processes: the Multiple Coulomb Scattering (MCS) and the nuclear interactions (Fig.2.1). Modern Treatment Planning Systems (TPSs) generally approximate the dose profiles by a sum of Gaussian functions [67].
The traditional approach in hadrontherapy is to use the so called Fermi-Eyges theory: the rationale behind this dates back to the first applications with electron beams and is still applied with hadrons [82]. This theory is essentially a Gaussian approximation of the core and is not able to reproduce the tails of the distribution. It is customary to add these effects as further parametrizations called nuclear halo, aura and spray to describe both the electromagnetic and nuclear scattering [83] [84].
The MONET code instead, as explained in [79], is based on the description of the multiple Coulomb scattering by the Molière theory and a Cauchy-Lorentz parametrization for the nuclear tails. This model is able to treat multiple scattering in a very detailed way, with better accuracy than the integration of the Fermi-Eyges distribution. In MONET, the calculation of the total electromagnetic effects without any free parameter allows that the nuclear part can be easily parameterized. This strategy produces a more stable solution and in case of protons is in excellent agreement with Monte Carlo codes [79].
The MONET approach still holds in the case of ^4He beams. Being based on theory of the multiple Coulomb scattering for a charged particle, only small changes are required for the electromagnetic contribution and a new fit of the tails, where the nuclear interactions play a more important role respect to protons, is required to determine the model parameters.
Examples of a the lateral profile for proton and ^4He beam are shown in Fig. 2.1: looking of these distributions, it is simple to note that the effect of the lateral beam spread can be evaluated with a good accuracy in order to limit

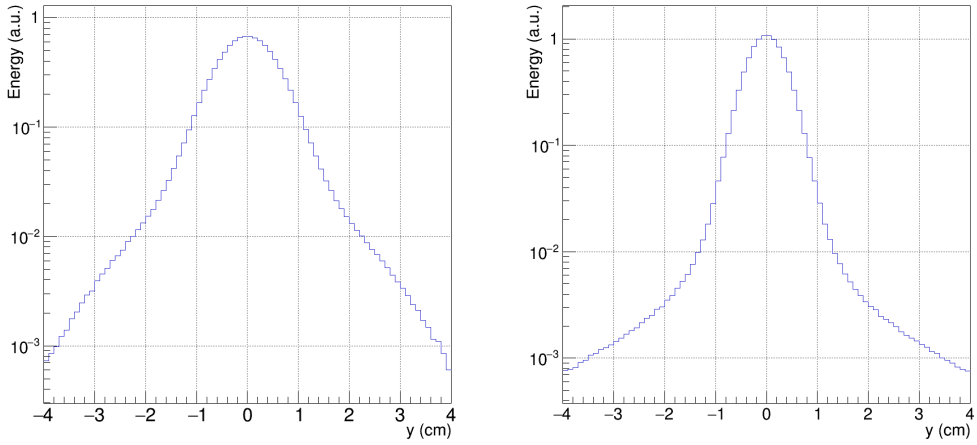

Figure 2.1: Lateral profile of proton (left) and ^4He beam (right) of 150 MeV/u at 15 cm water depth.

the dose in the tumor, saving healthy tissues.

2.1 Multiple Coulomb scattering

The scattering proceeds via the electromagnetic (em) interaction between the charge of the projectile and the charge of atomic electrons or nucleus of the target. The scattering process occurs frequently due to the long range of the Coulomb force and a little quantity of energy is transferred in these collisions, since the mass of the nuclei of the target are usually large compared to the incident particle. The deflection of a charged particle in a single interaction is extremely small. The particle traverses the material following a random zig-zag path. The total angular spread of a beam after a thickness of medium is due to the random combination of many deflections (Fig. 2.2). This phenomenon is called multiple Coulomb scattering and is responsible for the isotropic angular deflection of particle, respect to the original direction of the beam.
The scattering effect is more important for light particles (protons), however also for hadrons (^4He or ^{12}C) is not negligible.
The angular distribution is close to a Gaussian at small angles, but as angle increases, there is a long broad tail. At large angle, the deflections are generally due to one single, large angle Coulomb scattering in the medium. Therefore, the tail follows the Rutherford form for single scattering ($1/\sin\theta^4$), rather than a Gaussian shape.
The rigorous evaluation of multiple Coulomb scattering is complicated and several theories and formulae with different levels of sophistication exists [85] [86] [87] [88]. The principal theories are Molière [89], Snyder and Scott [90] [91] [92] [93], Goudsmit and Saunderson [94], and Lewis [95].

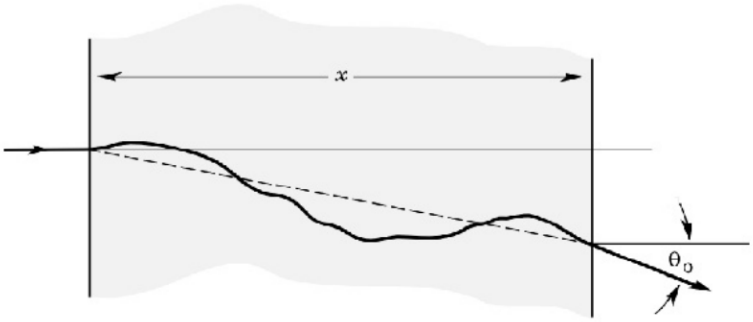

Figure 2.2: Effect of Multiple Coulomb Scattering.

The theories of Molière and of Snyder and Scott are based on the approximation of small scattering angles and use the expansion in Bessel function. Goudsmit and Saunderson instead develop a theory using an expansion in Legendre polynomials valid for any angle. Lewis, starting from the Legendre polynomials, limits the theory to small angles events. These theories on Multiple Coulomb Scattering are mathematically closely related and can give exact result if carefully evaluated.

In the contest of Hadrontherapy, there are many papers on pencil beam algorithms based on the Fermi Eyges theory [49] [54] [57] [60] [61] [62] [63]. For the study of multiple Coulomb scattering, we have analyzed the difference between the Fermi Eyges theory, that is a Gaussian distribution with the Molière theory.
In the following (Sect. 2.2-2.5), I delineate the features of these theories and compare the results, derived from the two different approaches.

2.2 Fermi Eyges's theory

Fermi and then Eyges developed a theory for charged particles that produce multiple scattering in the material [96]. Fermi-Eyges theory describes the spatial and angular distribution in the assumption that the particles undergo many small angle scattering events. It was initially used in pencil beam algorithm for electron beams and more recently it is extended to proton and Carbon ions beams.

In Fermi-Eyges theory, the probability to find the particle after a thickness z in the intervals $(x, x + dx)$ and $(\theta_x, \theta_x + d\theta_x)$ is:

$$P(x, \theta_x)dxd\theta_x = \frac{1}{2\pi\sqrt{B}} \exp\left(-\frac{1}{2}\frac{A_0x^2 - 2A_1x\theta_x + A_2\theta_x^2}{B}\right) dxd\theta_x \qquad (2.1)$$

where

$$B = A_0 A_2 - A_1^2 \tag{2.2}$$

The parameters A_n are written as moments:

$$A_n = \int_0^z (z - z')^n \, T(z') dz' \tag{2.3}$$

The moments A_n play a central role in Fermi-Eyges theory. In analogy to stopping power, we can define the scattering power $T(z)$ as the rate of increase of the variance of the projected angle:

$$T(z) = \frac{d \left\langle \theta_x^2 \right\rangle}{dz} \qquad \left\langle \theta_x^2 \right\rangle = \int_0^z T(z') dz' = A_0 \tag{2.4}$$

In hadrontherapy, many papers are devoted to the calculation of the scattering power. In general, any formula for $T(z)$ consist of three factors: a material dependent term, an energy dependent term and a single scattering correction term. The scattering power was introduced by Rossi [97], but he did not use that term. It was named by Brahme in the contest of the electron radiotherapy and now it is also used for hadrontherapy.
Starting from the original formulation of Rossi [97], many authors have proposed improvements, the most used are Kanematsu [98] and Gottschalk [71] [82].
The relation that reproduces better the experimental data is:

$$T(z) = f_s(z, R, p(z), \beta(z)) \left(\frac{E_s}{p\beta} \right)^2 \frac{1}{X_s} \tag{2.5}$$

where p is in MeV, $E_s = 15$ MeV and X_s is the scattering length. The Eq. 2.5 differs from the Molière angular variance by a few percents [82].
The scattering length, for a material of density ρ, is given by [82]:

$$\frac{1}{\rho X_s} = 0.349 \times 10^{-3} \, \frac{Z^2}{A} \left\{ 2 \ln[33219 \, (AZ)^{-1/3} - 1] \right\} \tag{2.6}$$

In case of mixtures and compounds, the total length can be evaluated using this relation:

$$\frac{1}{\rho X_s} = \sum_i w_i \left(\frac{1}{\rho X_s} \right)_i \tag{2.7}$$

where w_i is the fraction by weight.
The function $f_s(z, R, p(z), \beta(z))$, the so-called non-locality correction, has a logarithmic dependence on the energy loss [82]:

$$\begin{aligned} f_s(z, R, p(z), \beta(z)) \;=\; & 0.5244 + 0.1975 \log_{10} \left[1 - \left(1 - \frac{z}{R} \right)^k \right] \\ & + 0.2320 \log_{10}(p(z)\beta(z)) \\ & - 0.0098 \log_{10} \left[1 - \left(1 - \frac{z}{R} \right)^k \right] \log_{10}(p(z)\beta(z)) \end{aligned} \tag{2.8}$$

where p is in MeV and the lengths in cm. The non-locality takes into account the fact that, by dividing the absorber in many layers, the sum in quadrature of the r.m.s. deviations of the single layers gives a total r.m.s deviation which is not equal to that of the whole absorber. It is due to the dependence between the layers: a layer receives particles already deflected by the previous one. This effect can be only eliminated in the Monte Carlo simulation. In the analytical approaches the non-locality can be only minimized. The logarithms in the function of equation (2.8) prevents the analytical solution of equations (2.3), that must be integrated numerically.

At energies typical of hadrontherapy, some studies on the lateral spread in water [99] [100] have shown that good results are obtained with equation (2.5) and the choice

$$E_s = 12.7 \text{ MeV} , \qquad f_s = 1 \qquad X_s = X_0 \tag{2.9}$$

where X_0 is the radiation length, as in the original Rossi formulation. In the following we will consider both equation (2.8) or (2.9).
From equation (2.1) it is possible to obtain the marginal 1D distribution for the projected angle θ_x by integration:

$$f_E(\theta_x)d\theta_x = \frac{1}{\sqrt{2\pi A_0}} \exp\left(-\frac{1}{2}\frac{\theta_x^2}{A_0}\right)\theta_x \tag{2.10}$$

and that of the lateral displacement:

$$f_E(x)\mathrm{dx} = \frac{1}{\sqrt{2\pi \mathrm{A}_2}} \exp\left(-\frac{1}{2}\frac{\mathrm{x}^2}{\mathrm{A}_2}\right)\mathrm{dx} \tag{2.11}$$

The scattering power moments A_0 and A_2 appear as the variances of the multiple scattering angle and displacement distributions, respectively. The passage from the lateral displacement distribution to the angular can be obtained with the change of variable in equation (2.11):

$$x \to \theta_x \sqrt{\frac{A_2}{A_0}} \tag{2.12}$$

Obviously, it is possible also the inverse transformation. Therefore, the effective longitudinal squared length between the detection plane and an effective scattering point is:

$$z_{\text{esp}}^2 = \frac{A_2}{A_0} \tag{2.13}$$

and allows the passage from angles to displacements in the small angle approximation [82] [98].
In Fermi Eyges's theory, the equations (2.10, 2.12) are the basis for the beam setting and dose calculation in hadrontherapy.
In the Gottschalk paper [82], there is the study of conditional distributions and gives also the covariance between displacement and angle:

$$\langle x\, \theta_x \rangle = A_1 = \int_0^z (z - z')\, T(z') dz' \tag{2.14}$$

In conclusion, Fermi Eyges's theory provides the distribution for the projected angle (Eq. 2.10) and for the lateral displacement (Eq. 2.11). However, for the dose calculation in hadrontherapy, the main information is the lateral dose distribution of equation (2.11).

In the case of a layer j of thickness d_j, the equations (2.3) of the scattering power moments can be generalized using the property of the integrals. In the case of a stack with n layers, the scattering power becomes:

$$A_\alpha = \int_0^{z_{n+1}} (z_{n+1} - z')^\alpha \, T(z') dz' = \sum_{j=1}^{n} \int_0^{z_{j+1}-z_j} [(z_{n+1} - z_j) - z']^\alpha \, T_j(z_j + z') dz' \tag{2.15}$$

where z_j is the longitudinal coordinate at the j^{th} layer entrance, z_{n+1} is the coordinate at the end of the last layer and T_j means that the scattering power is calculated with equations (2.5, 2.8) or (2.5, 2.9) with $p_j(x)$, $\beta_j(x)$, R_j calculated at the entrance of the j^{th} layer.

2.3 Molière's theory

The Molière's theory starts from the standard transport equation and uses the Bessel transforms and the small angles approximation, to obtain the angular distribution of the particles scattered after a given thickness [85].
The notation adopted in the following is similar to the one introduced by Molière and Bethe [85]. The angles considered are:

- χ is the angle related to single scattering event,
- θ is the net angle after multiple scattering events.

A graphical interpretation of χ and θ angles is reported in Fig.2.3.
Molière derives his theory by considering successive collisions and the scattering can be treated as a diffusion problem in θ plane. He assumes the Rutherford form for the scattering cross section:

$$\rho\sigma(\theta) = 2\chi_c^2 \frac{1}{(\theta^2 + \chi_\alpha^2)^2} \tag{2.16}$$

where ρ is the number of $atoms/cm^2$ and χ_c, χ_α are the crucial parameters of the theory.

The scattering angle χ_c is connected to the rms scattering angle:

$$\chi_c^2 = 0.1569 \cdot 10^{-6} \frac{x}{A} \frac{Z^2 z^2}{p^2 \beta^2} \tag{2.17}$$

where Z and A are atomic and the mass number of the target, z is the atomic number of the incident particle, p is the momentum (GeV/c), $\beta = v/c$ and

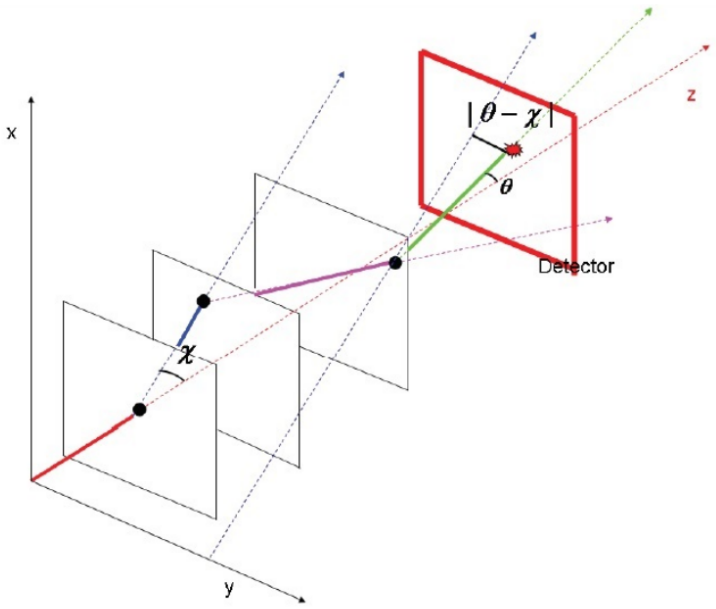

Figure 2.3: Transport of a particle deviated by multiple Coulomb scattering events. After the first scattering, the particle is deviated by a single angle χ and after successive scatterings it is totally deviated by an angle θ respect with the original z direction. The distance obtained by projecting in the transverse direction $|\theta - \chi|$ can be considered as the final lateral displacement.

x is the thickness. The Molière's formulation for χ_c is with Z^2, while Bethe proposed $Z(Z+1)$ instead of Z to take into account the scattering by atomic electrons.

The second parameter is connected to the electron screening of the Coulomb potential. The *screening angle* χ_α is defined by:

$$\chi_\alpha = \mu^2 \chi_0^2 \tag{2.18}$$

$$\mu^2 = \left(1.13 + 3.76 \left(\frac{zZ}{137\beta}\right)^2\right) \tag{2.19}$$

$$\chi_0^2 = \left(\frac{\hbar}{p} \frac{Z^{1/3}}{0.468 \cdot 10^{-8}}\right)^2 \tag{2.20}$$

Molière obtained the μ parameter parametrizing the screened Coulomb potential using the Wentzel-Kramers-Brillouin (WKB) method.
The screening angle χ_α is a cut off angle, which introduces, for very small values of χ (distant collisions), the departure from the $1/\chi^4$ law due to screening of nuclear charge by orbital electrons.

The total number of multiple scattering events is given by:

$$\rho \int_0^\infty \sigma(\theta)\theta d\theta = \int_0^\infty 2\chi_c^2 \frac{\theta}{(\theta^2+\chi_\alpha^2)^2} d\theta = \frac{\chi_c^2}{\chi_\alpha^2} \equiv \Omega_0 \tag{2.21}$$

An important term of the theory is the effective number of collisions [85]:

$$\Omega_0 - \Omega(\eta) = \frac{1}{4}(\chi_c\eta)^2 [-\ln(\chi_\alpha\eta) + C] \tag{2.22}$$

where $\eta \sim \frac{1}{\chi_c}$ and C is a constant.
The Molière distribution is given by:

$$f(\theta)\theta d\theta = \frac{\theta d\theta}{\chi_c^2} \int_0^\Gamma J_0\left(\frac{\theta\eta}{\chi_c}\right) \exp\left[-\frac{\eta^2}{4}\left(b - \log\frac{\eta^2}{4}\right)\right] \eta d\eta \tag{2.23}$$

where J_0 is the Bessel function,

$$b = \ln\frac{\chi_c^2}{\chi_\alpha^2} - 0.154432 = \ln\Omega_0 - 0.154432\ , \tag{2.24}$$

$$\Gamma = 2\exp[(b-1)/2] \tag{2.25}$$

In the small angle approximation, the connection between the two projected angles in the traverse plane is:

$$\theta = \sqrt{\theta_x^2 + \theta_y^2} \tag{2.26}$$

The angles θ_x and θ_y have the same distribution and the connection between the mean square angles is:

$$<\theta^2> = 2 <\theta_x^2> = 2 <\theta_y^2> \tag{2.27}$$

The projected angle θ_x follows the distribution [93]:

$$f(\theta_x)d\theta_x = \frac{d\theta_x}{\pi\chi_c^2} \int_0^\Gamma \cos\left(\frac{\theta_x y}{\chi_c}\right) \exp\left[-\frac{y}{4}\left(b - \log\frac{y}{4}\right)\right] dy \tag{2.28}$$

The Molière distributions in Eqs. 2.23-2.28 are the sum of a Gaussian core and for other corrective terms that describe the tails. The root mean square of the Gaussian core is given by [85]:

$$\theta_R \equiv \sqrt{\theta^2} = \chi_c\sqrt{B} \tag{2.29}$$

where B is the solution of the relation:

$$b = B - \log B \tag{2.30}$$

From Eq.2.27, the connection between the rms of the space and projected angles is:

$$\theta_{xR} = \frac{\theta_R}{\sqrt{2}} = \frac{\chi_c\sqrt{B}}{\sqrt{2}} \tag{2.31}$$

The parameter B of Eq. 2.30 can be approximated with the following formula [90]:

$$B \simeq 1.153 + 1.122 \log \Omega_0 \tag{2.32}$$

where Ω_0 is the total number of collisions of Eq. 2.21.

The distribution function can be expanded in a power series of B as:

$$f(\theta)\theta d\theta = \theta d\theta [f^0(\theta) + B^{-1} f^1(\theta) + B^{-2} f^2(\theta) + ...] \tag{2.33}$$

The distribution can be rewritten, using the characteristic multiple scattering angle:

$$f(\theta) = \frac{1}{2\pi\theta_R^2} \frac{1}{2} \left[f^0(\theta) + B^{-1} f^1(\theta) + B^{-2} f^2(\theta) + ... \right] \tag{2.34}$$

where

$$f^n(\theta) = \frac{1}{n!} \int_0^\infty J_0(\theta u) \exp\left(-\frac{u^2}{4}\right) \left[\frac{u^2}{4} - \log\left(\frac{u^2}{4}\right)\right]^n u du \tag{2.35}$$

The sum of two terms in Eq. 2.34 will be a good approximated representation of the distribution at any angle.
In particular, the principal contributions are:

- f^0 is a Gaussian with a standard deviation indicated by RMS as one can see below:

$$f^0(\theta) = 2\exp(-\theta^2) = 2\exp\left(-\frac{\theta}{\sqrt{2}\theta_R}\right)^2 \tag{2.36}$$

- f^1 has the analytical form below [101] [102]

$$f^1(\theta) = 2e^{-\theta}(\theta - 1)[E_i(x) - \log x] - 2(1 - 2e^{-\theta}) \tag{2.37}$$

  where E_i is the exponential integral function. For larger angles, the function f^1 become larger than f^0 . Indeed, for very large θ, f^1 goes into the single scattering law $f^1 = \theta^{-4}$, while f^0 decreases exponentially.

The first term of Molière's distribution represents the core of the distribution, while the extra terms account for the tails of the distribution that are non-Gaussian. In physical terms, the core of the distribution takes into account the small angles process (multiple scattering), while the tails describe the more rare scattering at large angles (single scattering).

2.3.1 Lateral displacement

We have derived a general formula, that allow the passage from angular (Molière theory) to spatial displacement.
The root mean square (rms) y_M of the transverse displacement on a detection

plane at depth z due to a layer dt at the depth t is given by $(x-t)\theta_{xR}$, where θ_{xR} is given by Eq. 2.31.
The angular squared rms is a product of χ_c^2, which is of a quantity that depends on the thickness z and that can be combined in quadrature and of the parameter B, which depends on the thickness in a logarithmic way. The reason of this is due to the dependence between two successive layers, in fact the second layer receives trajectories deflected by the first one (Fig. 2.4). Following Gottschalk [55], we combine in quadrature the χ_c^2 contributions and multiply for an average value of B:

$$y_M = \frac{\chi_W \sqrt{B}}{\sqrt{2}p\beta} \left[\int_0^z \frac{(z-t)^2}{\left(1-\frac{t}{R}\right)^k} dt \right]^{1/2} \tag{2.38}$$

where the parameter B is calculated from Eq.2.32. The Eq. 2.38 is the relation, that allows the passage from angular to spatial displacement in any depth.
One can find also the lateral displacement outside the target, by replacing the term $z-t$ in the integrand with $D-t$, where D is the detector position.

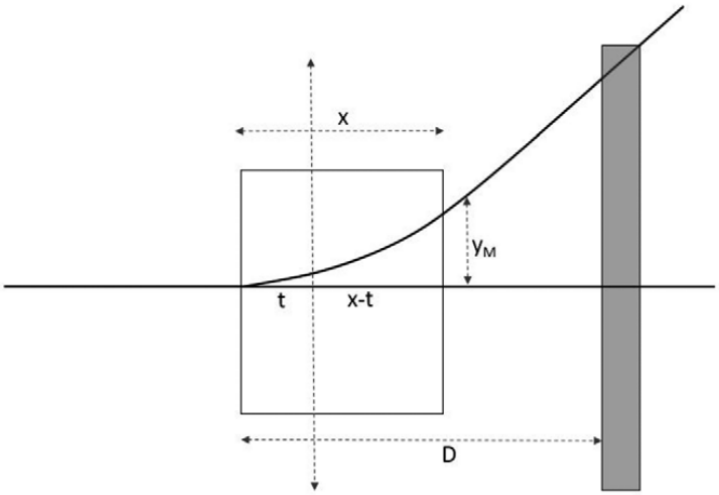

Figure 2.4: The geometry of the lateral displacement.

The rms obtained in Eq. 2.38 corresponds to the rms of the projection on the measuring plane of the rms θ_{xR} of the Gaussian core of the angular distribution. Therefore, the scale factor corresponding of the Fermi Eyges (Eq.2.13) is:

$$z_{esp} = \frac{y_M}{\theta_{xR}} = \frac{y_M \sqrt{2}}{\chi_c \sqrt{B}} \tag{2.39}$$

and permits the passage from the angular to the spatial distribution at thickness z. The change of variable is:

$$z_{esp} = \frac{y}{\theta_x} \rightarrow \theta_x = \frac{y}{z_{esp}} \tag{2.40}$$

Therefore the equation of the lateral distribution is:

$$f_M(y) = \frac{1}{\pi \chi_c z_{esp}} \int_0^\Gamma \cos\left(\frac{y\eta}{\chi_c z_{esp}}\right) \exp\left[-\frac{\eta^2}{4}\left(b - \log\frac{\eta^2}{4}\right)\right] d\eta \tag{2.41}$$

2.3.2 Energy loss

Since we will consider long paths in water, we have to modify the basic equation to take into account the energy loss process. The parameter χ_c and χ_α depends on the momentum p and β.
If we indicate as $p(z)$ and $\beta(z)$ the current values at the depth z in the target, χ_c becomes:

$$\chi_c^2 = \chi_W^2 \int_0^z \frac{1}{p(z)^2 \beta(z)^2} dz \tag{2.42}$$

To take into account the energy loss in the absorber, we use the empirical Øverås formula [103], which gives the value of $p(z)^2$ and $\beta(z)^2$ for a charged particle of incident momentum $p\beta$, after traversing a slab of thickness z [55]:

$$p(z)^2 \beta(z)^2 = p_0^2 \beta_0^2 \left(1 - \frac{z}{R}\right)^k \tag{2.43}$$

where R is the range for the particle of incident momentum p. The Eq. 2.43 is fairly accurate for many materials of density ρ and radiation length X_0 if k is calculated with [104]:

$$k = 1.0753 + 0.12 \exp(0.09 \rho X_0) \tag{2.44}$$

We verified that, with $k = 1.07$, the Eq. 2.43 is accurate for water within 2% compared with the Eq. 2.44.
Taking into account the energy loss, the equation for χ_c^2 becomes:

$$\chi_c^2 = \chi_W^2 \frac{1}{p_0^2 \beta_0^2} \int_0^z \frac{1}{\left(1 - \frac{z}{R}\right)^k} dz = \chi_W^2 \frac{R\left[\left(1 - \frac{z}{R}\right)^{1-k} - 1\right]}{(k-1) p_0^2 \beta_0^2} \tag{2.45}$$

The logarithm (see Eq.2.22) of χ_α can be written as:

$$\log \chi_\alpha^2 = \frac{1}{\chi_c^2} \frac{\chi_W^2}{p_0^2 \beta_0^2} \int_0^z \frac{\log \chi_\alpha^2}{\left(1 - \frac{z}{R}\right)^k} dz \tag{2.46}$$

2.3.3 Mixtures and compounds

The Molière's theory can treat compounds and mixtures, by setting:

$$c_i = 4\pi N_A \left(\frac{e^2}{\hbar c}\right)^2 (\hbar c)^2 \frac{Z^2 z^2}{A} \tag{2.47}$$

Therefore, the parameters χ_c is rewritten:

$$\chi_c^2 = \sum_i c_i \int_0^x \frac{dx'}{p^2 v^2} \tag{2.48}$$

and the screening angle χ_α becomes:

$$\log \chi_\alpha^2 = \frac{1}{\chi_c^2} \sum_i c_i \int_0^x \frac{dx'}{p^2 v^2} \log \chi_{\alpha i}^2(x') \tag{2.49}$$

where i runs over the number of elementary constituents in the target.
The value of $\chi_{\alpha i}$ is obtained with the replacements:

$$Z \to Z_i \frac{1}{A} \to \frac{f_i}{A} \tag{2.50}$$

where f_i is the fraction by weight of all constituent i in the mixture or compound.

We assume that biological matter is in a good approximation water. Therefore, the calculation of χ_c and χ_α is made in case of water, substituting by a summation over the constituents.
For the evaluation of χ_c, we have:

$$\chi_c^2 = \sum_i \chi_{ci}^2 = \chi_W^2 \frac{x}{p\beta} \tag{2.51}$$

where χ_W^2 is:

$$\chi_W^2 = 0.1569 \cdot 10^{-6} \frac{z^2 (2Z_H^2 + Z_O^2)}{\sum_i n_i A_i} \tag{2.52}$$

The generalization of χ_α to water is:

$$\log \chi_\alpha^2 = \frac{1}{\chi_c^2} \sum_i \chi_{ci}^2 \log \chi_\alpha^2 \tag{2.53}$$

where χ_c^2 and χ_{ci}^2 are defined in Eq. 2.51 and $\chi_{\alpha i}^2$ are evaluated with substitution $Z = Z_H, Z_O$.
Considering the energy loss, the parameter χ_α becomes [79]:

$$\log \chi_\alpha^2 = \frac{1}{\chi_c^2} \frac{0.1569 \cdot 10^{-6} z^2}{A_W} \sum_i \frac{n_i Z_i^2}{p^2 \beta^2} \int_0^z \frac{\log(\mu_i^2 \chi_{0i}^2) - \frac{D_i}{Z_i}}{\left(1 - \frac{z}{R}\right)^k} dz \tag{2.54}$$

where μ_i is a function of $\beta(z)$ and χ_{0i} is a faction of $p(z)$. They can be calculated with $Z_i = Z_H, Z_O$ and χ_c from Eq. 2.45. The Eq. 2.54 can be evaluated with the Simpson numerical integration with a good accuracy.
Since μ_i and χ_{0i} depend on p and β separately, we have to calculate them from $p(z)\beta(z)$, resulting during the numerical integration. Setting $p(z)\beta(z) \equiv \omega$ and indicate as E_z the total energy of the projectile, we obtain:

$$p(z)\beta(z) \equiv \omega = \frac{p(z)^2}{E_z} = \frac{E_z^2 - m^2}{E - z} \rightarrow$$

$$E_z^2 - \omega E_z^2 - m^2 = 0 \rightarrow E_z = \frac{1}{2}\left(\omega + \sqrt{\omega^2 + 4m^2}\right) \tag{2.55}$$

$$p(z) = \sqrt{E_z^2 - m^2} \qquad \beta = \frac{p(z)}{E_z} \tag{2.56}$$

2.3.4 Fano's correction

Fano corrected the Molière's theory in order to take into account also that the incident particle is scattered by atomic electrons, considering the screened Coulomb field of the nucleus [105].
For the parameters χ_c^2, Bethe replace Z^2 by $Z(Z+1)$, but Fano recommends using Molière's original definition of χ_c^2.
While the screening parameter becomes:

$$\log \chi_\alpha^2 = \frac{1}{\chi_c^2} \sum_i \chi_{ci}^2 \left(\log \chi_{\alpha i} - \frac{D_i}{Z_i}\right) \tag{2.57}$$

where D_i is the Fano correction:

$$D_i = \log\left(\frac{1130}{Z_i^{4/3}\left(\frac{1}{\beta^2}\right)}\right) + u_i - \frac{\beta^2}{2} \tag{2.58}$$

where for the water target $u_H = 3.6$ and $u_W = 5.0$
Considering the water material, the energy loss and the Fano's correction, we implement two functions for a calculation of χ_c and χ_α.

2.3.5 Evaluation of Range

The MONET code evaluates the CSDA (Continuous Slowing Down Approximation) range without taking in account Coulomb multiple scattering, energy straggling, delta ray production, nuclear interaction.
The model, starting from characteristic parameters of water ($Z = 10$, $A = 18$ and $\rho = 1 g/cm^3$) and the kinetic energy (in GeV), evaluates the range using the relation [106]:

$$R = \frac{1}{\rho}\frac{A_M}{Z_M}\sum_{n=1}^{4} \alpha_n E_I^{p_n} E_k^n \tag{2.59}$$

where E_I is the mean ionization potential of the medium and $Z_M = 10$ and $A_M = 18$ in water. The mean ionization potential of water used is $77eV$: this value has been obtained by the validation with experimental data. The values of the coefficients α_i and p_i for proton beams are reported in Tab.2.1.

	Proton		Helium	
order	α_i	p_i	α_i	p_i
1	6.84690 e-04	0.4002	0.013695	0.937675
2	2.26769 e-04	0.1594	0.507739	0.934832
3	-2.46100 e-07	0.2326	-0.0243788	0.912081
4	1.42750 e-10	0.3264	0.0790533	0.891479

Table 2.1: Parameters used for the range calculation of equation (2.59).

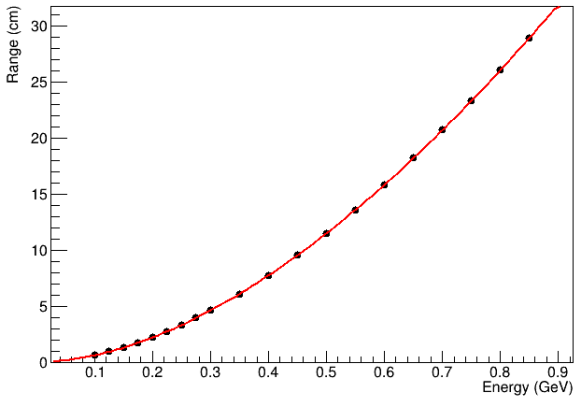

Figure 2.5: Fit of range data of ^4He in water from NIST table with expression (2.59).

In the case of **Helium beam**, we found a good agreement with the NIST table using a Ulmer-Schaffner like parametrization. The value of the coefficients are reported in Tab.2.1 and the ^4He range is plotted in Fig. 2.5.

2.3.6 Beam profile

In order to consider realist situations, we have to take into account the beam profile. For this study, we have used Gaussian beam with realist FWHM or a beam size given from the HIT phasespace file for the comparison with the experimental data.

We have assumed that the beam size is given by a Gauss-Rutherford function:

$$b(y) = \frac{a}{s} \exp\left[-\frac{y^2}{2s^2}\right] + \frac{b \cdot c}{(y^2 + c)^2} \tag{2.60}$$

where a and s are amplitude and sigma of Gaussian and b and c are amplitude and parameter of Rutherford hyperbole.
For the evaluation of beam profile, the parameters are obtained by a fit to FLUKA simulation: we simulate the particles in a geometry in which we substitute water region with vacuum, to take into account only the beam divergence. The FLUKA output is analyzed at every thickness of interest to obtain through a fit of lateral profile the parameters of Eq. 2.60.
The observed lateral profile in the presence of a measurable beam profile is given by the convolution between the distribution of Eqs. 2.41-2.60.

$$F(y) = f_m(y) \times b(y) = \int f(t) b(y - t) dt \tag{2.61}$$

All the equations are assembled in a main program that calculates the complete analytical model (without any free parameters) for the electromagnetic interaction that represents the core of the lateral distribution.

2.3.7 Molière's theory implementation

We have implemented the Molière's theory in a complete analytical model. The structure of the model consists of the following steps:

1. The kinetic energy (expressed in GeV) and the water thickness z are the input variables and are assigned. The momentum p and β are evaluated with standard formulae.

2. The parameter χ_c is calculated for water molecule, considering the correction for the energy loss.

3. The parameter χ_α is evaluated in case of water target, using the correction for the energy loss .

4. The parameter b and B are calculated from Eqs. 2.30-2.32.

5. The displacement z_{esp} is calculated.

6. The beam profile is evaluated by the convolution of the lateral displacement and a Gauss-Rutherford.

7. The total distribution $f(y)$ is calculated and describes the electromagnetic core of the total lateral beam profile.

2.4 From 1D to 2D lateral distribution

In the MONET code, we have considered the 1D lateral projections employed usually in dose calculations, because this approach simplifies both the mathematics of the algorithms, the fit of nuclear contribution and the convolution of the lateral distribution with any initial beam profile. At the end of the calculations, the connection between the joint distribution $f(x, y)$ and the projections $f_x(x)$ and $f_y(y)$ along two arbitrary orthogonal axes is important.
For two independent random variables the joint distribution is simply given by the factorization theorem:

$$f(x, y) = f_x(x) f_y(y) \tag{2.62}$$

In probability theory, a well known result is that if two random variables are independent, then they must be uncorrelated, i.e. they must have null covariance. The opposite is generally true only for Gaussian distributions. In general the property factorization(2.62) is valid only for some choice of the orthogonal axes. When it is valid for an arbitrary choice of axes in the presence of circular symmetry, a not very well known theorem states that the variables X and Y are necessarily Gaussian [80]. Therefore, for any non Gaussian joint density $f(x, y)$, X and Y are necessarily dependent.
This fact has important consequences for the analytical treatment of multiple scattering theories and the inclusion of nuclear interaction with a Cauchy-Lorentz function (Eq.2.72): since the lateral distribution is not Gaussian, the factorization property of equation (2.62) does not hold. In effect, it can be shown in [107] that the projected angles θ_x and θ_y in multiple Coulomb scattering theories are uncorrelated, but not independent.
To overcome this problem, the most common solution is to keep using Gaussian profiles, adding two or more Gaussian to approximate the lateral distribution, as shown in [67] for different parametrizations, and this is indeed the preferred choice also for many Treatment Planning Systems algorithms to reconstruct the joint transverse distribution from the projected ones [72]. In fact, only for Gaussian variables the sets of dependent and correlated variables and of independent and uncorrelated variables coincide.
Since in the MONET code, we use projected distribution from the lateral profile, we have to find a connection with the joint distribution different from (2.62). This is possible taking advantage of the circular symmetry of the problem and of a theorem of Papoulis.

2.4.1 Papoulis's reconstruction algorithm

The Papoulis method [80] can be applied in case of distributions with circular symmetry [108]. Let us consider a normalized distribution $f(x, y)$ in the $x - y$ plane with circular symmetry, i.e. such that in polar coordinates one can write:

$$f(x, y) = \hat{f}(r) \ , \quad r = \sqrt{x^2 + y^2} \tag{2.63}$$

The marginal distribution $f_x(x)$ corresponding to $f(x, y)$ is:

$$f_x(x) = \int_{-\infty}^{\infty} f(x, y)dy = \int_{-\infty}^{\infty} \hat{f}(r)dy = 2\int_{0}^{\infty} \hat{f}(\sqrt{x^2 + y^2})dy \tag{2.64}$$

The equation Eq. 2.64 is the definition of the projection operator that transforms $\hat{f}(r)$ into $f_x(x)$ by preserving the normalization.
The important fact is that the relation can be inverted to obtain the joint distribution $\hat{f}(r)$ from the marginal $f_x(x)$, under the essential hypothesis of circular symmetry. The procedure is described in Papoulis [80] and Amsel [108]. Hereafter, we recall the main steps.
One starts with the definition of the function:

$$h(r) = \int_{-\infty}^{\infty} f_x(\sqrt{t^2 + r^2})dt = \int_{-\infty}^{\infty} \hat{f}(\sqrt{t^2 + r^2 + y^2})dydt \tag{2.65}$$

where the last term comes from equation (2.64). Transforming in polar coordinates ($t = \rho\cos\theta$, $y = \rho\sin\theta$), we have:

$$h(r) = 2\pi \int_{0}^{\infty} \hat{f}(\sqrt{r^2 + \rho^2})\rho d\rho \tag{2.66}$$

With the substitution $v^2 = r^2 + \rho^2$ one obtains:

$$h(r) = 2\pi \int_{r}^{\infty} \hat{f}(v)vdv \tag{2.67}$$

Finally, using the Leibniz rule of differentiation under the integral sign, the final formula can be written:

$$\hat{f}(r) = -\frac{1}{2\pi r}\frac{dh(r)}{dr} \tag{2.68}$$

In the MONET implementation, the derivative is calculated numerically with the cubic spline and the point at $r = 0$ is obtained as the limit from the neighboring points at the right.
The equations (2.65, 2.68) define the recipe to go from non Gaussian projections f_x and f_y to the 2D distribution $\hat{f}$ with cylindrical symmetry.
In our case, the projected distributions will be used to fully represent the lateral distribution, including the multiple scattering and the nuclear interactions and the equations 2.65 2.68 will be used for the reconstruction of the radial distribution, starting from f_x.

2.5 Comparison between Fermi-Eyges and Molière theory

We compared the distributions of the two theories [109] using as a benchmark the Monte Carlo results from the FLUKA code [110] which is often used as a

reference in hadrontherapy [111] and gives results in very good agreement with data [79].
The FLUKA code treats multiple Coulomb scattering with a very detailed implementation of the Molière theory [112] the user provides the characteristics of projectile and material and the code guarantees that the result is always within the limits of validity of the theory. In the following analysis all the nuclear interactions have been switched off in FLUKA, since we are analyzing only the EM part of the interaction. For the simulations, we used the default settings for multiple scattering and the generally recommended settings for hadrontherapy (HADROTHE). The score quantity is the energy deposition in water, using a mesh of 1 mm size. The statistics used in the simulation involved 10^7 primaries, in 10 batches of 10^6 histories each. The version of the FLUKA code used is 2011.2c.5.

The Fermi-Eyges distributions were obtained with Eq. 2.5-2.8, because the results differ by about 5% from those of Eq. 2.5-2.9 but are closer to the FLUKA curve.

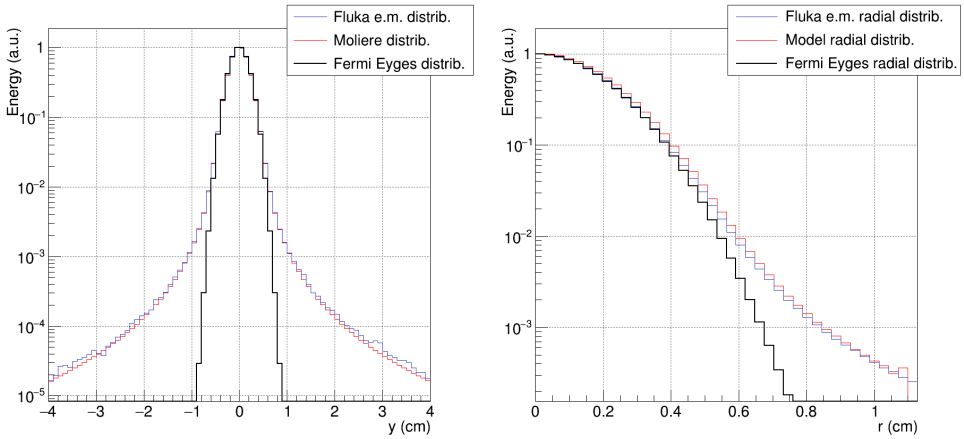

Figure 2.6: 150 MeV proton pencil beam (range 15.8 cm): projected distribution (left) and radial one (right) at 11 cm water depth.

In Fig. 2.6 we have reported the em lateral and radial displacement distributions for 150 MeV protons in water, showing the very good agreement between FLUKA and the Molière distributions. The Fermi-Eyges Gaussian does not fit well the tail of the distributions. In this case there is coincidence between the radial distribution obtained with the original Molière equation (equation (A.8) of Bellinzona paper [79] rescaled with z_{esp}) and the distribution (2.41) transformed with equations (2.65, 2.68). These equations become the only way to pass from the lateral 1D to the radial distribution, when the Molière lateral distribution is convolved with the beam profile. This is shown in Figure 2.7, where the lateral projections are the result of the convolution

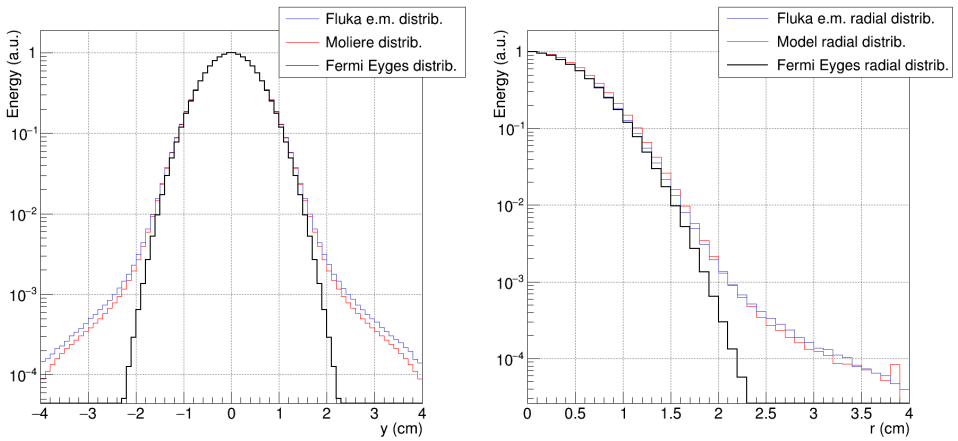

Figure 2.7: 150 MeV proton Gaussian beam (σ = 0.4 cm, range 15.8 cm): projected distribution (left) and radial one (right) at 15 cm water depth.

with a Gaussian beam profile (σ = 0.4 cm) and the radial distributions are obtained with equation (2.62) (Fermi-Eyges) and (2.65, 2.68) (Molière).
In Fig. 2.6-2.7 the Fermi-Eyges distributions have been scaled to same maximum of the Molière ones for the comparison.
Concerning the e.m. interaction, we see in figures 2.6 and 2.7, that the agreement between FLUKA and the Molière distributions is good over more than 10^{-4}, a remarkable result.
This is not obvious in principle, even if FLUKA is based on the Molière theory, because we calculated analytically the profile at a given depth taking into account the energy loss, whereas FLUKA proceeds in small steps.

A comparison between Molière distribution, FLUKA and MCNP6 is shown in [79]. FLUKA uses a transport algorithm based on Molière's theory, taking into account the correlations between scattering angle and path length corrections [112] [113] [110].The comparison with MCNP is important because it is based on Goudsmit-Sanderson's theory [94] [114].
In Figure 2.8, the comparison has shown that the prediction of MONET code is in good agreement with both simulations. Therefore, we can say that, concerning the electromagnetic interactions, MONET has the same predictive power as the MC codes.

The extension of Molière's theory in case of different material and the comparison with Fermi Eyges [109] are shown in Appendix A. Also in case of heterogeneous stack, the Molière distribution is more accurate than the Fermi Eyges Gaussian.

In conclusion, we have shown that the Molière theory has the same capa-

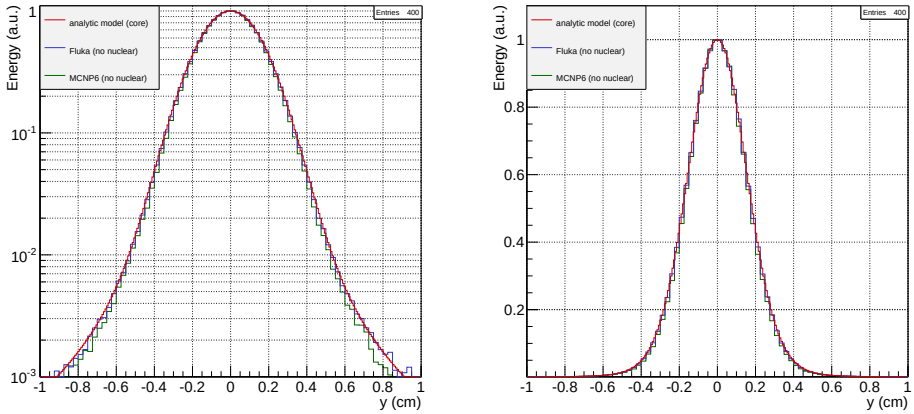

Figure 2.8: Comparison between the model (red line), FLUKA (blue histogram) and MCNP6 (green histogram, slightly below the line on the log scale) in water for 150 MeV protons at a depth of 10 cm in log (left) and linear (right) scale.

bility as the Fermi-Eyges, but a higher accuracy.
There are many advantages in the use of the Molière theory instead of the Fermi-Eyges:

- the results are in very good agreement with the Monte Carlo predictions of FLUKA,
- there are no free parameters,
- the theory is valid for any projectile and material,
- the nuclear halo, that affects the tails of the distribution of the lateral displacement, only represents the effect of the nuclear interaction. This allows for a simpler parametrization of the nuclear interaction and makes clearer its physical significance.

For these reasons, the MONET code is based on the Molière theory of multiple Coulomb scattering.

2.6 Nuclear interactions

Sometimes, the particle beam can have a collision with a nucleus, producing secondary particles in motion. These secondaries tend to have lower energies and much larger angles than primary particles. Obviously, the electromagnetic interactions dominate for light ion beam, but the nuclear interactions are not negligible. For scattering, mathematical and well validated theories exist, but the nuclear interactions are harder to model than scattering or stopping. The

lateral beam profile is significantly influenced by this process, that produces long tails of the distribution (Fig.2.9).

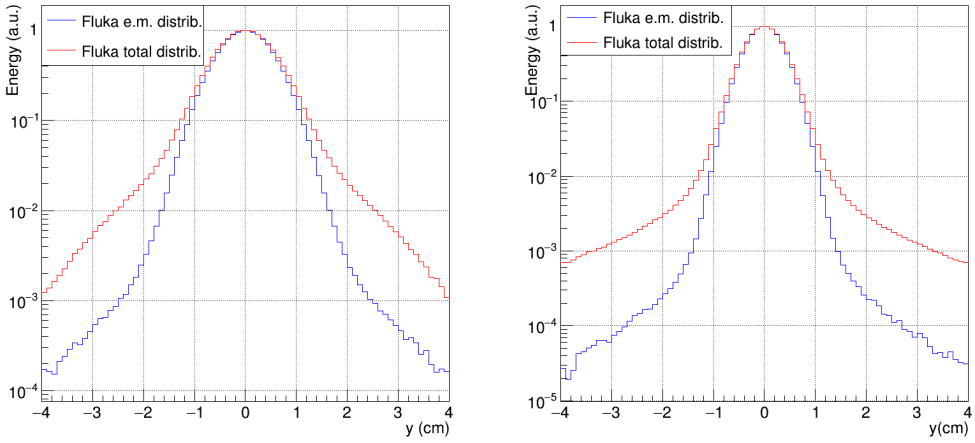

Figure 2.9: Electromagnetic and nuclear contribution for the lateral profile of proton (left) and ^4He beam (right)of energy 150 MeV/u in water at a depth z = 15 cm.

The analytic calculation of the nuclear contributions is a too difficult task and a Monte Carlo approach is still very time consuming: therefore many empirical parametrizations for the nuclear halo are available in literature. Among these it is worth mentioning the approach of Soukup et al. [99] that describes the nuclear halo tails with a modified Cauchy-Lorentz function, the work of Li et al. [115] and the recent review by Gottschalk et al. [116].

The Molière's theory developed in the previous section 2.3 takes into account only the electromagnetic interactions and nuclear interactions are not calculated. At therapeutic energies, the effects of nuclear interactions play an important role because they produce a widening of the lateral profile.
For the implementation of the nuclear interactions in the MONET code, the primary particle weights are evaluated by studying the attenuation of a beam in water. After this step, the parametrization of the tail of lateral profile is added.

2.6.1 Attenuation

When large thicknesses are involved, the nuclear interactions give a contribution to the deposited energy that can be estimated as about 1% [106] and 2% [69] per cm of water depth for proton and Helium beams respectively. This factor accounts for the primary particles fluence decrease and describes the

interactions, that also affect the tails of the lateral distribution.

For **protons** a formula for the fraction W_p of particles of incident kinetic energy E_k and range R, at a certain water thickness z, that undergo only electromagnetic interactions is given by [106]:

$$W_p = \frac{1}{2}\left[1 - \left(\frac{E_k - E_{th}}{m}\right)^f \frac{z}{R}\right]\left[1 + \text{erf}\left(\frac{R-z}{\tau}\right)\right] \tag{2.69}$$

where erf is the error function, $f = 1.032$, m is the proton mass in MeV, $E_{th} = 7MeV$ is the ^{16}O threshold energy for (p, p') reaction. The parameter τ takes into account the range variation due to straggling along the beam path and can be parameterized as in [106].
Therefore, the nuclear interaction weight is represented by the fraction $(1-W_p)$.

For **Helium** beams, I performed a detailed study of attenuation of primary particle using the results of the simulations and experimental data [25].
With FLUKA, I have evaluated the decrease of fluence as a function of depth for each energy analyzed. The attenuation curves are fitted using an error function multiplied by a linear parametrization:

$$W_p = (\alpha z + \beta) \times \text{erf}\left(\frac{R-z}{\gamma}\right) \tag{2.70}$$

where z is the depth in water, R is the range evaluated using the Eq. 2.59 and a, b and c are the free parameters.
The linear parametrization describes the initial part of the attenuation, while the error function represents the decrease to almost zero in the correspondence of the Bragg peak.
Good results are obtained by a best fit with the value of parameters β and γ fixed ($\beta = 1$ and $\gamma = 0.1$). The values of the parameter α for the different energies are reported in Table 2.2: the negative values are justified by the decrease of primary particles.

E(MeV/u)	100	150	200
α	-0.26	-0.22	-0.19

Table 2.2: The values of the parameter α for the attenuation of ^4He ions.

The fit results of the attenuation are reported in Fig.2.10, where the agreement between the simulation and model is good (2%) for the analyzed energies. In the case of ^4He of 200 MeV/u, a comparison with the experimental data [25] are performed: there is a good correspondence between the data and the model (see bottom part of Fig.2.10).

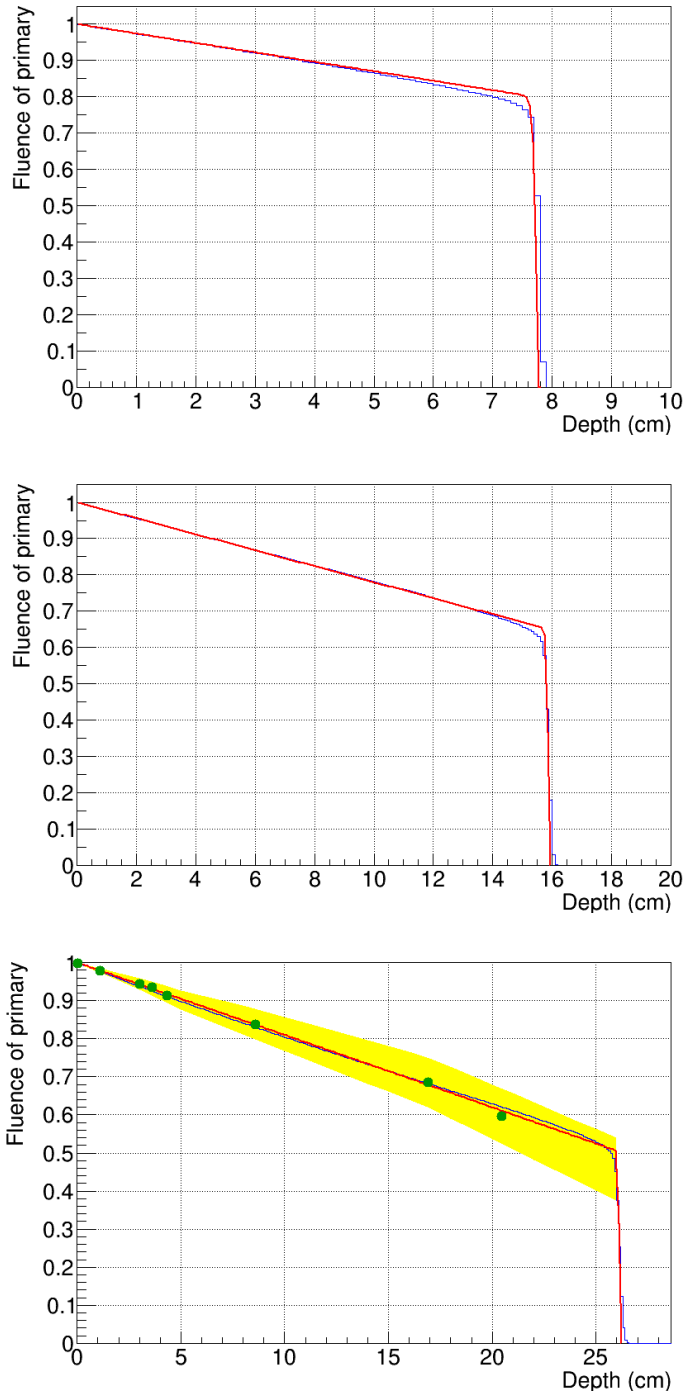

Figure 2.10: The attenuation curve of ^4He ions as a function of depth.
The attenuation curve obtained with FLUKA are reported in blue line and the results of fit with Eq. 2.70 is in red line.
The energy analyzed are: (top) E=100 MeV/u, (middle) E=150 MeV/u and (bottom) E=200 MeV/u.
For 200 MeV/u, the experimental data (green bullet point) and the error estimates (yellow band) from [25] are added for the validation of the curve.

2.6.2 Nuclear parametrization

Concerning the MONET code, once we evaluated the nuclear contribution, we add a parametrization to the curve of the analytical model.
The nuclear effect is well approximated by a Lorentz-Cauchy formula [99] [115]:

$$t(y) = \frac{1 - A \exp\left[-\frac{y^2}{2b^2\sigma^2}\right]}{\pi b \left(\frac{y^2}{b^2} + 1\right)} \tag{2.71}$$

where the free parameters are the amplitude A, the half width half maximum (HWHM) b and the variance σ^2.

In this way, the total normalized distribution for the lateral profile is given by:

$$f(y) = W_p f_M(y) + (1 - W_p) \frac{t(y)}{\int_{-\infty}^{+\infty} t(y) dy} \tag{2.72}$$

Both $f_M(y)$ and $t(y)$ are normalized to unit area, in order to conserve the significance of probability lateral distribution.
The free parameters A, b and σ of Cauchy-Lorentz function have been obtained by a fit to FLUKA simulation with the nuclear interactions switched on. During the fit study, we have found that good results were obtained with the variance fixed ($\sigma = 1$).

In conclusion, for the lateral profile in water, we have implemented a complete model both for protons and for ^4He beams, that considers the electromagnetic interactions (Molière's theory) and nuclear fragmentation with a parametrization (Lorentz-Cauchy formula).

2.7 Results

In this section, the results of the total lateral profile of proton and ^4He beam are reported. I have analyzed three different energies (100, 150 and 200 MeV/u) at different depths and the MONET results are compared with FLUKA simulations. Subsequently, the radial reconstruction for the total lateral profile of protons and ^4He ions are shown.

2.7.1 Proton beam

A selection of the obtained results for proton beams of different energies at two depths each are shown in Fig. 2.11.
In any analyzed case, I find a general good agreement with the FLUKA simulations within 1%. For 100 MeV at 7 cm, the model seems to overestimate the MC distribution at large lateral distance (note the log scale), but in most

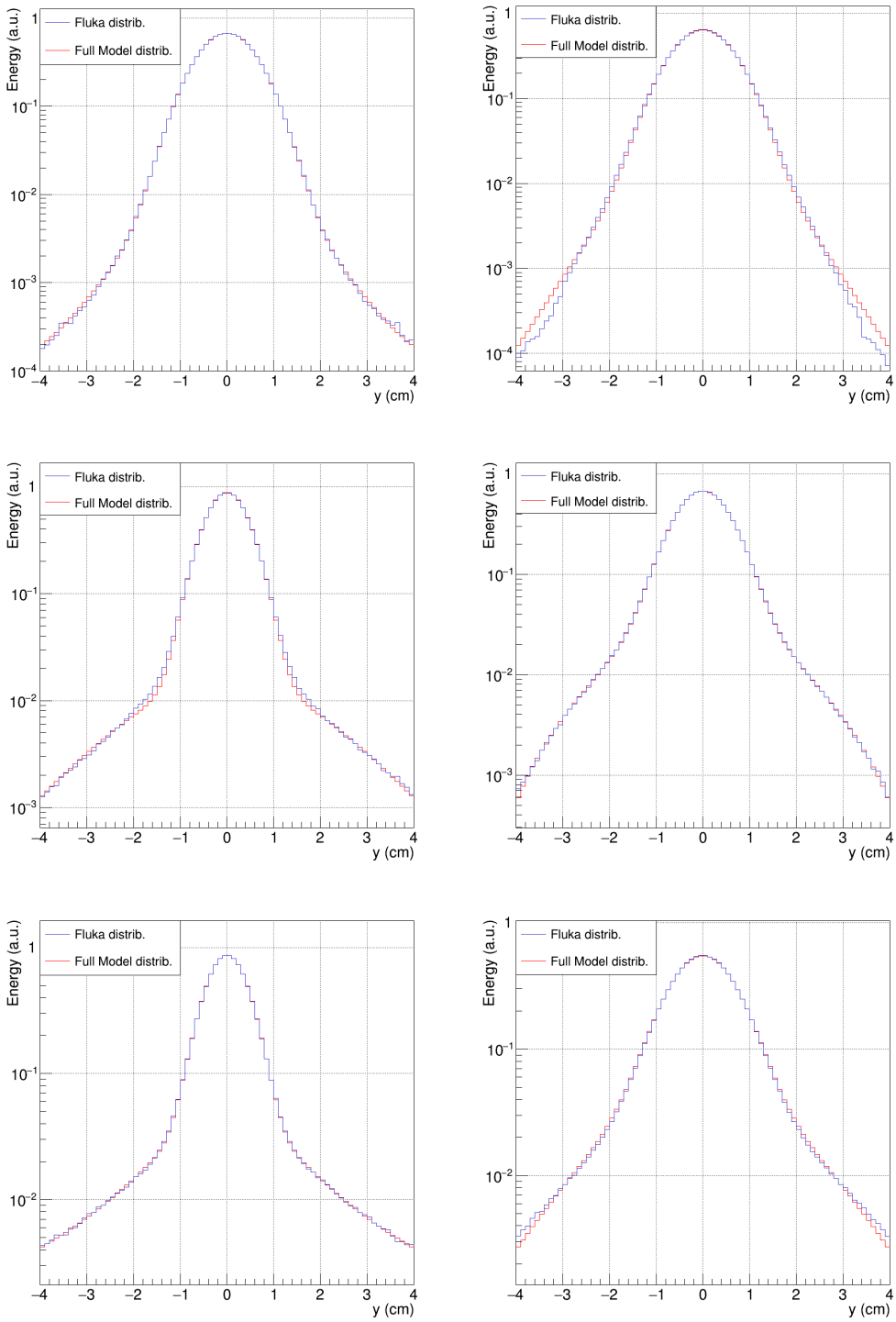

Figure 2.11: Lateral distributions of proton beam in water at a different depth.
Top: E=100 MeV at z= 4 (left) and z= 7 (right) cm.
Middle: E=150 MeV at z= 7 (left) and z= 15 (right) cm.
Bottom: E=200 MeV at z= 15 (left) and z= 25 (right) cm.

of cases the agreement is very good.

In order to compare the predictions of the model to a realistic situation of proton beam broadening in water, we used experimental data acquired at the HIT Heidelberg Ion Beam Therapy Center [51].
These dosimetric measurements were performed in a water phantom with entrance window at the treatment isocenter, using a special arrangement of 24 PinPoint ionization chambers (PTW Freiburg, type 31015, 0.030 cm^3 active volume) with six rows of four chambers aligned in lateral offset patterns (in beam-eye view) not to shadow each other, and controlled by a step motor. Lateral profiles were sampled at different depths in water by repeated acquisitions at horizontally shifted positions of the detector block for irradiation of a vertically scanned line pattern of 10 cm length and 1 mm scanning step size. The errors on the data range from 2% to 15%, going from the high dose points to the lowest dose regions. More details of the experimental setup can be found in Schwaab et al.[51].

The comparisons shown in [79] refer to initial beam energies of 81.49 MeV and 158.58 MeV and to beam sizes of 17.55 and 10.7 mm FWHM in air at the isocenter.

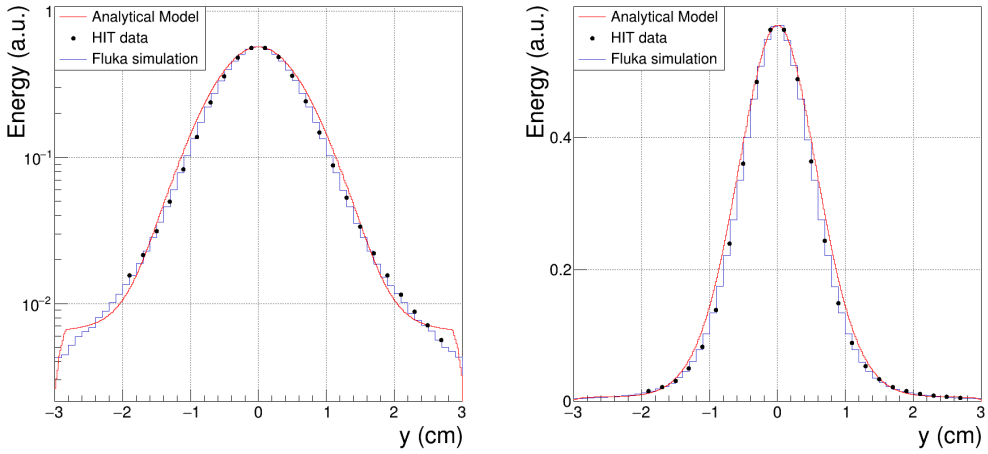

Figure 2.12: Comparison between model, FLUKA simulation and experimental data for 158.58 MeV in water for a thickness of: z=6.55 cm in logarithmic (left) and linear (right) scales. The MONET and FLUKA curves are normalized to the maximum of the experimental data.

In Figure 2.12 the experimental data are compared with the FLUKA simulation and the calculation of the model.
In the comparison between model and data, the detector effect that should be considered. This effect can be taken into account through the parabolic

normalized resolution function [51]:

$$S(x) = \frac{2}{\pi R^2}\sqrt{R^2 - x^2} \text{ when } x < R \text{ , 0 otherwise,} \tag{2.73}$$

where x is the lateral position and R is the effective detector radius, quoted as $R = 0.145$ cm. To correct these effects, we convolute this function with model distributions, resulting after the convolution with the beam. The inclusion of detector size does not significantly modify the agreement with data.

We have found that in any case FLUKA and the MONET calculations agree very well, and that the agreement with the measurement data is good.

2.7.2 Helium beam

The results for ^4He beams of energies (100, 150 and 200 MeV/u) are shown in Fig. 2.13.
In any analyzed case, we find a general good agreement with the FLUKA simulations within 1%. At low energy (100 MeV), the model seems to overestimate the MC distribution at large lateral distance, but with increasing energy and depth, the agreement improves considerably.
A further comparison between our model and the parametrization currently used in hadrontherapy is shown in Appendix B. The results show that MONETα are equivalent or even better and require a smaller number of free parameters than the other methods.

2.7.3 Radial distributions

The 2D reconstruction corresponding to the projected profile of figure 2.14-2.15 (left) is shown in figure 2.14-2.15(right) respectively. The results of equations 2.65-2.68 are compared with the radial distribution obtained with FLUKA simulations and the agreement is about 2%.
In conclusion, the model's calculations agree very well with simulation in the case of protons and ^4He beams at therapeutic energies.

2.8 Conclusions

This chapter are presented an accurate model for the lateral profile based on Molière theory for the multiple Coulomb scattering and a Cauchy Lorentz function for the nuclear interactions.
The model calculates the lateral profile considering the projected distribution. This choice is due to many reasons: in particular, the convolution with beam size and the fit of nuclear contributions are simpler to evaluate. With the

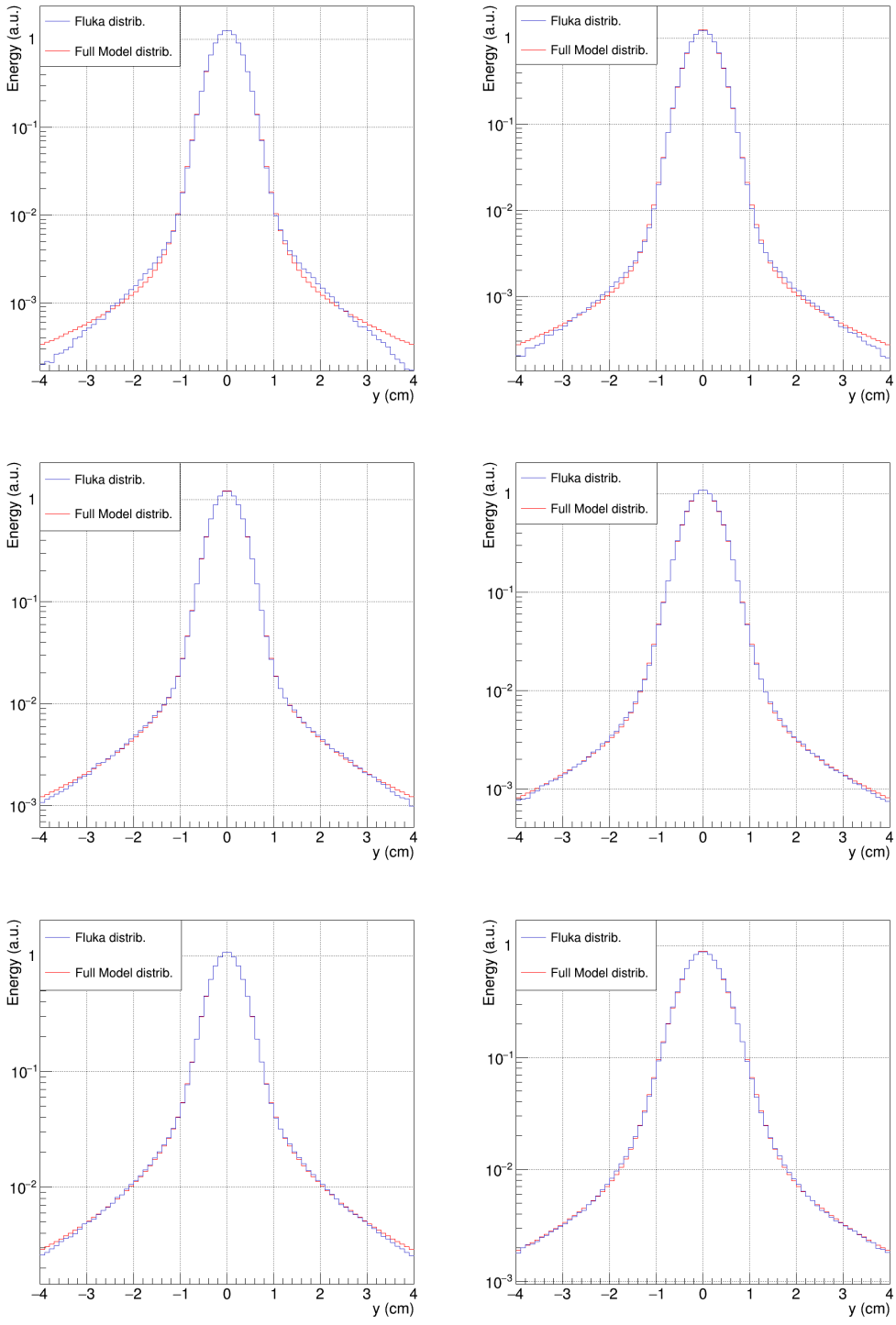

Figure 2.13: Lateral distributions of ^4He beam in water at a different depth.
Top: E=100 MeV/u at z= 4 (left) and z= 7 (right) cm.
Middle: E=150 MeV/u at z= 7 (left) and z= 15 (right) cm.
Bottom: E=200 MeV/u at z= 15 (left) and z= 25 (right) cm.

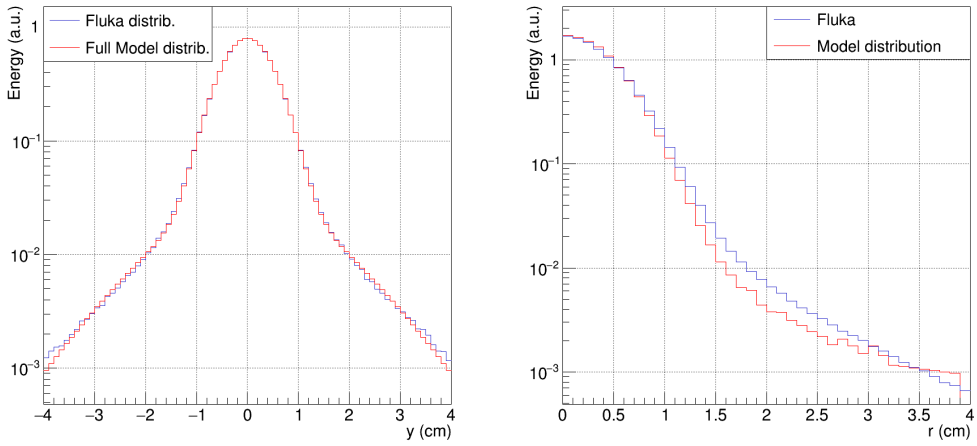

Figure 2.14: Lateral distributions (left) and radial distributions (right) for 150 MeV protons in water at a depth z = 11 cm.

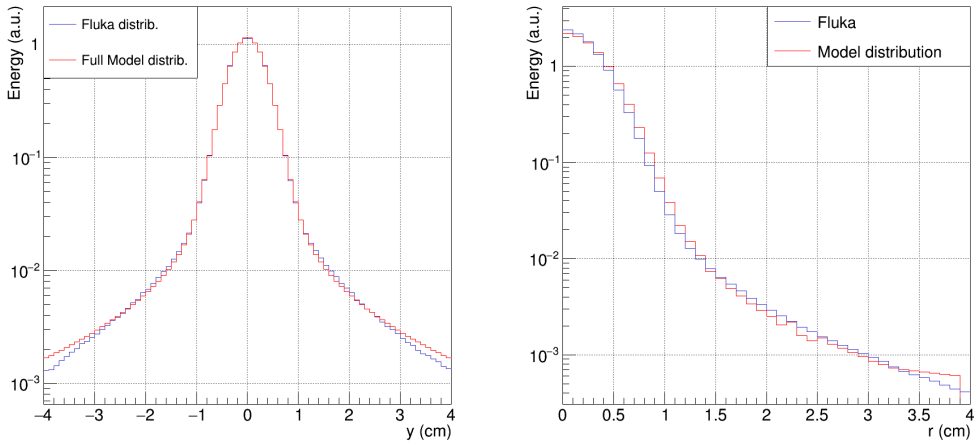

Figure 2.15: Lateral distributions (left) and radial distributions (right) for 150 MeV/u ^4He beam in water at a depth z = 11 cm.

implementation of Papoulis algorithm, MONET is able to reconstruct the 2-dimensional lateral distribution, starting from the projected one.
A comparison with the results of Fermi Eyges theory has been also presented to underline the better accuracy of the Molière distribution and the novelty of our approach.
The tails of the lateral distribution due to nuclear interactions are well described by the Cauchy Lorentz function with only two free parameters, obtained with a fit of FLUKA calculations.
The comparison with FLUKA, at three different energies and different depths, shows an agreement between MONET and MC simulations.
Therefore, MONET is able to reproduce the lateral distribution of protons

and ^4He beams in water, with the same order of accuracy as MC methods, but with shorter computation time.

Chapter 3

The Longitudinal Profile

In hadrontherapy, the knowledge of depth-dose curves, or Bragg curves, is a fundamental prerequisite for the evaluation of the dose in the treatment plan of a patient.
The MONET code provides an accurate model of the Bragg curve that has a physical basis and is valid for therapeutic energies that could compete with Gaussian models or with MC codes for validation studies even in the clinical practice.

3.1 Physical processes

The range of a hadron depends on its energy and this effect is at the heart of therapy with protons and ions.
As a heavy charged particle moves through the patient medium, it loses energy and consequently its stopping power and ionization effects change. In particular, the stopping power increases with the decreasing of the residual energy of the particle. Therefore as the particle looses energy, it causes more ionization until it reaches the highest point of ionization at the **Bragg peak**. After the Bragg Peak, the particles have lost almost all of their energy and are neutralized by attracting electrons from the surrounding atoms.
The longitudinal profile is characterized by three processes:

- Energy loss;
- Straggling;
- Nuclear interactions;

and the single contribution of all these interactions is shown in Fig. 3.1.

3.1.1 Energy loss

The longitudinal dose profile is mainly determined by the stopping process of projectile due to inelastic collisions with the atomic electrons.

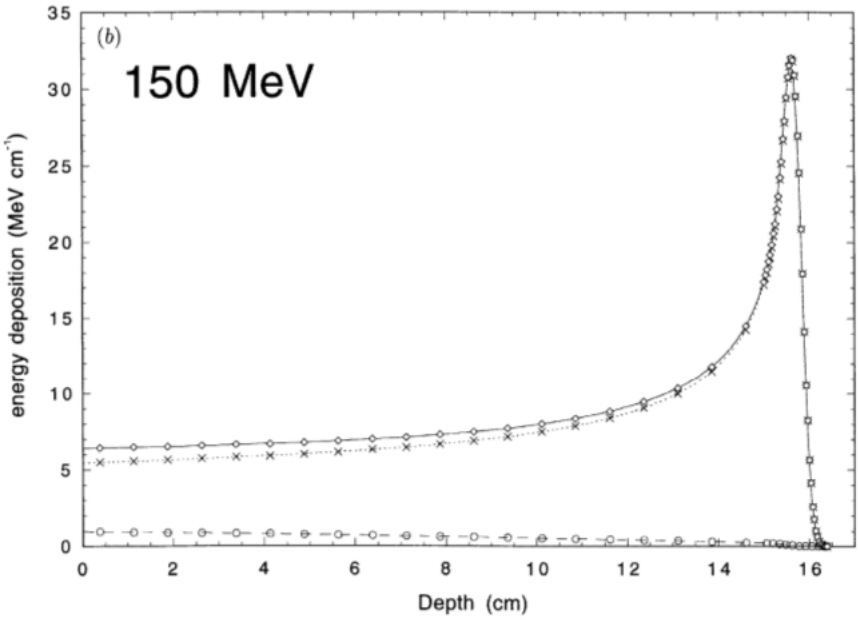

Figure 3.1: Total energy deposition for proton beam of 150 MeV from [57]: the total dose distribution (solid line), the contributions from Coulomb ($\times$ bullets) and inelastic nuclear interaction ($\circ$ bullets) are shown.

In these collisions, the energy is transferred from the particle to the atom causing ionization or excitation of the latter. The maximum energy transferred in each collision is generally a very small fraction of the initial kinetic energy; however, in dense material as water, the number of collision per unit path length is so large, that a substantial cumulative energy loss is observed.

3.1.2 Straggling

The statistical nature of the energy loss process must also be taken into account, due to the high number of collisions for energies and thicknesses typical of hadrontherapy.
The details of the microscopic interactions undergone by any specific particle vary randomly and the energy loss is a stochastic process. In fact, due to this statistical effect, a monoenergetic beam of incident particles gets a finite width in its energy distribution as it travels through the material. This is called range straggling or energy straggling if we focus on fluctuations in energy loss rather than range.
Due to the straggling, the shape of the longitudinal profile changes specially at the end of the particle track: the Bragg peak is less sharp and the curve has a small tail at the end. The straggling effect is shown in Fig. 3.2 with reference to the curve obtained considering only the energy loss processes.

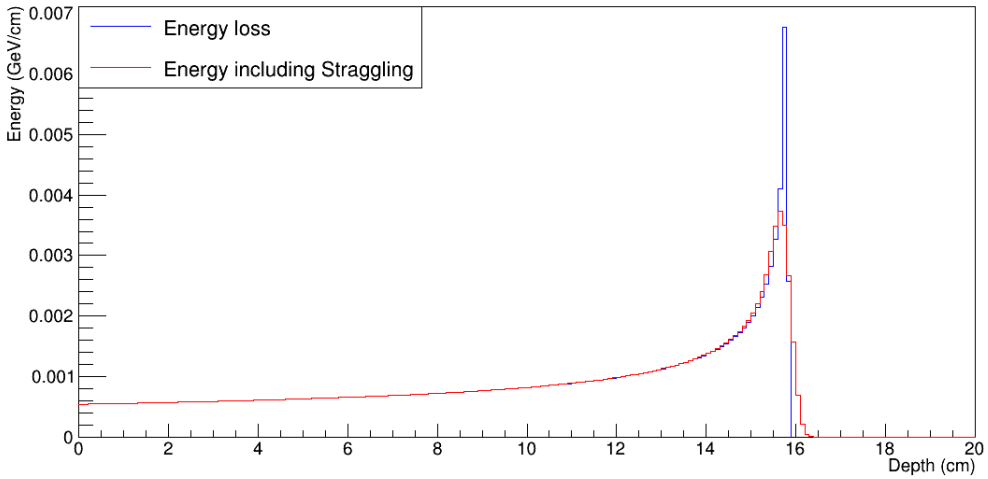

Figure 3.2: Bragg curves obtained with FLUKA simulation: average energy loss (blue line) and energy loss including straggling (red line).

3.1.3 Nuclear interactions

In the evaluation of the longitudinal profile, nuclear interactions play an important role by reducing the fluence of the primary particles.
Due to nuclear reactions particles are removed from the electromagnetic peak and their secondaries deposit their energy upstream. Another effect of the nuclear interactions is a small buildup of nuclear fragments in the entrance region. After the end of the nozzle, the beams travel in air, where the nuclear secondaries are few, due to the low density of the medium. The nuclear interactions increase as soon as the beam hits the patient, but the equilibrium situation is reached after few centimeter (the characteristic range of secondary particles). Therefore, nuclear interactions increase in the entrance region and decrease near the peak.
When a projectile hits a target nucleus, light particles are promptly emitted and an excited projectile and an excited target are formed. These excited nuclei decay through consecutive light particle emissions (evaporation process) or by a prompt break-up (fragmentation process).
Nucleus-nucleus collisions have two main effects. The first one is the disappearance of the projectile since the collision will change its nature. As a consequence, the projectile will not deposit its energy up to the Bragg Peak. The second effect is the secondary particle production. These fragments will be smaller, but with a velocity close to velocity of the projectile. Because of the A/Z^2 scaling of the range for particles with the same velocity, these fragments will deposit their energy at penetration depths beyond the projectile Bragg Peak.
The inelastic nuclear interaction give rise to different kinds of charged particles

(protons, deuterons, alpha particle and heavier nuclear fragments) as well as uncharged particles (gamma rays and neutrons). The charged particles impart all energy locally whereas the uncharged particles can escape to the target region and release energy in the normal tissue.

Proton beam

For proton beams, only target fragmentation is possible. The electromagnetic interactions of protons dominate, but nuclear reactions are not rare enough to be neglected.
At the energies typical of hadrontherapy, the possible secondaries from nonelastic reactions are protons, neutrons, γ rays, heavy fragments such as α and the recoiling residual nucleus. Heavy fragments other than α are in fact quite rare. The most probable nuclear reaction for a proton beam in water are [106]:

1. $p + {}^{16}_{8}O \rightarrow n + {}^{16}_{9}F$
2. $p + {}^{16}_{8}O \rightarrow n + p + {}^{15}_{9}O$
3. $p + {}^{16}_{8}O \rightarrow p + p + {}^{15}_{7}N$
4. $p + {}^{16}_{8}O \rightarrow \alpha + {}^{13}_{7}N$
5. $p + {}^{16}_{8}O \rightarrow d + {}^{15}_{8}O$
6. $n + {}^{16}_{8}O \rightarrow p + {}^{16}_{7}N$
7. $n + {}^{16}_{8}O \rightarrow n + p + {}^{15}_{7}N$

where reactions 6 and 7 result from 1 and 2. All types of β^+ decay produce one γ of energy in the order $0.6 - 1MeV$ and their half mean life varies between few second to minutes.
An example of the secondary particles yield in percentage is shown in Tab.3.1. The results are obtained by a Monte Carlo simulation [117].

p	d	t	^3He	α	Recoils	n	γ
0.57	0.016	0.002	0.002	0.029	0.016	0.2	0.16

Table 3.1: Fragments produced by $150MeV$ proton beams on ^{16}O target.

Helium beam

Helium has a unique structure: it is a double magic nucleus, a bound system with a high binding energy. Therefore, the ^4He ions suffer less projectile fragmentation than ^{12}C ions.
The depth dose profile of ^4He is characterized by a tail behind the Bragg peak.

At therapeutic energies, the secondaries are the hydrogen isotopes: protons, deuterons and tritons and neutrons, with similar penetration depth.
The reaction channels for ^4He with Hydrogen are [75]:

- $^4He + p \rightarrow^2 H +^3 He$
- $^4He + p \rightarrow p + p +^3 H$
- $^4He + p \rightarrow p + n +^3 He$
- $^4He + p \rightarrow p +^2 H +^2 H$
- $^4He + p \rightarrow p + p + n +^2 H$
- $^4He + p \rightarrow p + p + p + n + n$

Due to nuclear fragmentation, the ^4He ions decrease with increasing depth and the ^3He ions increase reaching the maximum in the correspondence of the Bragg peak. The hydrogen isotopes have a broad energy distribution, but their dose contribution is smaller than that of ^4He primary particles, as the small size of the tail indicates.

3.2 MONET implementation

In the following, the formulas proposed are valid for therapeutic energies (50-220 MeV for protons and 50-250 MeV/u for Helium beams) in water.
Any physical processes is benchmarked with FLUKA: in the Monte Carlo simulation, the physical process can be easily switched on or off and this is an important tool for the verification of our formulas. No reference is made to experimental data since FLUKA for protons and Helium beam [118] [77] in water is already validated, as testified by its use in different facilities like HIT or CNAO.

3.2.1 Energy loss computation

For the evaluation of the mean energy loss, the only information needed are the initial energy and the corresponding range, that can be easily calculated with the accurate formula (Eq. 2.59).
In the MONET code, the evaluation of the average energy loss is based on 2.43:

$$p(z)^2\beta(z)^2 = p^2\beta^2(1 - \frac{z}{R})^k \tag{3.1}$$

where R is the CSDA range for incident particle of momentum p and velocity β, $p(z)$ and $\beta(z)$ are the momentum and velocity of the particle at the depth z and $k = 1.07$ in water.
Since $p\beta$ can be written as:

$$\frac{p}{E} = \frac{E_T^2 - m^2}{E_T} \tag{3.2}$$

where E_T is the total energy ($E_T = E_k + m$, E_k kinetic energy), the equation 3.1 can be rewritten:

$$\frac{E_k^2 + m^2 + 2mE_k - m^2}{E} = \frac{E_k^2 + 2mE_k}{E_k + m} = p\beta \left(1 - \frac{z}{R}\right)^{k/2} \equiv F(z) \qquad (3.3)$$

Solving the quadratic form, we obtain the expression of the kinetic energy as a function of depth z:

$$E_k(z) = -m + \frac{F(z)}{2} + \sqrt{m^2 + \frac{F^2(z)}{4}} \qquad (3.4)$$

Equation Eq. 3.4 is valid both for proton and Helium beams, considering the initial energy of the beam and the different range evaluation.

3.2.2 Straggling computation

For a complete description of the longitudinal profile, we have also considered the statistical variations in the energy lost by the incident particle the so called straggling.
A good approximation for the straggling is given by a Gaussian distribution around the mean depth $\bar{z}$. The energy deposed can be obtained by the convolution of the analytical dose (Eq. 3.4) with a Gaussian function [53] of standard deviation $\sigma(\bar{z})$:

$$\hat{E}_k(z) = \int_0^R E_k(\bar{z}) \frac{e^{-(z-\bar{z})^2/2\sigma^2(\bar{z})}}{\sqrt{2\pi}\sigma(\bar{z})} d\bar{z} \qquad (3.5)$$

Since the longitudinal profile is extremely flat until the end, only the last part including the Bragg peak will be significantly affected by a convolution.

For **protons**, in the MONET code we have computed the convolution numerically, using the approximation found in [106]:

$$\bar{\sigma} \approx 0.012 R^{0.935} \qquad (3.6)$$

In the case of **Helium beam**, the energy deposition with straggling is evaluated by a convolution with a Gaussian of $\sigma(\bar{z})$:

$$\bar{\sigma} \approx 0.012 R^{s} \qquad (3.7)$$

where the s values are tuned on the FLUKA depth dose profile including straggling.

In Fig. 3.3, the straggling value s scale with energy with a simple polynomial function:

$$s = \sum_{i=0}^{2} a_i E^i \qquad (3.8)$$

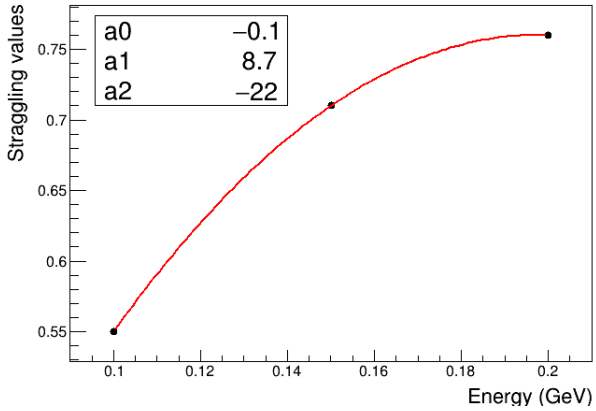

Figure 3.3: The parameter s as a function of energy: the parameters are fitted with polynomial function.

3.2.3 Nuclear interactions evaluation

To complete the longitudinal dose profile, also the nuclear contributions due to secondary particles and fragments are included in the MONET calculation.

For **proton beams**, the expression of the deposited energy becomes:

$$f_z(z) = W_p \hat{E}_k(z) + (1 - W_p) E_N(z) \tag{3.9}$$

where the first term represents the energy deposition of the primary particles and the second is the contribution of nuclear interactions. The electromagnetic and nuclear contribution are weighted for the primary particle weight and for the nuclear contribution respectively, according to Eq. 2.69.
To the electromagnetic contribution, the nuclear interaction is added with a simple model that requires two free parameters to be adjusted at each energy. The energy deposited by the nuclear fragments $E_N(z)$ is added using a linear parametrization, according to [57]:

$$E_N(z) = a'(E)z + b'(E) \tag{3.10}$$

where the coefficients a' and b' are obtained by fitting the FLUKA results in the presence of the nuclear interactions.

Also in the case of **Helium ions**, the nuclear interactions are described with a linear parametrization weighted for the nuclear contribution $(1 - W_p)$. The evaluation of W_p is done using Eq. 2.70 and the values of the parameters reported in Table 2.2.
In addition to the proton case, there is however an important contribution to the dose beyond the Bragg peak, due to nuclear fragmentation.

3.2.4 Fragmentation tail

The fragmentation of ^4He ions in the target leads a tail after the Bragg peak. In the case of proton beams, this effect is negligible.
A preliminary study of the tail of ^4He ions in water is performed here. The depth dose curve from FLUKA simulations are analyzed, focusing in the few centimeters after the peak.
The description of this contribution is based on the search of **practical range**, following the approach of [81]. The practical range R_p is defined as the depth corresponding to the intersection point between the tangent at the inflection point of the descending part of the depth dose profile and the exponentially extrapolated fragmentation tail (Fig. 3.4).

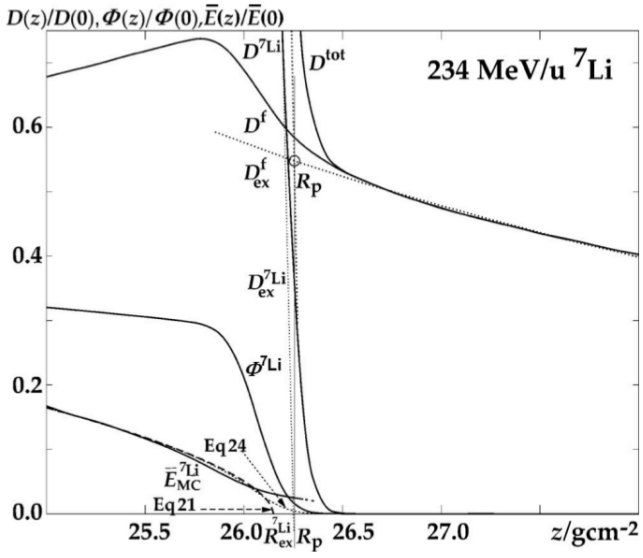

Figure 3.4: Practical range R_p from [81] : the tangent at the inflection point and the exponentially extrapolated background dose of fragments.

To include the ^4He fragmentation tail, we consider:

- before the practical range: the tangent at the inflection point
- after the practical range: the exponential tail

in the calculation of energy deposition. Therefore the total energy deposition for ^4He ions is given by:

$$f_z(z) = \begin{cases} W_p \hat{E}_k(z) + (1 - W_p)(a'z + b') & 0 < z < R \\ mz + q & R < z < R_p \\ \exp(p_0 + p_1 z) & z > R_p \end{cases} \tag{3.11}$$

where m and q are the parameter of the tangent at the inflection point and the p_0 and p_1 the parameters of the exponential fit of the tails.
The modelization of the fragmentation tail of ^4He is validated with FLUKA simulations and the agreement is good.

3.3 Results: Proton beam

Here, a benchmark with FLUKA simulations of the formulas for the energy loss, straggling and nuclear interaction for proton beams in water is presented.

3.3.1 Energy loss

The new formula implemented in MONET for the evaluation of average energy loss Eq.3.4 is similar to the relation already published:

$$E'_k(z) = E_k(0)\left(1 - \frac{z}{R}\right)^{1/p} \tag{3.12}$$

where $E_k(0)$ is the initial beam energy and $p = 1.77$ in water, which has been verified to be in agreement with data within the measurement errors for various energies and media [53] [81].
In Fig. 3.5, the comparison of the Bragg curve from FLUKA with those from Eqs. 3.4-3.12 are reported. I have analyzed different therapeutic energies and our formula Eq. 3.4 is in good agreement with FLUKA simulations within 1%.

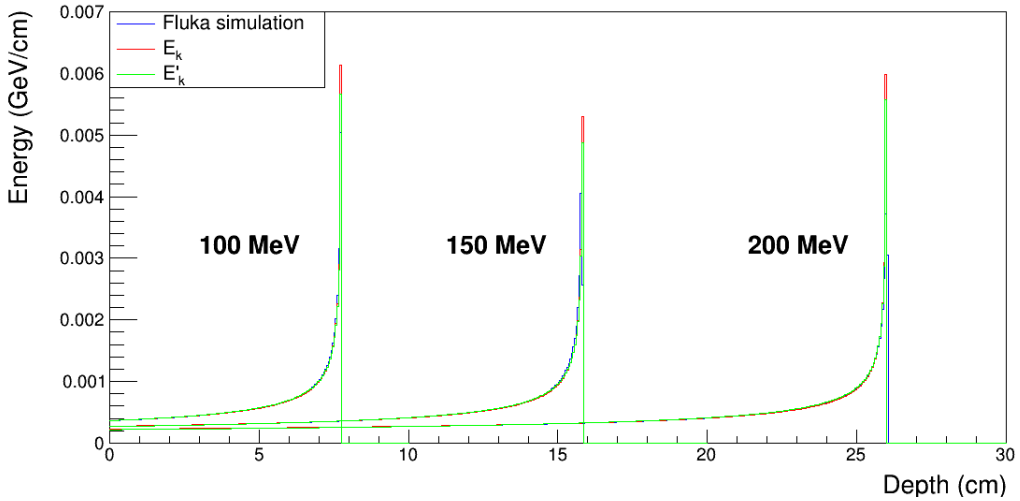

Figure 3.5: Bragg curves calculated with equations (3.4) and (3.12) compared with FLUKA simulations for three different energies $(100, 150, 200$ MeV).

3.3.2 Straggling

The validation of Eq. 3.5 for the straggling effect has been performed including the straggling in the FLUKA simulations. The result is shown in Fig. 3.6, where the agreement with MC calculation is still good (1%).

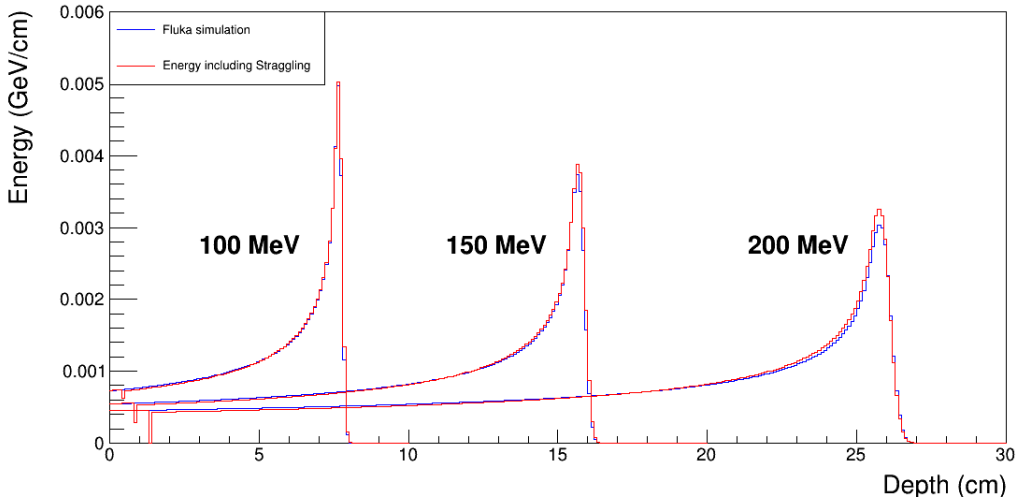

Figure 3.6: Bragg curves including straggling effects for $E = 100, 150, 200$ MeV.

3.3.3 Total energy loss

The total energy deposition from Eq. 3.9 including the nuclear interaction is compared with FLUKA in Fig. 3.7.
By looking at the plot in Fig. 3.7, we see a good agreement within 1% of the MONET calculation with FLUKA for all energies up to 150 MeV. These results are very sensitive to the CSDA range value.
In Fig. 3.6 we can see that, above 150 MeV, the agreement with the FLUKA simulation is not very good: the difference on the Bragg Peak is about 7%. Therefore, in the final curve of Fig. 3.7, we increased linearly the CSDA range by 3‰ for 200 MeV.
The corresponding parameters of the nuclear contribution a and b as a function of energy are reported in Fig. 3.8. The parameters of Eq. 3.10 scale with energy with a simple polynomial function given by:

$$a'(E) = \sum_{i=0}^{3} a'_i E^i \ , \qquad b'(E) = \sum_{i=0}^{3} b'_i E^i \tag{3.13}$$

where the values of the coefficients a'_i and b'_i are those reported in the plots. These parameters allow the immediate calculation of the full dose longitudinal

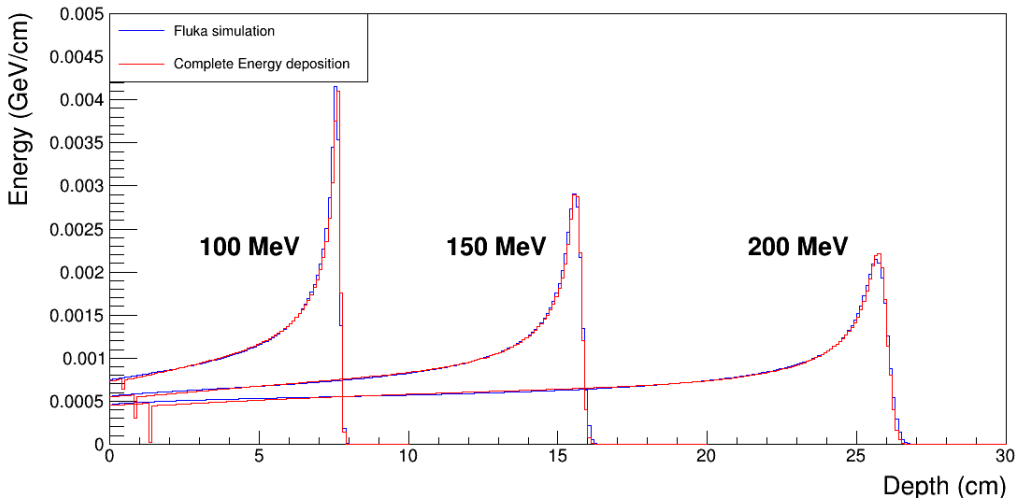

Figure 3.7: Bragg curves including straggling effects and nuclear contributions for $E = 100, 150, 200$ MeV.

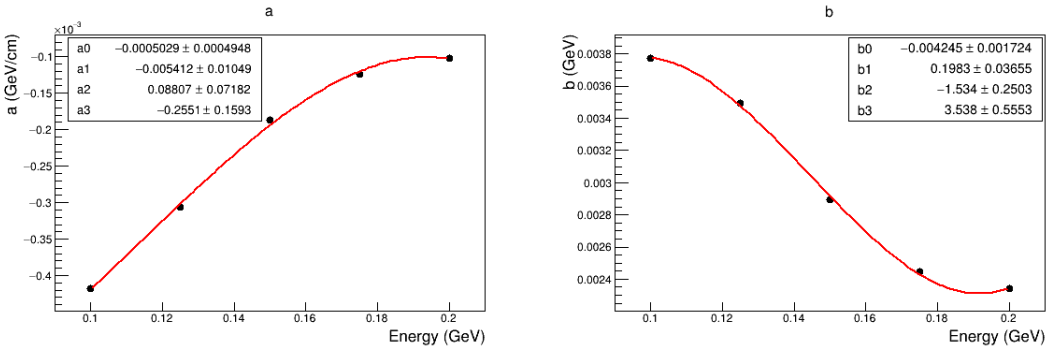

Figure 3.8: Plot of the a' and b' parameters for the longitudinal nuclear contributions for $E = 100, 125, 150, 175, 200$ MeV.

profile for each therapeutic energy of protons in water.

As a further test of the accuracy of Eq. 3.9, the incident and the corresponding energy fraction deposited in the phantom are reported in Table 3.2. The energy missing corresponds to energy escaping in form of uncharged secondary particles, created in the nuclear reaction.
Looking at Table 3.2, the values evaluated with MONET are in agreement with the FLUKA simulation within 1% and they are similar to the results reported in [57].

	MONET	FLUKA
Primary Energy (MeV)	Energy deposited (MeV)	Energy deposited (MeV)
100	96.3	96.9
150	141.3	143.0
200	182.5	184.5

Table 3.2: Comparison between the primary energy and the energy deposited evaluated with FLUKA and the MONET code. The sizes of the phantom are $-4 < x < 4$, $-4 < y < 4$ and $0 < z < 10, 20, 30$ respectively for protons of 100, 150 and 200 MeV.

3.4 Results: Helium beam

In this Section, the benchmark with FLUKA simulations of the formulas for evaluation of energy deposition of ^4He ions in water, considering contribution of the energy loss, straggling and nuclear interaction is presented.

3.4.1 Energy loss

In Fig. 3.9, the comparison of the Bragg curve from MONETα and FLUKA simulation shows a good agreement within 1%.
The formula implemented for the evaluation of average energy loss is also valid for ^4He with the same order of accuracy of the proton beams.

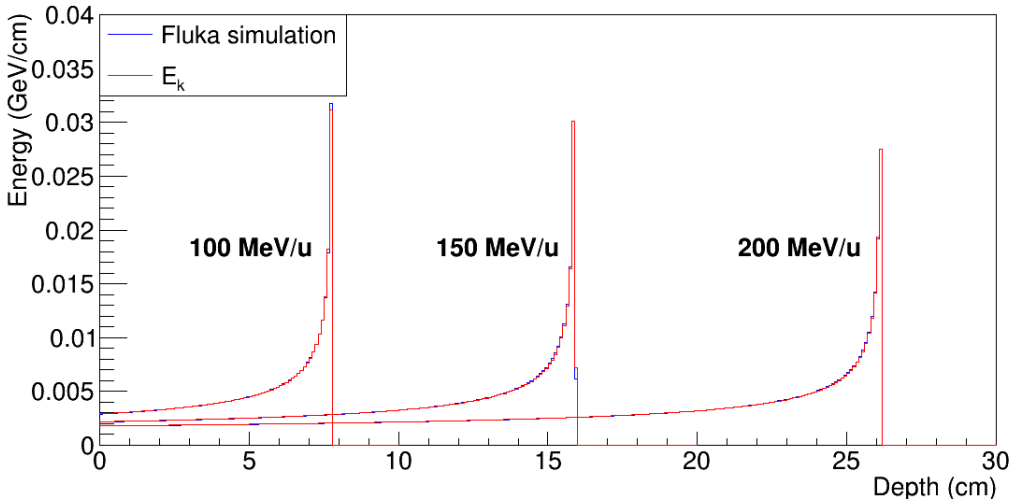

Figure 3.9: Bragg curves of ^4He ions calculated with MONETα compared with FLUKA simulations for three different energies (100, 150, 200 MeV/u).

3.4.2 Straggling

The equation (Eq. 3.5) and the values (Table 3.7) for the straggling of ^4He ion are validated with a FLUKA simulation that includes the straggling effect. The results of MONETα are shown in Fig. 3.10, where the agreement with MC calculation is still good (1%).

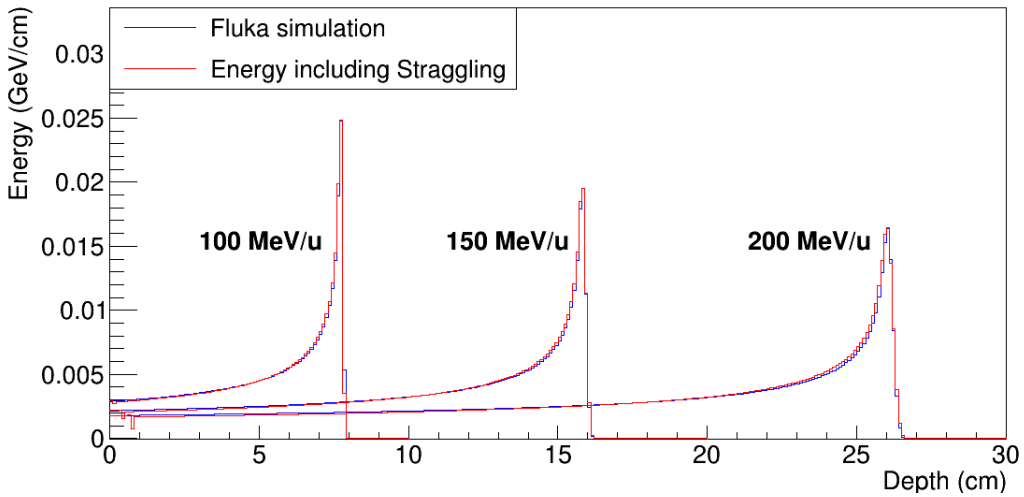

Figure 3.10: Bragg curves including straggling effects of ^4He ions calculated with MONETα compared with FLUKA simulations for three different energies $E = 100, 150, 200$ MeV/u.

3.4.3 Total energy loss

The total energy deposition, including the nuclear interaction and the fragmentation tail, is compared with FLUKA in Fig. 3.11-3.13.
In Fig. 3.11-3.13 the description of dose-depth distribution is reported at the top, while the detail of the search of practical range is shown at the bottom part. An the top of Fig. 3.11-3.13, the inset plot reports a zoom on the fragmentation tail in logarithmic scale, in order to underline the accuracy of the new formula for the fragmentation tails.
The tail of the energy-depth distribution is evaluated with Eq.3.11, using the tangent and an exponential function.
The practical range is evaluated using numerical algorithms implemented in the code. In particular, the procedure starts with the evaluation of inflection point of the descending part of the depth dose profile by looking for the zero of the 2nd derivative using standard numerical techniques [119]. The second step is the evaluation of the intersection of the tangent and the exponential fit of the tail using a numerical algorithm implemented in ROOT. The search of the practical range is underlined in Fig. 3.11-3.13(bottom), where the tangent

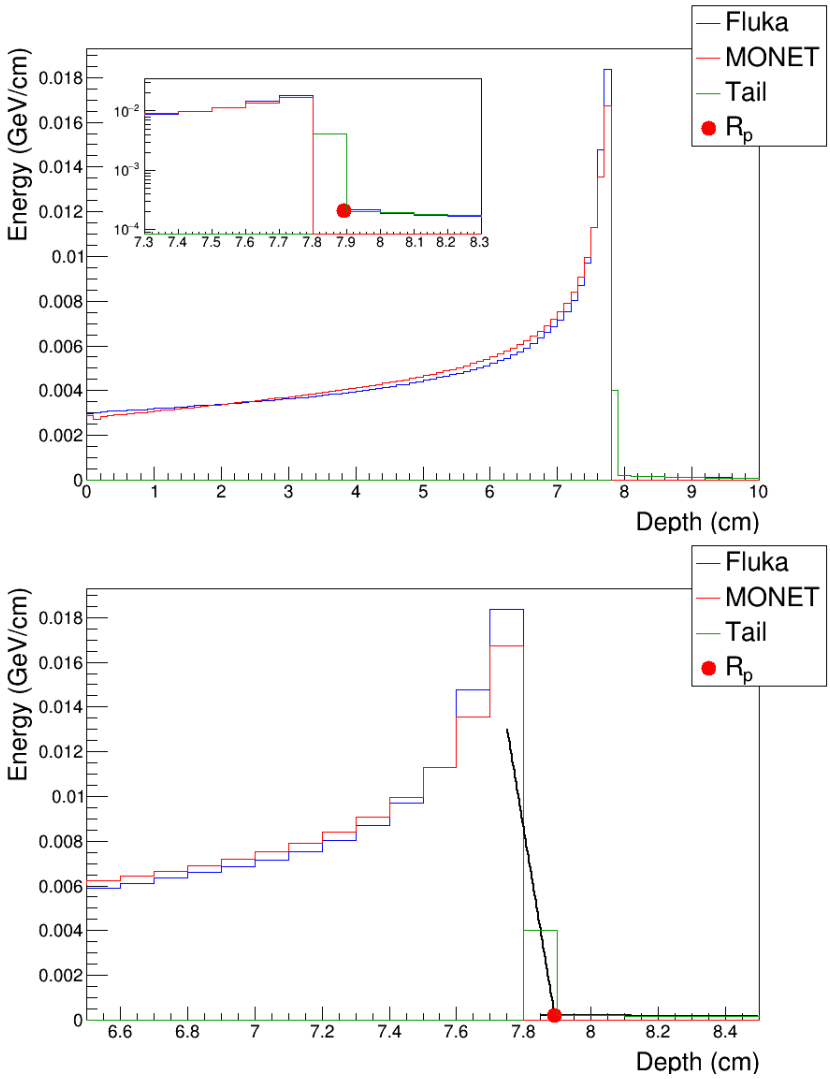

Figure 3.11: Top: Bragg curves including nuclear contributions of ^4He ions calculated with MONETα compared with FLUKA simulations for 100 MeV/u. The bullet point represent the practical range R_p. In the inset plot, a zoom of fragmentation tail is reported in logarithmic scale. Bottom: the practical range as the intersection between tangent at inflection point and the exponential tail is reported.

and the exponential tail are reported.
In Fig. 3.11-3.13, we can see a correspondence between the MONETα calculation and FLUKA. In case of the 100 MeV/u, the model underestimates the energy on the Bragg peak, but the agreement increases with energy.
The new description of the tail is in good agreement with the FLUKA simulations within 3%, as indicated in the inset plot. For ^4He of 200 MeV/u, the fragmentation tail is longer than for the previous cases, but the MONETα

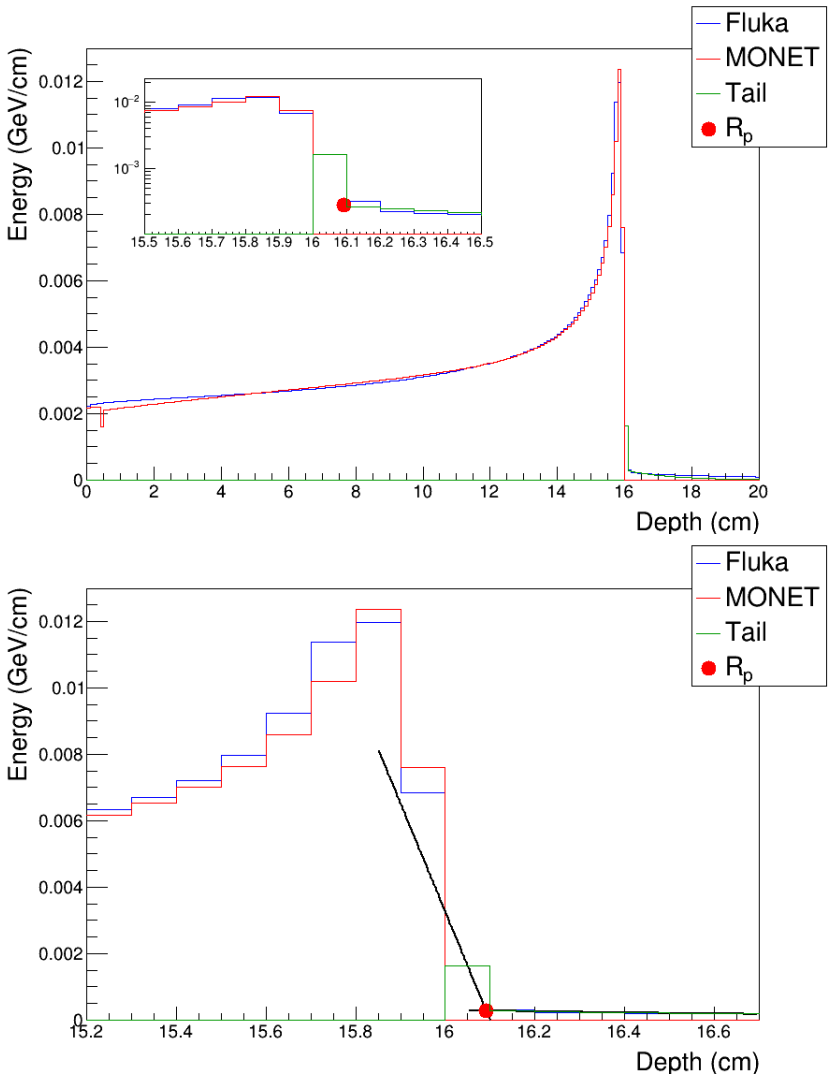

Figure 3.12: Top: Bragg curves including nuclear contributions of ^4He ions calculated with MONETα compared with FLUKA simulations for 150 MeV/u. The bullet represent the practical range R_p. In the inset plot, a zoom of fragmentation tail is reported in logarithmic scale. Bottom: the practical range as the intersection between tangent at inflection point and the exponential tail is reported.

description can be considered satisfactory.

The corresponding parameters of the nuclear contributions of Eq.3.10 are reported in Fig. 3.14. The parameters a and b scale with energy with a simple polynomial function, given by:

$$a'(E) = \sum_{i=0}^{3} a'_i E^i \ , \qquad b'(E) = \sum_{i=0}^{3} b'_i E^i \tag{3.14}$$

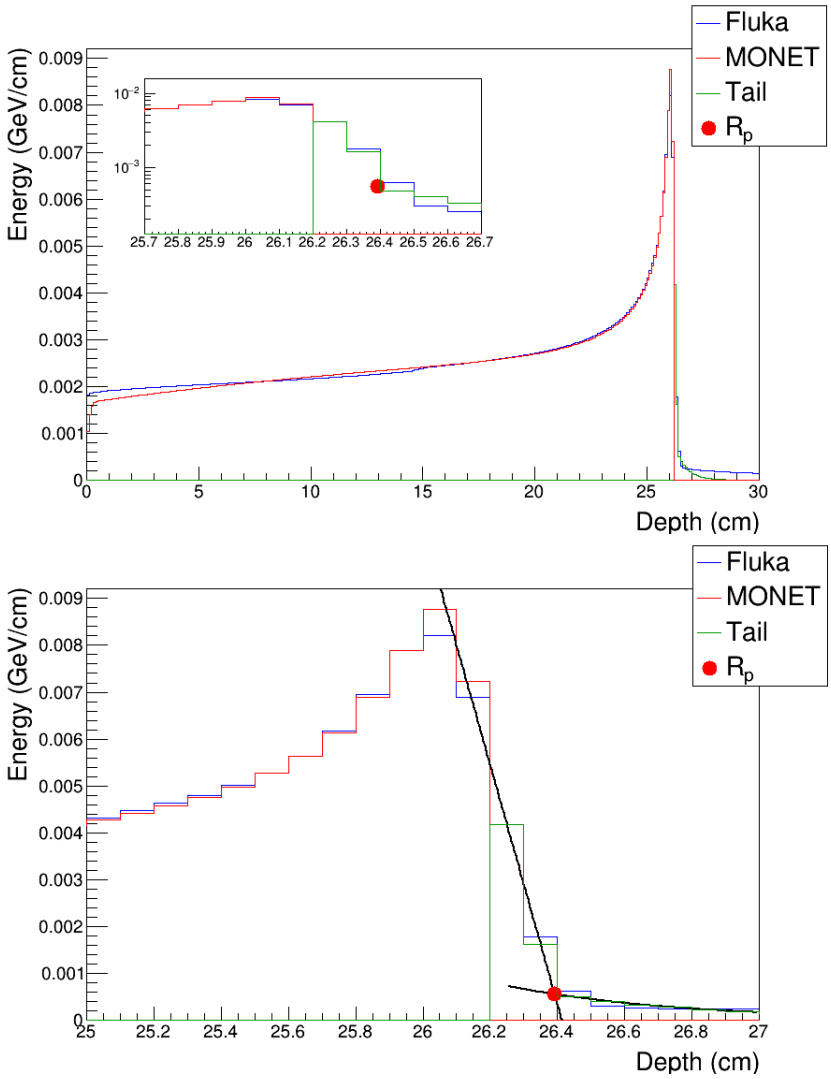

Figure 3.13: Top: Bragg curves including nuclear contributions of ^4He ions calculated with MONETα compared with FLUKA simulations for 200 MeV/u. The bullet represent the practical range R_p. In the inset plot, a zoom of fragmentation tail is reported in logarithmic scale. Bottom: the practical range as the intersection between tangent at inflection point and the exponential tail is reported.

where the values of the coefficients a_i' and b_i' are reported in the plots. These parameters allow the calculation of the depth-dose distribution of ^4He ions in water for therapeutic energies.

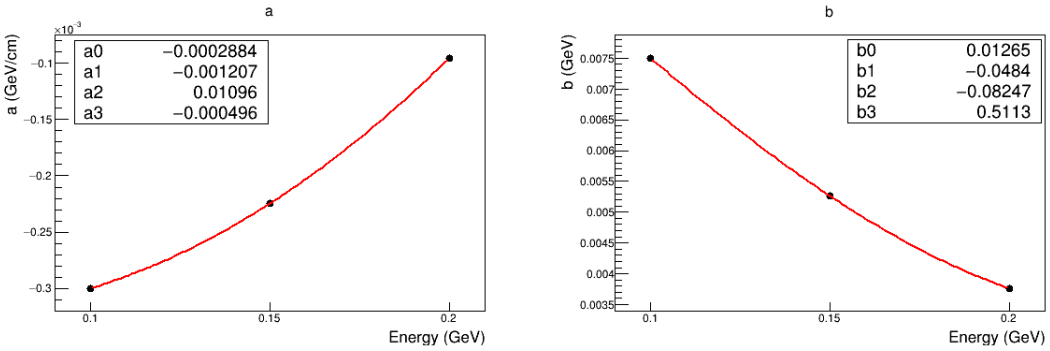

Figure 3.14: Plot of the a' and b' parameters for the longitudinal nuclear contributions (Eq.3.10) for $E = 100, 150, 200$ MeV/u.

3.5 The 3D dose distribution

After the calculation of energy deposition in the longitudinal way, the 2D lateral distribution is scaled at this value. In this way, MONET is able to evaluate a 3D dose distribution, considering all the physical interactions.
Concerning the electromagnetic part, the model is completely analytical and is based on well known and validated theories. The advantage of the MONET approach is that, due to the exact description of the electromagnetic contribution, only few parameters are required to describe the nuclear component of the dose profile. The nuclear interactions are parameterized using functions with few parameters, obtained by a fit to the Monte Carlo simulation.
The parameters of the model are reported in table 3.3.

	MONET	MONETα
Lateral	A(E,z), b(E,z)	A(E,z), b(E,z)
Longitudinal	a'(E), b'(E)	a'(E), b'(E)
Fragmentation tail		m(E), q(E) p_0(E), p_1(E)

Table 3.3: The parameters of MONET code.

In the lateral distribution, the parameters are two of Cauchy-Lorentz function, evaluated at each depth and energy. On the contrary, the two parameters for the longitudinal profile depend only for the energy of the beam and are evaluated only once. The behavior of the longitudinal parameters is given by a simple polynomial function (Eqs.3.13-3.14) as shown in Figs.3.8-3.14. For Helium ions, the parametrization of the fragmentation tail is added to consider the dose after the Bragg peak.

3.6 Conclusions

This chapter has presented the model for the longitudinal profile for protons and Helium ions, including the contribution of the average energy loss, the straggling, the nuclear interaction and the fragmentation tail.
The average energy loss is evaluated using a new formula valid both for proton and Helium beams, in agreement with the formulas already published. The straggling effects are based on the convolution of energy loss with a Gaussian distribution. The nuclear interactions are included using a linear parametrization and the study of the fragmentation tail are performed for ^4He ions, using the FLUKA results.
The comparison with FLUKA for three different energies shows a good agreement within 1% between MONET and MC evaluation. We can conclude that MONET is able to reproduce the energy-depth distribution of protons and ^4He beams in water.

Chapter 4

Results for Protons

The purpose of this chapter is to show the results obtained with the MONET code for the evaluation of energy deposition of proton beam in a water phantom. I have evaluated the energy deposition considering energies of clinical interest (100, 150 and 200 MeV).
At first, the evaluation of energy deposition for single Gaussian beam will be compared with FLUKA simulation for different energies and depths. Subsequently, the study of dose deposition in a lateral scan will be presented in order to simulate a more realist case: the field size factor test will be considered.
FLUKA simulations have been used as reference: it is currently employed in many hadrontherapy centers and has been recently validated with experimental data [79].

4.1 Simulation setup

The simulations are performed with FLUKA [110] [111] (version FLUKA2011.2c.4).
In the FLUKA simulation, the **geometry** is a parallelepiped of water contained in an air one. The implemented geometry bodies are:

- water phantom: -15<x<15 cm, -15<y<15 cm and 0<z<30 cm;
- air parallelepiped: -30<x<30 cm, -30<y<30 cm and -100<z<30 cm.

The **source** is a monoenergetic beam of energy 100, 150 and 200 MeV with an initial Gaussian profile of FWHM reported in Table 4.1.
The beam origin position is in air in particular at (0,0,-70 cm), like in the

E(MeV)	100	150	200
FWHM(cm)	1.30	0.94	0.77

Table 4.1: The FWHM of initial Gaussian profile.

CNAO facility.
The **materials** used are the default materials implemented in FLUKA. For the water phantom, I have defined the mean ionization potential as 77 eV using the MAT-PROP card. This value has been suggested by the HIT and CNAO groups, where the simulation with this mean ionization potential is validated with experimental data.
The **physics** default used is the recommended settings for hadrontherapy (defaults: HADROTHE), that takes into account:

- particle transport, by setting threshold at 100 KeV for all particles (for neutron 10^{-5} eV);
- low energy neutron transport to thermal energies;
- fully absorption for low energy;
- electromagnetic interactions;
- multiple scattering by setting threshold at minimum allowed energy;
- inelastic form factor corrections to Compton scattering and Compton profiles;
- delta ray production (threshold at 100 keV).

The **scored quantity** is the energy deposited in a mesh defined as cartesian grid of 1 mm size (x: 80 bin [-4,4] cm, y: 80 bin [-4,4] cm, z: 77-158-259 bin [0,7.7-15.8-25.9] cm for 100,150 and 200 MeV respectively).
The **statistics** used involved 10^7 primaries, in 10 batches of 10^6 histories each.

4.2 Single Gaussian beam

We have analyzed three energies ($E = 100, 150$ and 200 MeV) in order to evaluate the energy deposition with the model in a three-dimensional mesh with voxels of 1 mm^3 size, identical to the one used in the FLUKA score. In this study, the beam is monoenergetic and has a Gaussian initial lateral profile with realistic FWHM (see Tab.4.1).
We have compared the MONET with FLUKA voxel by voxel: the comparison is shown for a longitudinal central cross section in figures 4.1-4.3. Looking the Fig.4.1-4.3, there is a correspondence between the model and MC simulations.

To assess the accuracy of MONET, we have compared the results of MONET obtained by selecting transverse cross section at fixed depths (see Fig.4.1-4.3) and the FLUKA distribution.
The results of the spot profile comparison are shown in figures 4.4-4.6: in each plot the FLUKA profile and model profile on the transverse plane at different depths are shown (top left and right respectively), the relative error (bottom

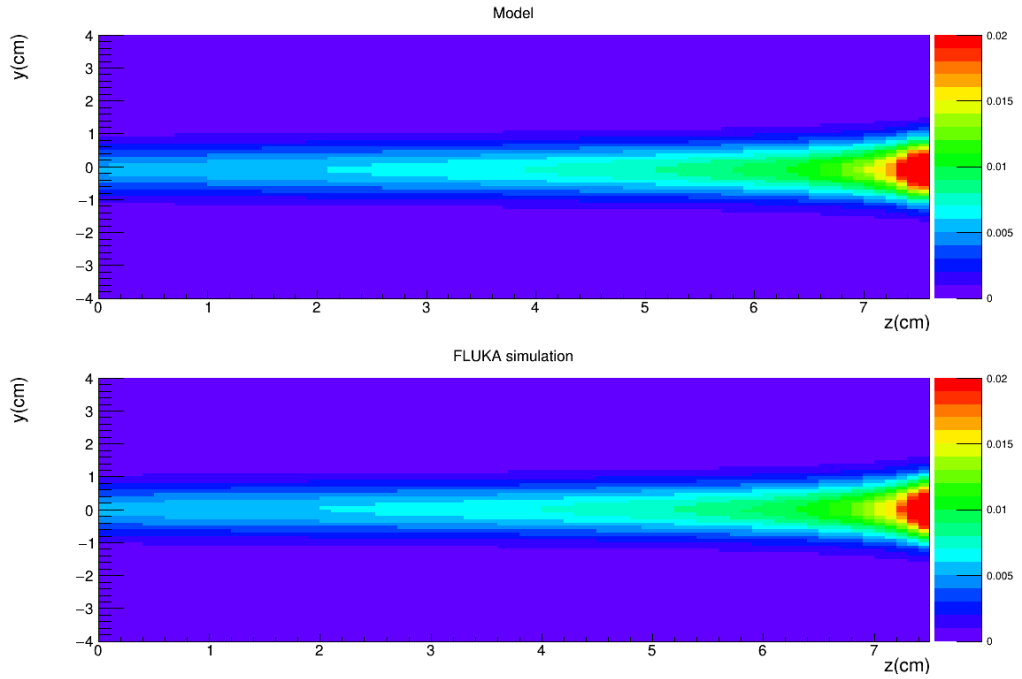

Figure 4.1: Energy deposition of proton beam of 100 MeV in water.

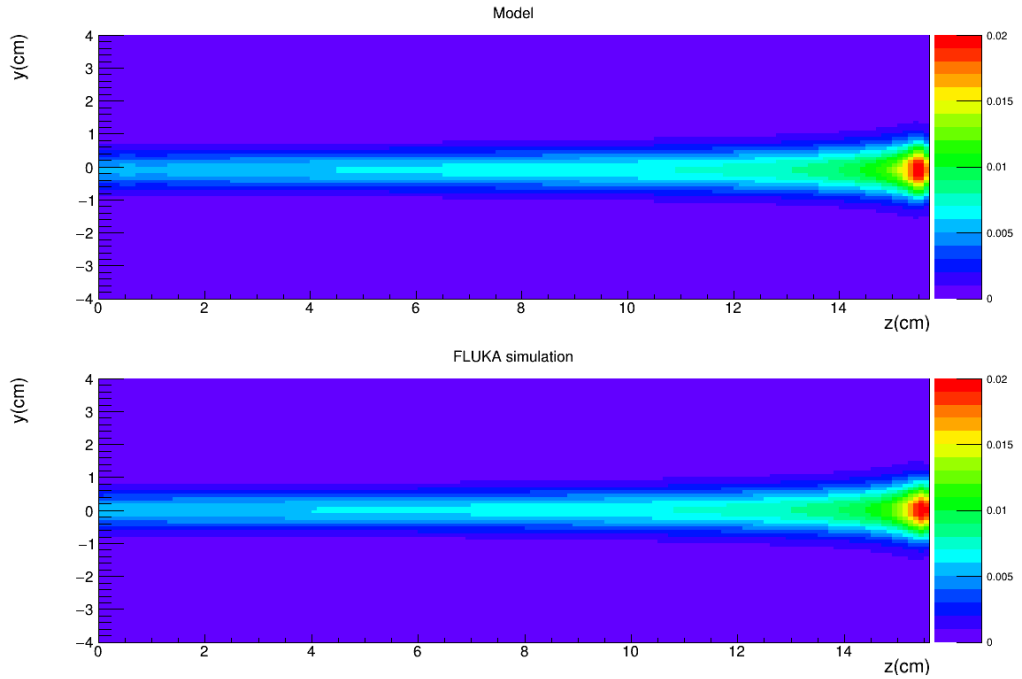

Figure 4.2: Energy deposition of proton beam of 150 MeV in water.

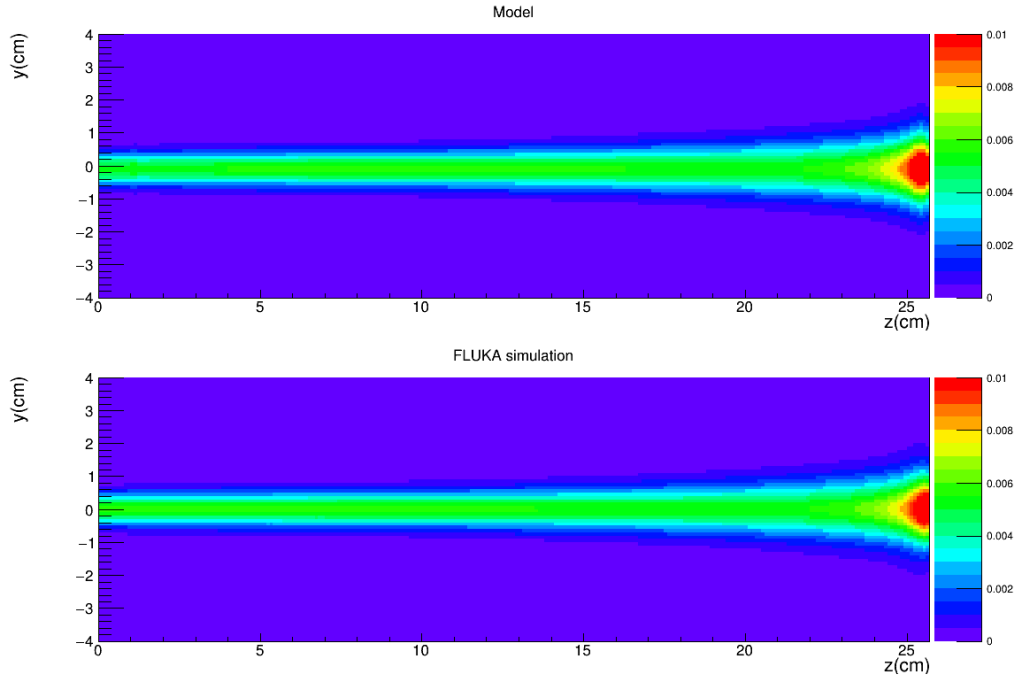

Figure 4.3: Energy deposition of proton beam of 200 MeV in water.

left) and the quantile-quantile (QQ) plot (bottom right) are plotted.

The relative errors are evaluated on the central axis and are given by:

$$e = (F - M)/F \tag{4.1}$$

where F and M are the energy deposition evaluated with FLUKA simulation and MONET respectively. The relative error represent a good indicator of the agreement between the MONET evaluation and the MC simulations. In the plot 4.4-4.6 (bottom left), the relative errors for each bin are reported: these values are between 1% and 10%.

The quantile-quantile QQ plot is useful to compare the quantiles of the model and MC distributions. This plot allows to assess the disagreement between the MC and the model: in our case the agreement is well verified since the QQ plot does not show a significant deviation from the ideal case of a 45° line [120].

For proton of 100 MeV, the results at 4 and 7 cm show a good correspondence between model and FLUKA as indicate by the QQ plot and the relative error is about 3-4%.

In case of energy of 150 MeV, the agreement between MONET and MC calculation at 10 and 15 cm is well verified by looking the results of the relative error (about 2%) and the QQ plot.

The plots for the highest energy analyzed (200 MeV) show also a good results for depth of 15 cm, but at 24 cm the relative error increases.

The maximum relative error for a single bin in the worst case is lower than

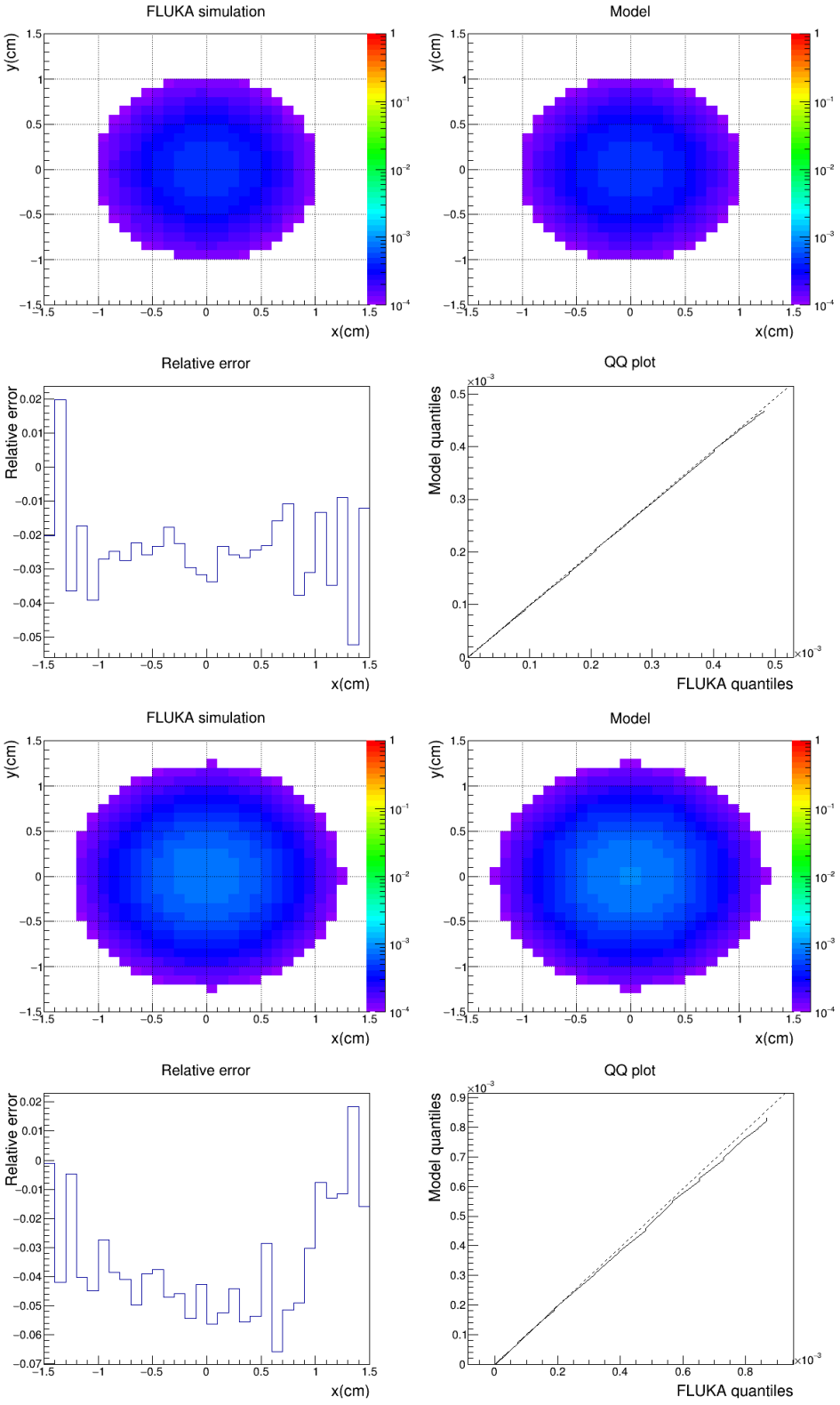

Figure 4.4: Energy deposition of proton beam of 100 MeV at 4 (top) and 7 (bottom) cm in water.

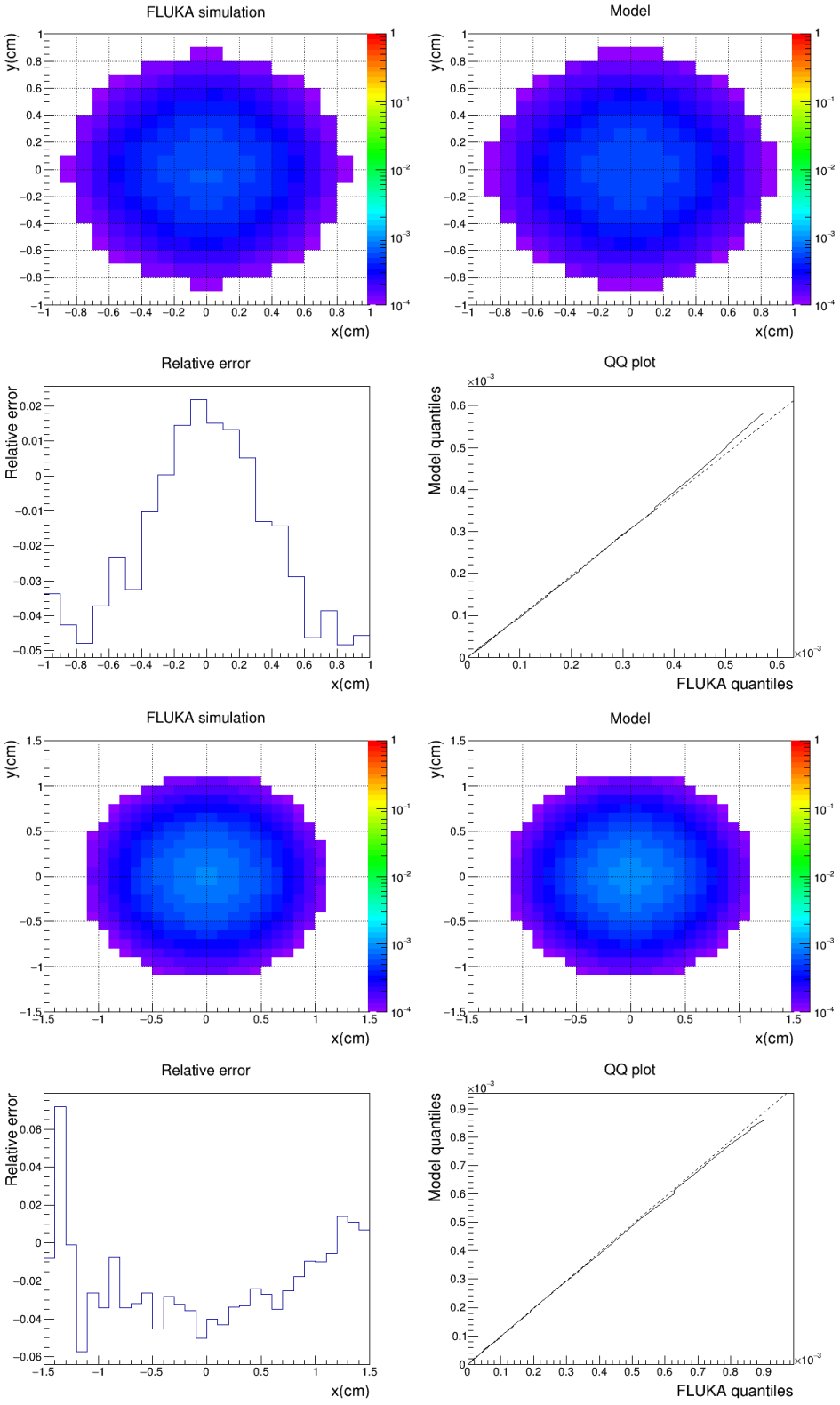

Figure 4.5: Energy deposition of proton beam of 150 MeV at 10 (top) and 15 (bottom) cm in water.

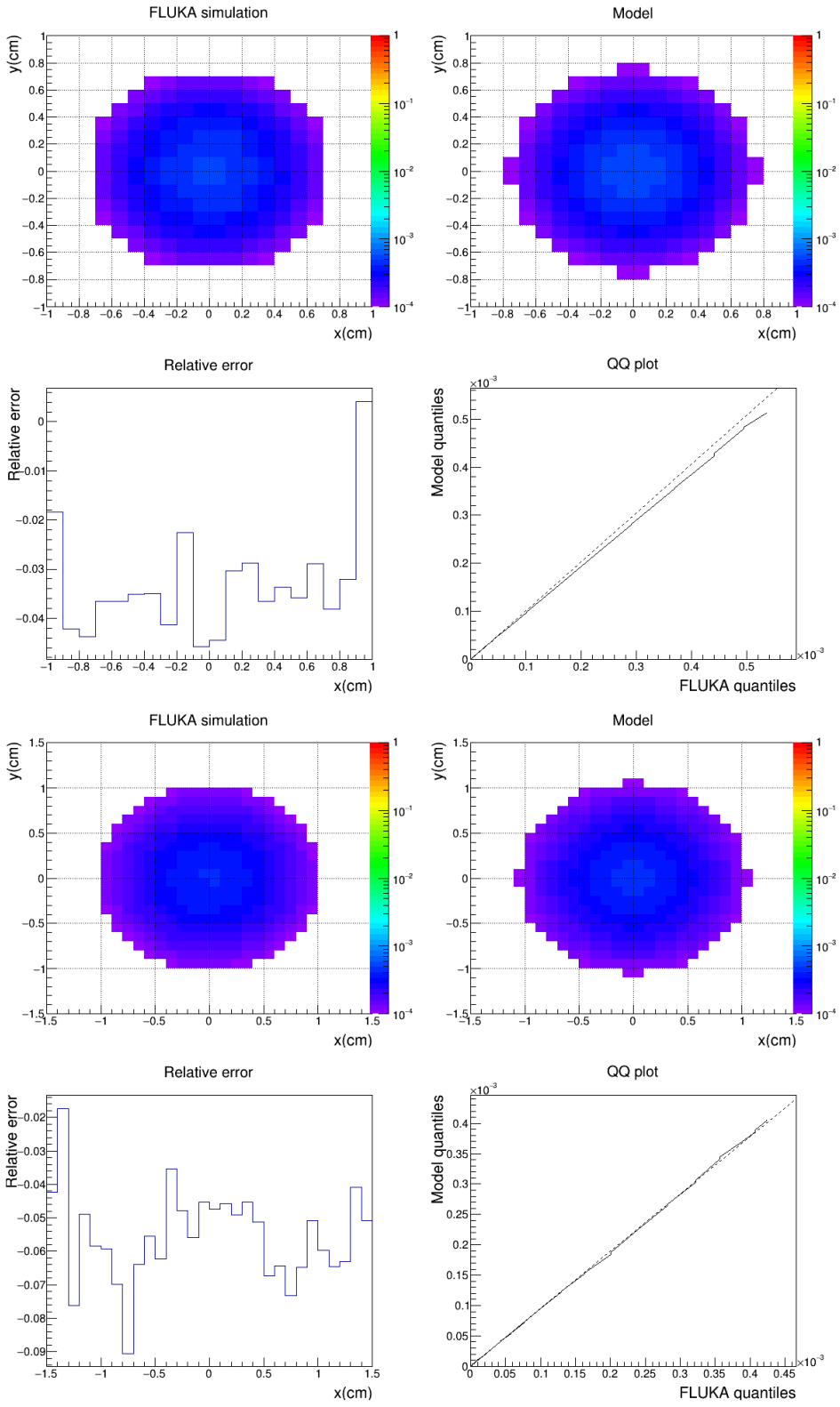

Figure 4.6: Energy deposition of proton beam of 200 MeV at 15 (top) and 24 (bottom) cm in water.

10%, showing the good correspondence between the model and the MC simulations, taking into account the expected dose delivery uncertainties (see Table 13.1 in [3] for a comparison among the major contributions).
To better quantify the compatibility of the two distributions we have performed a Kolmogorov-Smirnov (KS) test [121]: we have used the maximum distance D as a criterion to evaluate its accuracy. The use of the maximum distance of KS test is complementary to the use of the standard p-value and, in case of binned data, is a parameter without a universal statistical meaning, that allows to estimate the different fits quality in a relative manner.
The maximum value of D is about 5×10^{-3} indicating a very good agreement. In all analyzed cases, the results of MONET is in good agreement with the FLUKA simulation, indicating a good accuracy of the energy deposition formulas implemented in the code.

4.3 Lateral scan: Field Size Factor test

In order to estimate the accuracy of the MONET code, focusing on the tails of the distribution that produce the low-dose contribution, we have performed a Field Size Factor (FSF) test. For the FSF test, the model and FLUKA code evaluates the energy deposition of different beams stacked together in a lateral scan. In the lateral scan, the code calculates the energy deposition for a single beam. Afterwards the dose profile is translated in order to obtain a lateral scan and the total energy deposition will be given by a sum of all the single beams. For the FLUKA simulation, the lateral scan is achieved by modifying the source routine in agreement with the model scan.
The field size factor [122] is the ratio between the total dose deposition in a concentric square fields of increasing size f and the same quantity in a square reference ($f_R = 10$):

$$FSF(f) = \frac{D_f}{D_{10}} \tag{4.2}$$

where f can assume different values (in particular $f = 4, 6, 8, 10, 12$ cm). We have considered the field size factor for our model and simulations.
The FSF variations as a function of square size f are shown in Fig. 4.7 for different energies and depths.

For 100 MeV, the trend is similar at 4 and 6 cm in water: the agreement between MONET and FLUKA is very good for field higher than four and the differences at low field ($f = 4$ cm) is about 5%.
For 150 MeV, the difference between the model and MC calculation is less than 1% at 10 cm and increases at 15 cm in water.
A similar results are obtained for 200 MeV, where the agreement is about 1% and increases for depths near to the Bragg Peak.
In all the studied cases, the agreement between MONET and FLUKA improves with increasing depth: these results indicate a good description of the energy deposition in correspondence of the Bragg peak.

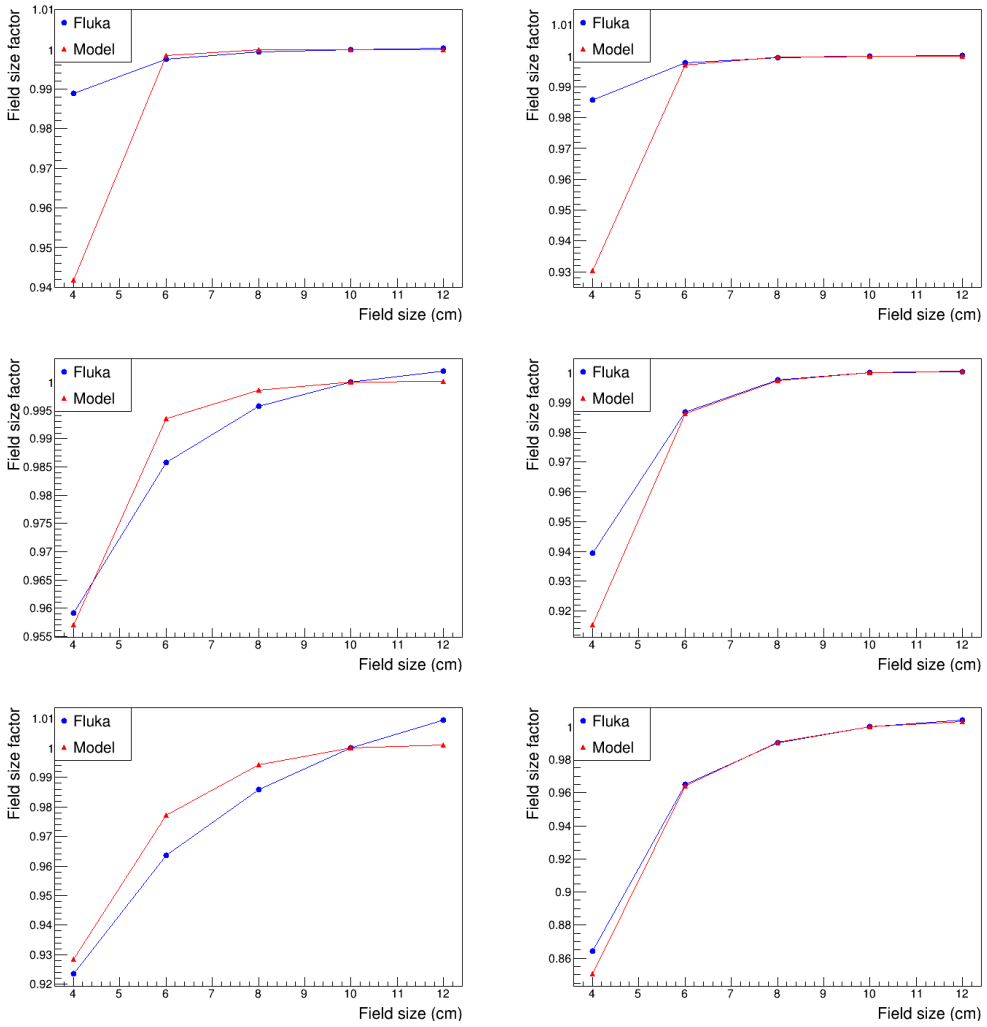

Figure 4.7: FSF for the model and FLUKA.
Top: Energy 100 MeV at z=4 cm (right) and z=6 (left).
Middle: Energy 150 MeV at z=10 cm (right) and z=15 (left).
Bottom: Energy 200 MeV at z=15 cm (right) and z=25 (left).
A straight line connection between points is added to improve visualization.

Looking at Figure 4.7, we can observe an increase of the fluctuations at low energy (100 MeV) compared to high one, in agreement with [123]. The fluctuation are due to the larger FWHM of the low energy beam, that dominates on the nuclear interaction [122].
We have also noted bigger differences at low energy when the field size is comparable with the dimension of the lateral scan (source size is 3 cm) as shown in Fig. 4.7.
The difference between model and MC simulation for FSF evaluated at three depths for each energy are reported in Table 4.2. The maximum difference is

about 5%, the same order of accuracy of the single beam case.
In conclusion, the FSF tests show a good agreement between MONET and FLUKA and these results also indicate a good evaluation of the low dose contributions.

E(MeV)	100			150			200		
FSF	2	4	6	5	10	15	10	15	25
4	-5.1%	-4.8%	-5.6%	-0.2%	-0.2%	-0.3%	1.4%	0.5%	-1.6%
6	0.0%	0.1%	-0.1%	0.7%	0.8%	-0.1%	1.8%	1.4%	-0.1%
8	0.0%	0.0%	0.0%	0.3%	0.3%	-0.0%	1.0%	0.8%	0.1%
12	-0.0%	-0.0%	-0.0%	-0.1%	-0.2%	0.0%	-0.8%	-0.8%	-0.1%

Table 4.2: FSF differences between the model and FLUKA for four fields, three depths and three energies.

4.4 Conclusions

In this chapter, I have demonstrated the possibility to calculate a complete 3-dimensional energy profile for protons in water in an accurate and fast way. The dose deposition for different energies has been analyzed comparing the 2-dimensional lateral distribution obtained with the MONET using FLUKA code as reference.
Starting with the case of single beam, I have found an agreement better than 10% considering the simple relative error and we obtained a maximum distance with the KS test of 5×10^{-3}. Also the QQ plot indicates a good compatibility between model and simulations. For the lateral scan, the maximum difference is about 5%, a similar results to other studies.
The comparison with the results of the FLUKA code shows a very good agreement in all the considered case, with a general trend of improvement with increasing energies.

Based on these results, one can conclude that MONET is an accurate tool for the evaluation of the energy deposition for proton beam. The MONET code accounts for all the physical effects of the interaction of protons with water and is based on well known and validated theories. The longitudinal and the lateral e.m. contribution can be used for any hadronic projectile and target, since they are independent from the beam size. Therefore, the advantage of MONET approach is that, due to the exact physical description of the electromagnetic contribution and to the calculation of the radial distribution from two non Gaussian projections, only few parameters are required to describe the nuclear component of the dose profile. This can be done easily before the clinical application of the model to prepare the parameters database.

Chapter 5

Results for ^4He ions

In this chapter, the results obtained with the extension of MONET code to the case of ^4He beams, called MONETα, are presented. I have evaluated the energy deposition considering energies of clinical interest (100, 150 and 200 MeV/u) in a water phantom.
At first, the evaluation of the energy deposition for a single Gaussian beam is compared with a FLUKA simulation for different energies and depths. Subsequently, the calculation of the dose deposition in a lateral scan is shown in order to simulate a clinical case. To this aim, the field size factor test is performed.
The FLUKA simulations have been used as reference. This is supported by the fact that FLUKA has been validated with experimental data of ^4He ions, acquired at the HIT center [77] [118].

5.1 Simulation setup

The simulations are performed with FLUKA [110] [111] using the development version (version 2017.0). The choice of using the FLUKA development is justified by their recent validation with experimental data from the HIT center [77] [118].
In the simulation, the **geometry** is a parallelepiped of water contained in an air one. The implemented geometry are:

- water phantom: -15<x<15 cm, -15<y<15 cm and 0<z<30 cm;
- air parallelepiped: -30<x<30 cm, -30<y<30 cm and -1.1<z<30 cm.

The **source** is a monoenergetic beam of energy 100, 150 and 200 MeV/u with an initial Gaussian profile of FWHM of 0.7 cm. The beam position is in air at (0,0,-1 cm).
The **materials** used in the simulation are the default materials implemented in FLUKA. I have defined the mean ionization potential of water using the

MAT-PROP card as the same value of the proton beam ($I_p = 77eV$).
The **physics** default used is the recommended settings for particle therapy (defaults: HADROTHE). The physics details of HADROTHE setting are reported in 4.1.
The **scored quantity** is the energy deposited in a mesh defined as cartesian grid of 1 mm size (in particular x: 80 bin [-4,4] cm, y: 80 bin [-4,4] cm, z: 78-159-261 bin [0,7.8-15.9-26.1] cm for 100,150 and 200 MeV/u respectively).
The **statistics** used involved 10^7 primaries, in 10 batches of 10^6 histories each.

5.2 Single Gaussian beam

We have analyzed three energies ($E = 100, 150$ and 200 MeV/u) in order to evaluate the energy deposition with MONETα in a three-dimensional mesh with voxels of 1 mm^3 size, identical to the FLUKA one. In this case, the beam is monoenergetic and has a Gaussian initial lateral profile with realistic FWHM of 0.7 cm.
We have compared MONETα with FLUKA voxel by voxel: the comparison is shown for a longitudinal central cross section in figures 5.1-5.3. Looking the results, there is a good agreement between the model and MC simulations.

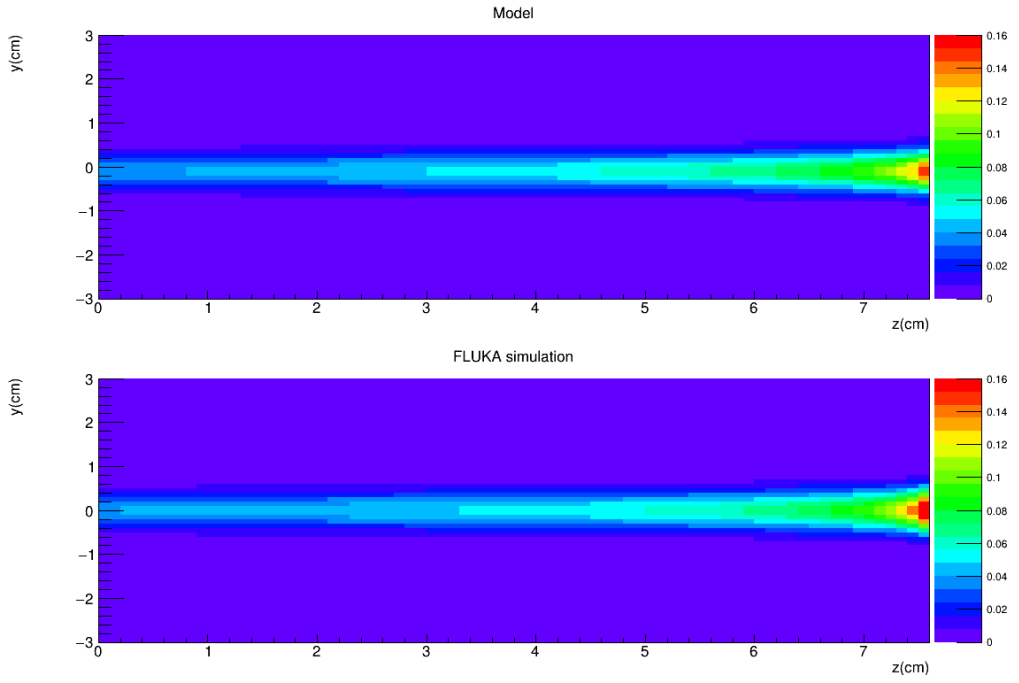

Figure 5.1: Energy deposition of ^4He beam of 100 MeV in a water phantom obtained with FLUKA simulation and MONETα.

To better compare MONETα and FLUKA simulation, the results are obtained by selecting transverse cross section at fixed depths (see Fig.5.1-5.3).

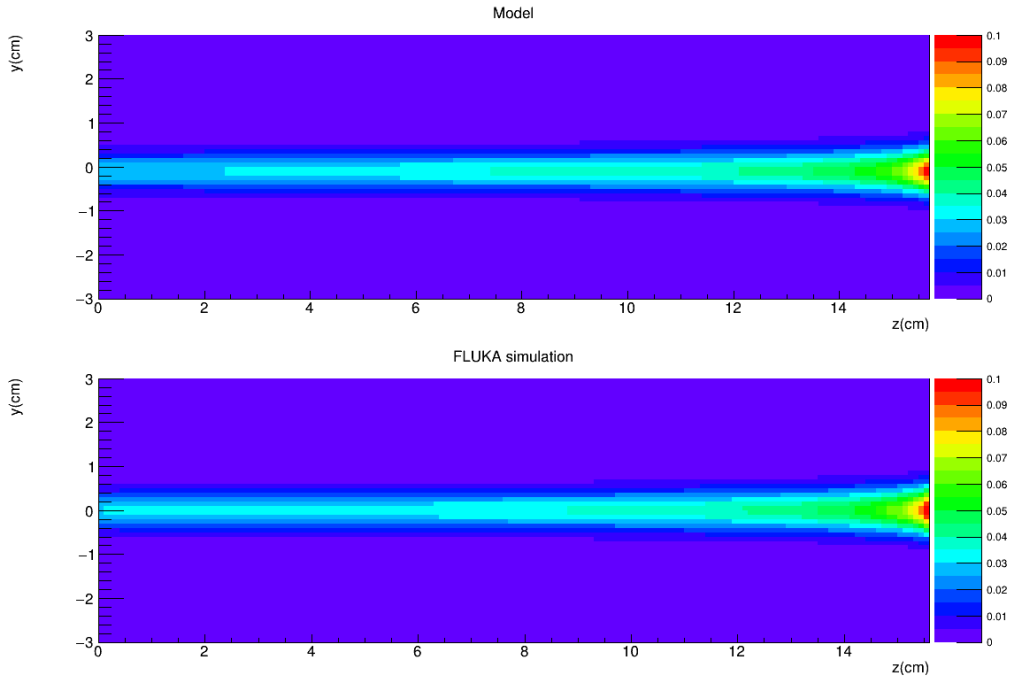

Figure 5.2: Energy deposition of ^4He beam of 150 MeV in a water phantom obtained with FLUKA simulation and MONETα.

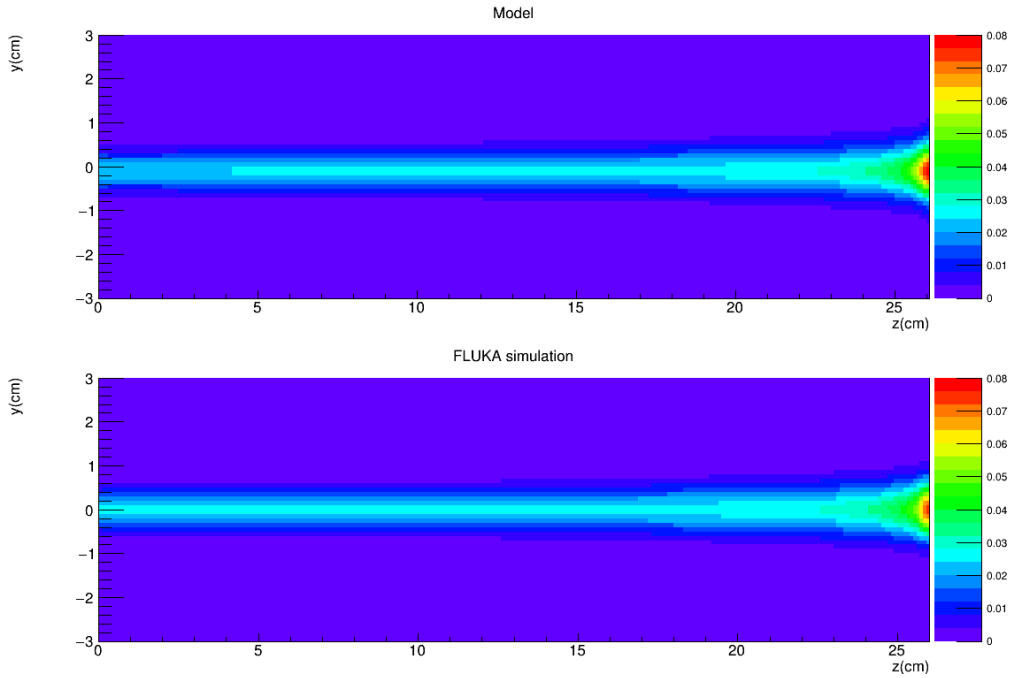

Figure 5.3: Energy deposition of ^4He beam of 200 MeV/u in a water phantom obtained with FLUKA simulation and MONETα.

These results are shown in figures 5.4-5.6: the FLUKA and the MONETα profile on the transverse plane at different depths are shown (top left and right respectively) and the relative error (bottom left) and the quantile-quantile (QQ) plot (bottom right) are consider as an estimation of the accuracy of the model.
The relative errors are calculated on the central axis. The QQ plot [120] is used to compare the quantiles of the model and MC distributions. In the analyzed case the agreement is well verified, since the plot does not show a significant deviation from the ideal 45° line.
For ^4He of energy 100 MeV/u, the results at 4 and 7 cm shown a correspondence between model and FLUKA: the relative error is less than 10% and the QQ plot is well verified.
In case of energy 150 MeV/u, the agreement between MONET and MC calculation at 10 and 15 cm improves. The relative error is about 5% and the QQ plot shows good correspondence.
Also for 200 MeV/u, we have a good results for depth of 15 cm with a relative error less than 5%, but the relative error increases at 25 cm (6-8%), as reported also by the QQ plot.
The maximum relative error is about 10%, showing a correspondence between the model and the MC calculation. The QQ plots indicates a similar results of relative errors: the agreement is satisfactory considering the dose and range uncertainties.
To quantify the compatibility of the two distributions I have also performed a Kolmogorov-Smirnov (KS) test using the maximum distance D as a criterion to evaluate its accuracy. The maximum distance of KS test is a parameter, that allows to estimate the different fits quality in a relative manner.
For the distribution reported in Figures 5.4-5.6, the maximum value of D is about 6×10^{-3} indicating a good agreement.

In conclusion, MONETα is in good agreement with the FLUKA simulation in all analyzed energies. These results indicate the possible extension of the MONET code in case of ^4He with a good accuracy.

5.3 Lateral scan: Field Size Factor test

I have also analyzed the energy deposition in a lateral scan in order to estimate the accuracy of the MONETα code in the description of the tails of the distribution, that produce the low dose contribution. To this aim, I have performed a Field Size Factor (FSF) test and the values obtained for the model and the simulation are compared.
The model and the FLUKA code evaluate the energy deposition of different beams stacked together in a lateral scan. For the simulation, the scan is achieved by modifying the source routine according to the model. The MONETα code calculates the energy deposition for a single beam, after the

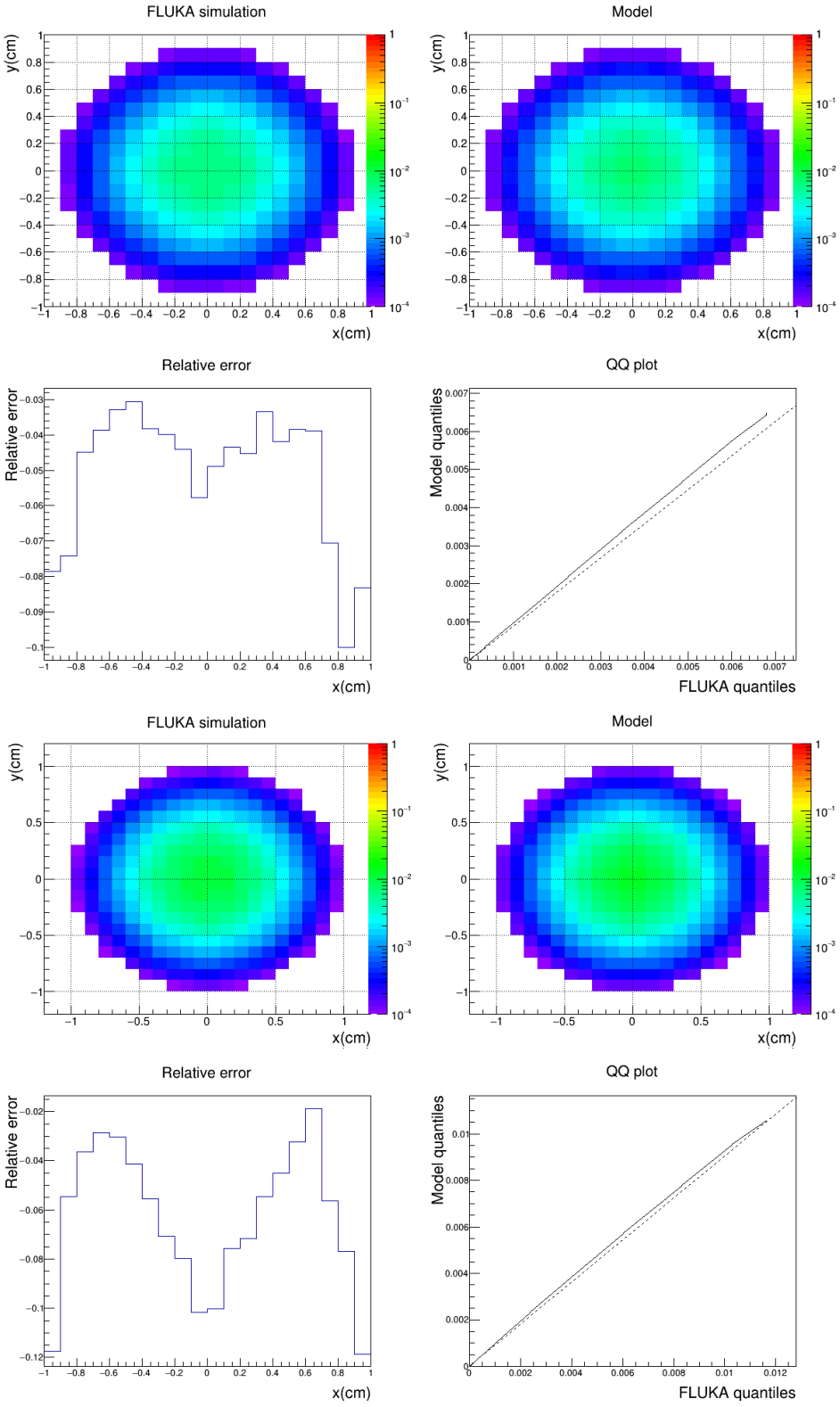

Figure 5.4: The energy deposition of ^4He beam of 100 MeV/u at 4 (top) and 7 (bottom) cm in water phantom.

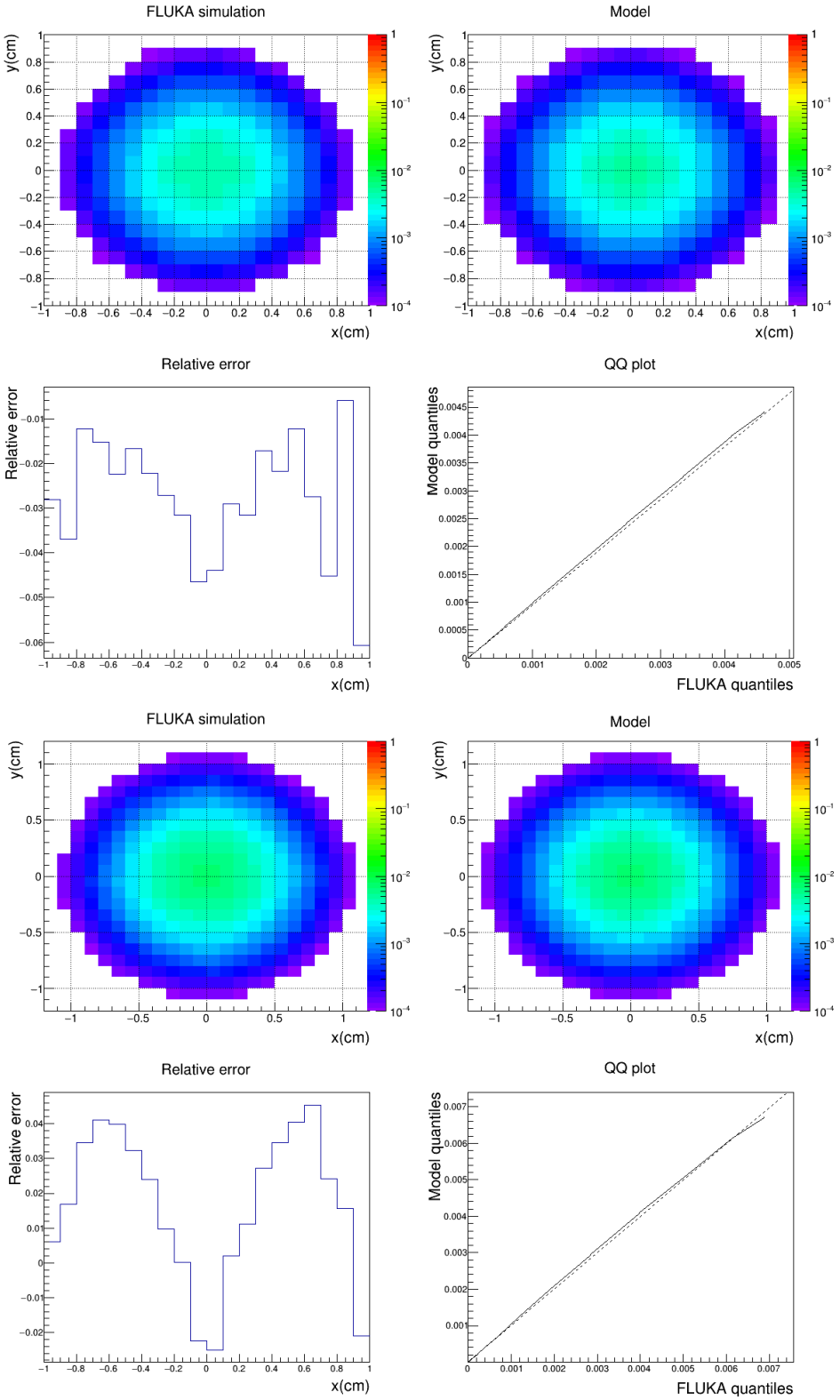

Figure 5.5: The energy deposition of ^4He beam of 150 MeV/u at 10 (top) and 15 (bottom) cm in water phantom.

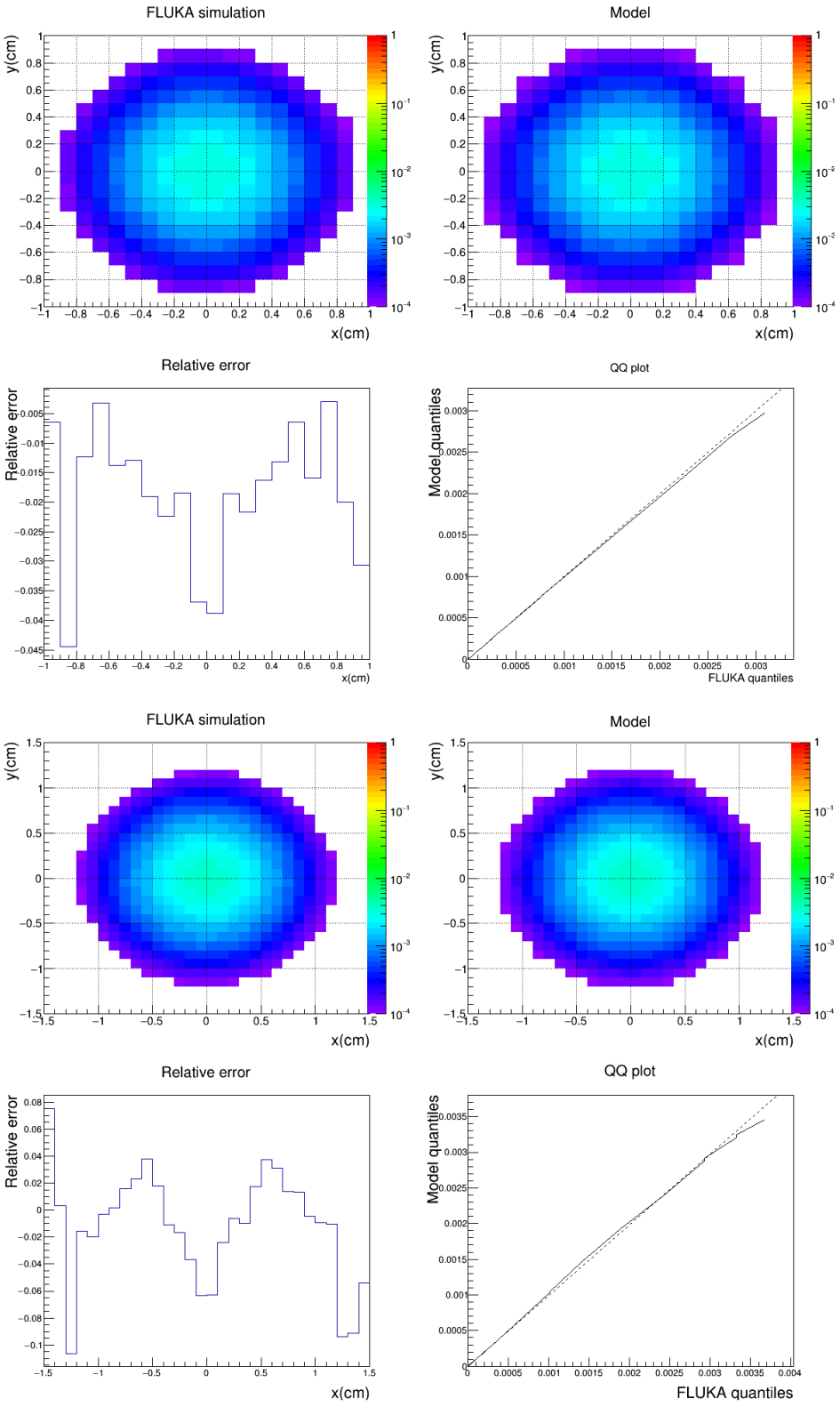

Figure 5.6: The energy deposition of ^4He beam of 200 MeV/u at 15 (top) and 25 (bottom) cm in water phantom.

energy profile is translated in order to obtain a lateral scan and the total distribution is given by a sum of all contribution.
The field size factor [122] is evaluated using Eq. 4.2, considering the ratio between the energy deposition in different square field ($f = 4, 6, 8, 10, 12$ cm) and the same quantity in the square reference ($f_R = 10$).

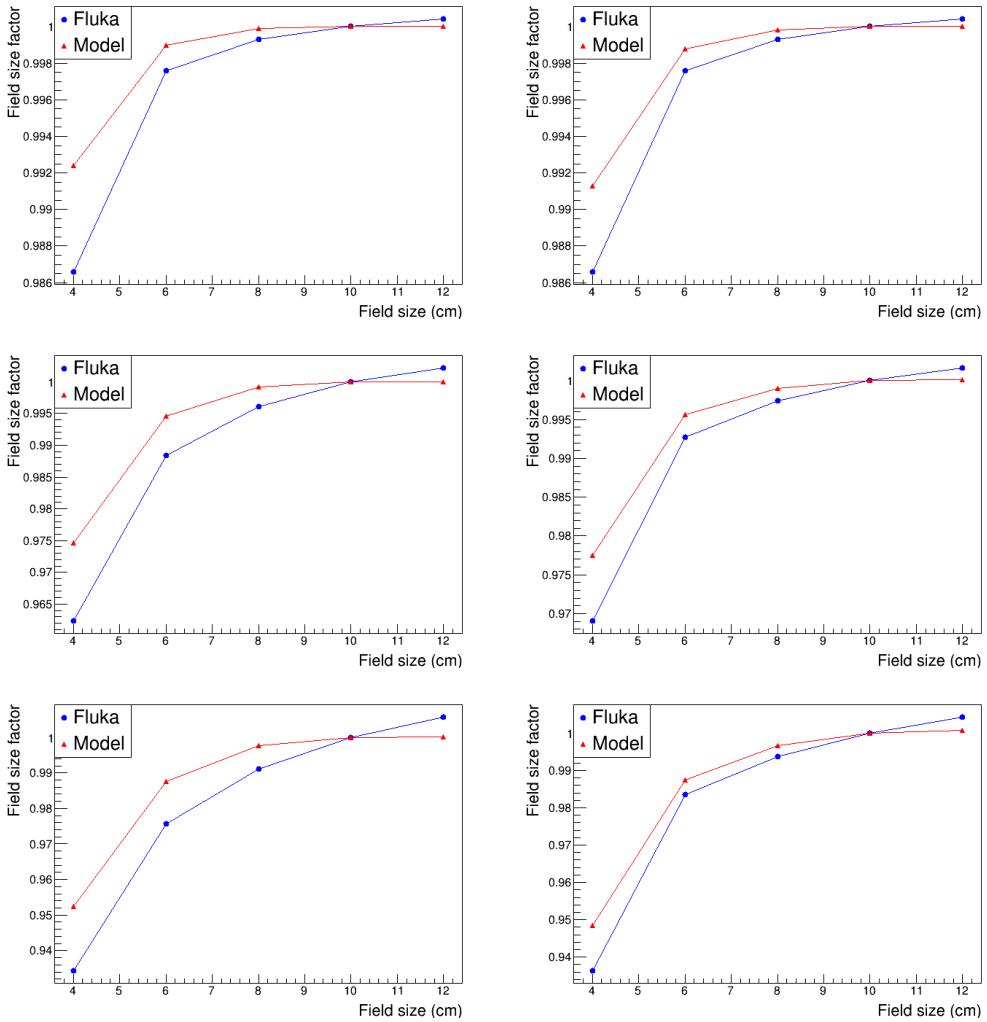

Figure 5.7: FSF for the model and FLUKA.
Top: Energy 100 MeV/u at z=4 cm (right) and z=6 (left).
Middle: Energy 150 MeV/u at z=10 cm (right) and z=15 (left).
Bottom: Energy 200 MeV/u at z=15 cm (right) and z=25 (left).
A linear interpolation of the points is added to improve visualization.

In Fig. 5.7, the FSF variations as a function of square size f are shown for different energies and depths.
For ^4He of 100 MeV/u, the trend is similar at 4 and 6 cm in water: the agree-

ment between MONETα and FLUKA is very good and the differences is less than 0.6%.
For 150 MeV/u, the agreement between the model and MC calculation is good: it is less than 1.2% at 10 cm and increases at 15 cm in water (0.9%).
Similar results are obtained for 200 MeV, where the agreement increases for depths near to the Bragg Peak (z=25 cm).
In general, the agreement between MONETα and FLUKA simulation improves with increasing depth: these results indicate a good description of the energy deposition in correspondence of the Bragg peak.

E(MeV)	100/u			150/u			200/u		
FSF	2	4	6	5	10	15	10	15	25
4	0.4%	0.6%	0.5%	0.9%	1.2%	0.9%	1.8%	1.9%	1.3%
6	0.1%	0.1%	0.1%	0.3%	0.6%	0.3%	1.1%	1.2%	0.4%
8	0.0%	0.1%	0.0%	0.1%	0.3%	0.2%	0.6%	0.7%	0.3%
12	0.0%	-0.0%	-0.0%	-0.1%	-0.2%	-0.2%	-0.4%	-0.6%	-0.3%

Table 5.1: FSF differences between the model and FLUKA for four fields, three depths and three energies.

In Table 5.1 reports the difference between MONETα and FLUKA simulation for FSF evaluated at three depths for each energy. The maximum difference is less than 2%, showing a good agreement between the model and simulations.
In conclusion, the FSF tests show a good evaluation of the low dose contributions with MONETα code.

5.4 Calculation time

In addition to the accuracy, another advantage of MONET approach is the fast calculation time.
For the timing evaluation I used a DELL XPS computer with an INTEL i7 (8 cores), with 3.6 GHz CPU, 16 Gbyte RAM and a 64 bit. The times are estimated by calculating the the energy deposition for a single Gaussian beam and for the full lateral scan for proton and Helium ions.
On average, for each depth the calculation time $\sim$ 2 seconds for the single beam and $\sim$ 4 seconds for the full lateral scan. The MONET calculation times are faster than typical simulation times ($\sim 1 - 10$ hours for 10^7 primaries).
Therefore MONET code can be competitive, in calculation accuracy and speed, with existing solutions.

5.5 Conclusions

In this chapter, I have investigated the possibility to describe the energy deposition for ^4He beams with the MONET approach, already validated for proton beams.
The dose deposition for different therapeutic energies has been analyzed, comparing the distributions obtained with the model using the FLUKA code.
In the case of single Gaussian beams, I have found a good agreement as indicated by the relative errors and the QQ plots. For the lateral scan, the maximum difference is less than 2%, a result similar to the study for proton beam. These results show a good evaluation of the energy deposition in all the considered cases. The number of free parameters is the same as in the proton case.

The results obtained demonstrate the possibility to extend the MONET code to the case of ^4He ions, making MONETα a possible new tool for the evaluation of the energy deposition for applications to Treatment Planning Systems (TPS).

Conclusions and future perspectives

In this thesis, the energy deposition of proton and Helium ion beams in a water target was investigated with the development of a new model. For the lateral profile, the MONET (MOdel of ioN dosE for Therapy) code is based on the Molière theory of multiple Coulomb scattering, with the nuclear interactions added using a parametrization obtained by a fit of FLUKA simulation. The passage from the projected to a two-dimensional (2D) lateral distribution is performed with an algorithm that allows to reconstruct the radial distribution. For the longitudinal profile, MONET uses a new formula for evaluation of the average energy loss and the convolution with a Gaussian distribution for the straggling effect, while the nuclear contributions are included using a linear parametrization.
The results of the model for protons and Helium ions are compared to FLUKA simulations, considering both a simple initial Gaussian profile and a more complex lateral scan. Looking at the results, one can conclude that MONET is an accurate model for the evaluation of the energy deposition for proton and Helium ions in water.
The MONET code accounts for all the physical effects of the interaction of protons and Helium ions with water and is based on well known and validated theories. The advantage of our approach is that only four parameters are required to describe the nuclear component of the dose profile. Two parameters are for the lateral distribution (Cauchy-Lorentz function) and are evaluated by a fit at each depth and energy, while the two parameters for the linear parametrization of the longitudinal profile depend only on the energy of the beam and are evaluated only once.
Another advantage is the fast calculation time. Indicatively, for each depth the calculation time for the full 3D dose is ~ 2 seconds for the single beam and ~ 4 seconds for the full lateral scan. These times extrapolated to a full dose calculation are competitive with typical simulation times ($\sim 1 - 10$ hours).
The electromagnetic contribution can be easily extended for any hadronic projectile and target, as demonstrated in Appendix A. For the nuclear part,

the approach developed in the thesis is open to different developments: the parametrization of the nuclear interaction in different materials of clinical interest, the implementation of algorithms to account for inhomogeneities and the real materials composition of the patient and the creation of a database for the parameter of the nuclear interactions.
The MONET code can also be implemented for other particles, e.g. Carbon or Oxygen ions: Carbon beams are already clinically used in different facilities like CNAO and HIT, while Oxygen ions are a potential candidate, due to their higher relative biological effectiveness and reduced oxygen enhancement ratio. By increasing the atomic number, the effects of nuclear interactions become more relevant in the calculation of the energy deposition and for the future implementation of these ions, the nuclear interactions need to be further investigated and new experimental data are required.
Another important issue in particle therapy, only suggested in the thesis, is the theoretical evaluation of dose after the Bragg peak: a possible solution could be extending the expression for the fragmentation tails used for Helium to other ions.
Finally, a future perspective would be to implement MONET in a TPS as online/in-room fast dose evaluation tool.

Part of the studies presented in this thesis has been published in the papers in Reference [67] [69] [78] [79] [109]. A further complete article for energy deposition of Helium ions is in preparation.

Appendix A

Molière theory for compounds and layers

In Chapter 2, we have shown that Molière theory reproduces well not only angles, but also the lateral displacement in water for proton and ^4He beam at therapeutic energies and in general is in very good agreement with the predictions of the FLUKA code [110].
The Molière theory is based on two well known parameters χ_c^2 and χ_α^2 [79]. Here we generalize the formulae in the case of absorbers made by many layers of different materials [109].
We indicate with χ_W^2 the kinematic independent part of χ_c^2:

$$\chi_{Wij}^2 = \theta_0 z_0^2 \frac{n_{ij} Z_{ij}^2 \rho_i}{A_{Tj}} \tag{A.1}$$

where $\theta_0 = 0.1569 \times 10^{-6}$, z_0 is the projectile charge, the indices i, j refer to the i^{th} atom in the molecule of the j^{th} layer, ρ_j is the layer density (g/cm^3), A_{Tj} is the total atomic weight of the molecule of the layer j. For a single monoatomic layer with thickness z (cm) and no energy loss and for a particle of momentum p (GeV) and velocity β the parameter χ_c^2 is:

$$\chi_c^2 = \chi_W^2 \frac{z}{p^2\beta^2} \tag{A.2}$$

The general formula, taking into account layers, atoms of the molecules and energy loss becomes:

$$\chi_c^2 = \sum_j^{\text{layers}} \frac{1}{p_j^2\beta_j^2} \sum_i^{\text{atoms}} \chi_{Wij}^2 \, I_0(d_j, R_j, k_j) \tag{A.3}$$

where p_j and β_j are momentum and velocity of the projectile at the entrance of the layer j of thickness d_j. The integral I_0 takes into account the energy

loss with Øverås equation 2.43 and is given by:

$$I_0(d,R,k) = \int_0^d \frac{1}{(1-x/R)^k}\mathrm{d}x = R\frac{(1-d/R)^{1-k}-1}{k-1}\ , \quad k \neq 1 \tag{A.4}$$

The equation A.2 propagates in an independent way the effects of the layers through the stack and is entirely analytical, since the integral I_0 has an explicit solution.
The second Molière parameter χ_α can be extracted from the following equation:

$$\chi_c^2 \log \chi_\alpha^2 = \sum_j^{\text{layers}} \frac{1}{p_j^2\beta_j^2} \sum_i^{\text{atoms}} \chi_{Wij}^2 \int_0^{d_j} \frac{\ln[\mu_{ij}^2(z)\chi_{0ij}^2(z)] - F_{ij}(z)/Z_{ij}(z)}{(1-z/R_j)^{k_j}}\mathrm{d}z \tag{A.5}$$

where χ_c^2 on the left side comes from equation A.2. The parameter $\mu_{ij}^2(z)$ is given by:

$$\mu_{ij}^2(z) = \left(1.13 + 3.76\,\frac{z_0^2 Z_{ij}^2}{137^2\beta_j^2(z)}\right)\ , \qquad \chi_{0ij}(z) = 4.216\times10^{-6}\,\frac{Z_{ij}^{1/3}}{p_j(z)} \tag{A.6}$$

and the Fano factor is :

$$F_{ij}(z) = \ln\left(\frac{1130}{Z_{ij}^{4/3}(1/\beta_j^2(z)-1)}\right) + u_i - \frac{\beta_j^2(z)}{2} \tag{A.7}$$

where $3.6 < u_i < 5.8$ from the light to the heavier elements [105].
The momenta and velocities $p_j(z)$ and $\beta_j(z)$ in equations A.6, A.7 must be evaluated at each integration step from equation 2.43, where p_j and β_j must be evaluated at the entrance of each layer.
The smooth behavior of the integrand in equation A.5 does not create computational problems and the integration can be performed with fast numerical methods.
Starting from the two fundamental parameters of equations A.2 A.5, the b parameter, that appears in the final formula for the distribution, becomes:

$$b = \ln\frac{\chi_c^2}{\chi_\alpha^2} - 0.154432 \tag{A.8}$$

and the B parameter, connected to the r.m.s. angle, which is solution of the equation:

$$B - \ln B = b\ , \qquad B \simeq 1.153 + 1.122\,\ln\frac{\chi_c^2}{\chi_\alpha^2} \tag{A.9}$$

The square of the r.m.s. angle, coming from the Gaussian first term of the power series of the Molière projected distribution [85], is given by:

$$\left\langle\theta_x^2\right\rangle = \frac{\chi_c^2 B'}{2} \tag{A.10}$$

where $B = B'$. When the Gaussian term is used, the area of the curve makes the r.m.s. of the curve greater than that of the Molière one. For this reason often a reduced r.m.s. is used, with the choice $B' = B - 1.2$ [82] [85] [55]. The Fermi-Eyges equations (Eq.2.5-2.8) give the best agreement with this reduced r.m.s. angle [71]. In this case, the scattering length of Eq.2.4, taking into account Eq. A.2, is:

$$T(z) = \frac{d}{dz}\left(\frac{\chi_c^2\, B'}{2}\right) \tag{A.11}$$

In the Molière theory, the non-locality is contained in the $\ln(\chi_c^2/\chi_\alpha^2)$ term of the b and B parameters. The degree of dependence of the successive layers is represented by χ_c^2, which, from Eq.A.3, is proportional to the absorber thickness d_j.
To apply the Molière theory, we have to pass from the scattering angle at the absorber exit to the displacement measured on a detection plane. The spatial displacement x should be evaluated from the exit angle θ as $x = z_{\text{esp}}\theta$, where z_{esp} is the effective scattering point coordinate already defined in Eq. 2.13.
Gottschalk proposed in [55] to find the square of this distance as the sum in quadrature of the term $(D - z)^2 \langle\theta_x^2\rangle$, where z is the current depth and D the distance from the detection plane (usually placed at the end of the last layer), taking into account the energy loss and using the Highland approximation [124].
Bellinzona in [79] evaluated this distance with Eq. A.10, by summing in quadrature the χ_c^2 contribution and multiplying the expression by the final B value. This factor is dues to pass from the angle to the displacement in the Molière distribution. In the case of multiple layers this formula can be modified as:

$$z_{\text{esp}}^2 = \frac{\langle (D-z)^2\theta^2\rangle}{\langle\theta^2\rangle} = \frac{\sum_{j}^{\text{layers}} I_2(d_j, D, R_j, k_j) \sum_{i}^{\text{atoms}} \chi_{Wij}^2/(p_j^2\beta_j^2)}{\sum_{j}^{\text{layers}} I_0(d_j, R_j, k_j) \sum_{i}^{\text{atoms}} \chi_{Wij}^2/(p_j^2\beta_j^2)} \tag{A.12}$$

where the analytical solution of integrals I_0 are reported in Eq. A.4. The integral is $I_2(d, D, R, k)$ in case of $k \neq 1,\ 2,\ 3$ and $D = d$ is:

$$I_2(d, d, R, k) = \int_0^d \frac{(d-x)^2}{(1-x/R)^k}\mathrm{d}x = \frac{2R^3(1-d/R)^{3-k} - 2dkR^2 + 6dR^2 - 2R^3}{(k-1)(k-2)(k-3)} - \frac{Rd^2}{k-1} \tag{A.13}$$

When the layer is not the last one, then $D > d$ and the integral becomes:

$$I_2(d, D, R, k) = \int_0^d \frac{(D-x)^2}{(1-x/R)^k} \mathrm{d}x =$$

$$\frac{R(2kDR - 2kdR + 6dR - 6DR)(1-d/R)^{2-k} + 2R^3(1-d/R)^{3-k}}{(k-1)(k-2)(k-3)} +$$

$$+\frac{-2kDR^2 + 6DR^2 - 2R^3}{(k-1)(k-2)(k-3)} + \frac{R(D-d)^2(1-d/R)^{1-k} - RD^2}{k-1} \ , \quad k \neq 1 \qquad \text{(A.14)}$$

The equation A.12 can be evaluated in closed form. Since this formula assumes the multiplication by the final logarithmic factor B, this parameter disappear in the ratio between the two r.m.s.. Therefore, a non-local behavior for z_{esp} is absent. In the case of a single layer, the equation A.12 becomes $z_{\mathrm{esp}} = I_2/I_0$, in agreement with equations of Bellinzona [79]. For a single layer, the result is numerically identical to that of the Fermi-Eyges theory when equations 2.5-2.9 are used in equation 2.13.
The final Molière distribution with all modification for the parameters and with the substitution $\theta \to x/z_{\mathrm{esp}}$, we can write as:

$$f_M(x) = \frac{1}{\pi \chi_c z_{\mathrm{esp}}} \int_0^\infty \cos\left(x \frac{\eta}{\chi_c z_{\mathrm{esp}}}\right) \exp\left[-\frac{\eta^2}{4}\left(b - \ln\frac{\eta^2}{4}\right)\right] \mathrm{d}\eta \qquad \text{(A.15)}$$

The equation A.15 is alternative to the Fermi-Eyges marginal distribution of equation 2.11 and, after the substitution $x/Z_{\mathrm{esp}} \to \theta$, to the angular distribution 2.10.

A.0.1 Comparison with Fermi Eyges theory

We compare the distributions of the two theories in the case of a beam impinging on a multilayer absorber [109] using as a benchmark the Monte Carlo FLUKA code [110] [111].
Since the layers are not independent of each others, if one divides an homogeneous scatterer in different slabs or layers, in principle multiple scattering theories do not give the same result as in the single layer of equal thickness. This effect has called the non locality and mathematically is contained in the logarithmic terms of the Fermi Eyges and Molière theories, in equations 2.8, A.5, A.8.
We have considered a 200 MeV proton beam on 25 cm of water (range of 25.9 cm) and then we have divided this thickness in ten thick layers of 2.5 cm. The results of the crucial parameters of the two theories are compared in table A.1.
We see that in general non local effects are confined below 3%. The Fermi-Eyges values are from equations 2.5, 2.9. When we use equation (2.8) instead of (2.9), we obtain results in agreement within 5% with those of table A.1 for the single layer case and in case of ten layer stack are less of about 15% of those of the single layer case. Therefore, the function 2.8 seems less stable

Fermi-Eyges				Molière			
par	1 layer	10 layers	Δ (%)	par	1 layer	10 layers	Δ (%)
A_0	0.00321	0.00330	3	χ_c	0.0206	0.0203	< 1
A_1	0.0201	0.0202	< 1	χ_α	1.338×10^{-5}	1.314×10^{-5}	2
A_2	0.2624	0.2628	< 1	b	14.52	14.53	< 1
z_{esp}	9.04	8.92	< 1	B	17.38	17.39	< 1
				z_{esp}	8.925	9.041	< 1

Table A.1: Variations (Δ) for the parameters of the Fermi-Eyges and Molière theory for 200 MeV protons in a 25 cm of water and in 10 layers of 2.5 cm each.

than the non-locality of Eq. 2.9.
A comparison between the Molière and Fermi Eyges theory in a stack of different material (for example water and aluminium) at different depth, is shown in figure A.1.

The good agreement between Molière theory and FLUKA is maintained in

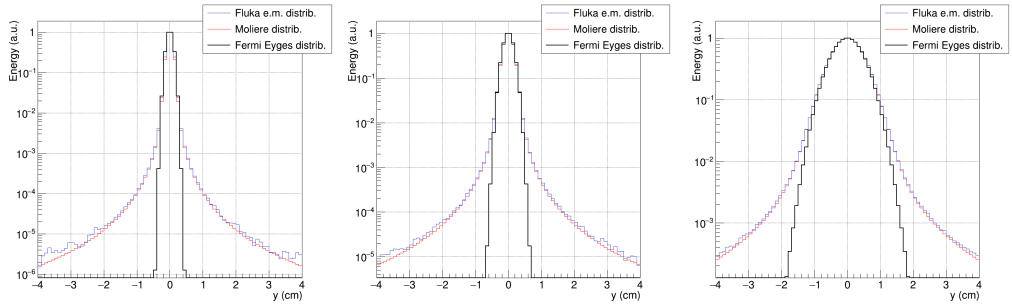

Figure A.1: Lateral e.m. profile of 200 MeV proton point beam in a stack. Left: depth 8cm water. Middle: depth 11 cm (9 cm water + 2 cm aluminium). Right: depth 20 cm (9 cm water + 3 cm aluminium + 8 cm water, residual range in water $\simeq$ 2.6 cm).

the case of a stack. Also in this case the Fermi Eyges theory is in good agreement with Molière and FLUKA in the first two decades, but is not able to reproduce the tails of the distribution.

Appendix B

Lateral profile of ^4He: comparison between Monetα and parametrizations

In this section, we have compared the parametrization currently used for protons and ^{12}C ions [67] [107] [125] [126], with the MONETα results for ^4He beams in water.
The parametrizations considered in this study are [69]:

- Double Gaussian (DG)
  The use of a double Gaussian function to describe the tails of the dose distribution was proposed by R. Fruhwirth and M. Regler [107] and was applied already in clinical TPS [125].

$$f(y) = N\left\{(1-W)\frac{1}{\sqrt{2\pi}\sigma_1}\exp\Big[-\frac{y^2}{2\sigma_1^2}\Big] + W\frac{1}{\sqrt{2\pi}\sigma_2}\exp\Big[-\frac{y^2}{2\sigma_2^2}\Big]\right\}$$

- Triple Gaussian (TG)
  The triple Gaussian was used successfully for ^{12}C ion therapy [126].

$$f(y) = N\Big\{(1-W_1-W_2)\frac{1}{\sqrt{2\pi}\sigma_1}\exp\Big[-\frac{y^2}{2\sigma_1^2}\Big] + W_1\frac{1}{\sqrt{2\pi}\sigma_2}\exp\Big[-\frac{y^2}{2\sigma_2^2}\Big] + W_2\frac{1}{\sqrt{2\pi}\sigma_3}\exp\Big[-\frac{y^2}{2\sigma_3^2}\Big]\Big\}$$

- Gauss-Rutherford (GR)
  The Gauss-Rutherford was an attempt to distinguish the effects of multiple scattering at small angles and of single nuclear scattering at large angles [67]. Recently, this parametrization is applied to ^4He beams in [68].

$$f(y) = N\left\{(1-W)\frac{1}{\sqrt{2\pi}\sigma}\exp\Big[-\frac{y^2}{2\sigma^2}\Big] + W\frac{2b^{3/2}}{\pi}\frac{1}{(y^2+b)^2}\right\}$$

Further details of the parametrization can be found in [67].
To asses the accuracy of the MONETα for the lateral dose profile of ^4He

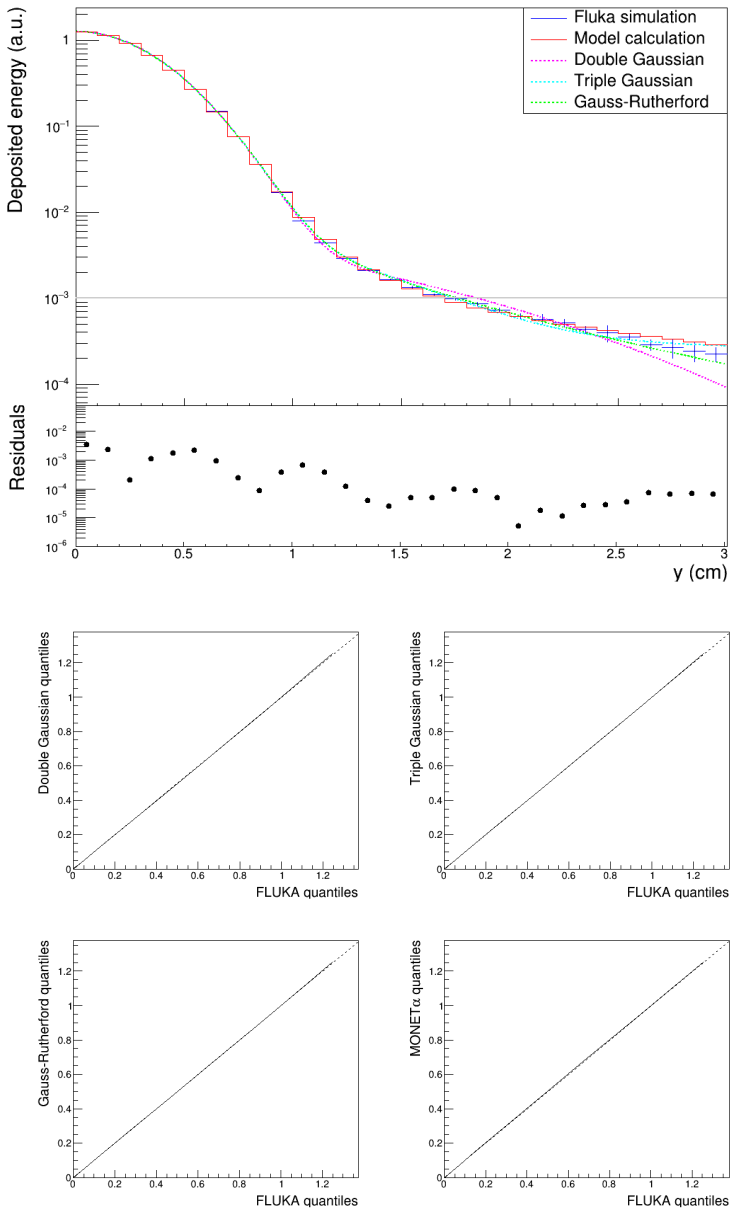

Figure B.1: Energy of 100 MeV/u in water at a depth $z = 7$ cm.
Top: Lateral distribution of Helium beam with the different models. The plotted residuals are calculated between the FLUKA simulation and the model.
Bottom: QQ plot between the MC calculation and different lateral dose profile parametrizations.

beams in water, we have analyzed three different energies (100, 150 and 200 MeV/u) at different depths (7, 10 and 15 cm respectively) and we have com-

pared the model results both with the parametrizations described above and with FLUKA simulations.

The results are reported in figures B.1-B.3. In the lateral distribution, the

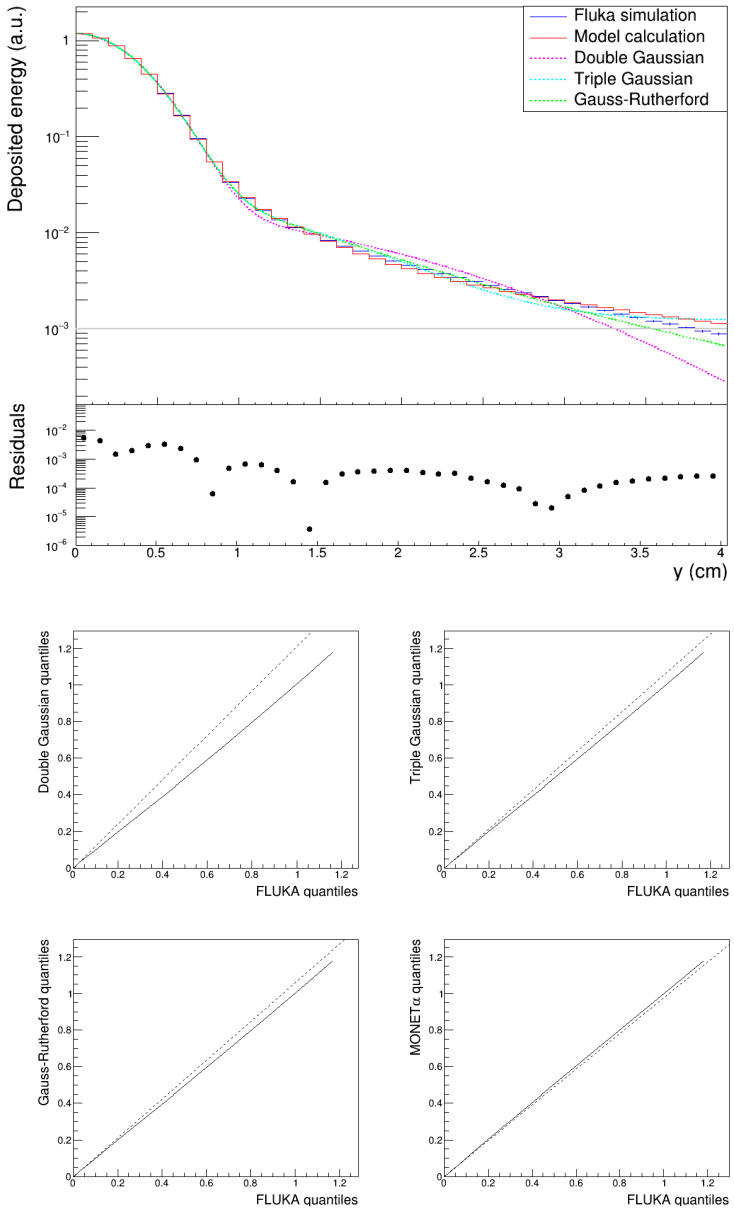

Figure B.2: Energy of 150 MeV/u in water at a depth $z = 10$ cm.
Top: Lateral distribution of Helium beam as in Fig. B.1.
Bottom: QQ plot between the MC calculation and different lateral dose profile parametrizations.

gray line represents the level of 0.1% of the central axis dose: this value is typically considered negligible in terms of clinical significance.

We also plotted the residuals between the model and FLUKA simulation: with the profile normalized to unit area, on the energy scale of figures B.1-B.3, it is important to note that the residuals are in the order of 10^{-2} on the core and of 10^{-4} at increasing of the lateral distance.

We also present the QQ-plot to compare the quantiles of the model and the

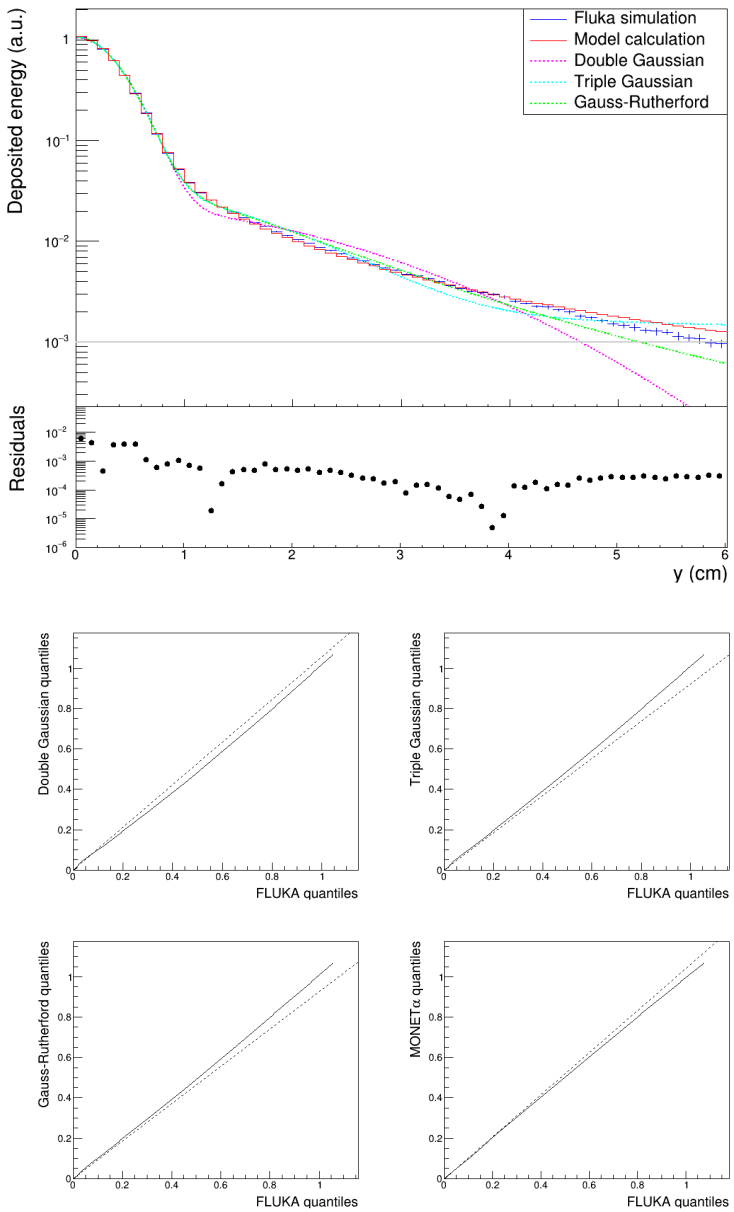

Figure B.3: Energy of 200 MeV/u in water at a depth $z = 15$ cm.
Top: Lateral distribution of Helium beam as in Fig. B.1.
Bottom: QQ plot between the MC calculation and different lateral dose profile parametrizations.

parametrizations with MC distribution. This plot is useful to compare the quantiles of the model and MC distributions showing a 45° line in case of perfect match and allowing to assess the disagreement between MC and a model. We report the values of the average residual between the MC simulation, the parametrizations and the model in Tab. B.1.

	$E = 100$ MeV/u		$E = 150$ MeV/u		$E = 200$ MeV/u	
	4 cm	7 cm	10 cm	15 cm	15 cm	25 cm
DG	0.009	0.009	0.0021	0.0015	0.0029	0.0017
TG	0.005	0.005	0.0011	0.0007	0.0016	0.001
GR	0.003	**0.0004**	0.0009	0.0008	0.0014	0.001
MONETα	**0.003**	0.0005	**0.0008**	**0.0004**	**0.0007**	**0.0005**

Table B.1: Average of the residuals between the MC calculation and different lateral dose profile parametrizations for two depths at energies 100, 150 and 200 MeV/u. In each column the bold figures are the closest to the Monte Carlo simulation.

Looking at the plots B.1-B.3, we have found an agreement with both the model and the three parametrizations. At low energy (100 MeV/u), the model seems to overestimate the MC distribution at large lateral distance, while the multi-Gaussian parametrizations underestimate it. With increasing energy, the agreement improves considerably and we note a good correspondence between the model and the triple Gaussian, but the advantage of the model is that only 3 parameters (compared to the 6 of the Triple Gaussian) are necessary to describe the nuclear contributions.
In the comparison with the parametrizations, the model shows the best agreement with FLUKA at most energies: in particular the accuracy with the Monte Carlo is comparable with the Gauss-Rutherford parametrization at low energy, but improves up to a factor 2 at high energies (looking the Table B.1).
The results of MONETα, based on the Molière theory for multiple scattering and with only 3 parameters for the nuclear contribution, are equivalent or even better than those of the parametrizations. The accuracy of the MONET code motivates its application to treatment planning with ^4He beams.

List of Publications

Articles in peer reviewed international journals

1 - **A. Embriaco**, V. E. Bellinzona, A. Fontana, A. Rotondi, On the lateral dose profile of ^4He beams in water, *Physica Medica*, 40 2017, 51-58

2 - **A. Embriaco**, V. E. Bellinzona, A. Fontana, A. Rotondi, On Molière and Fermi-Eyges scattering theories in hadrontherapy, *Physics in Medicine and Biology*, 62 2017, 6290–6303

3 - **A. Embriaco**, V. E. Bellinzona, A. Fontana, A. Rotondi, An accurate model for the computation of the dose of protons in water, *Physica Medica*, 38 2017, 66-75

4 - V. E. Bellinzona, M. Ciocca, **A. Embriaco**, A. Ferrari, A. Fontana, A. Mairani, K. Parodi, A. Rotondi, P. Sala, T. Tessonnier, A model for the accurate computation of the lateral scattering of protons in water, *Physics in Medicine and Biology*, 61(4) 2016, N102

5 - V. E. Bellinzona, M. Ciocca, **A. Embriaco**, A. Fontana, A. Mairani, M. Mori, K. Parodi, On the parametrization of lateral dose profiles in proton radiation therapy, *Physica Medica*, 31(5) 2015, 484-492

Proceedings

6 - **A. Embriaco**, On the parametrization of lateral dose profiles in proton radiation therapy, *Proceeding of the International Conference on Nuclear Reaction Mechanism 2015*

7 - V. E. Bellinzona, M. Ciocca, **A. Embriaco**, A. Ferrari, A. Fontana, A. Mairani, K. Parodi, A. Rotondi, P. Sala, T. Tessonnier, An analytic solution to lateral dose prediction in Hadrontherapy, *Proceeding of the International Conference on Nuclear Reaction Mechanism 2015*

Abstracts

1 - **A. Embriaco**,V. E. Bellinzona, A. Fontana, A. Rotondi, FLUKA validation of MONET code for dose calculation in Hadrontherapy, *International Conference on Monte Carlo Techniques for Medical Applications , Napoli, Italy, 2017*, Published on Physica Medica 42, 1-50, 2017

2 - G. Battistoni, F. Ballarini, J. Bauer, T. Böhlen, M.P. Carante, F. Cerutti, M. Chin, R. Dos Santos Augusto, A. Fontana, **A. Embriaco**, A. Ferrari, W. Kozlowska, G. Magro, A. Mairani, K. Parodi, P. Ortega, P. Sala, P. Schoofs, T. Tessonier, V. Vlachoudis, The application of the FLUKA Monte Carlo code in medicalphysics, *International conference on Monte-Carlo techniques for medical applications, Napoli, Italy, 2017*, Published on Physica Medica 42, 1-50, 2017

3 - **A. Embriaco**, V. E. Bellinzona, S. Bortolussi, M. El Ais, R. Ferrari, G. Gaudio, I. Postuma, D. Santostasi, M. Torti , S. Venturini, Fisica? Elementare! Esperimenti di fluidodinamica ed elettromagnetismo per incuriosire più di 250 bambini 103° *Congresso Nazionale della Società Italiana di Fisica Trento, Book of abstracts 2017*

4 - **A. Embriaco**, A. Fontana, E. Tiengo, L'aria è un isolante o un conduttore?
Un esperimento didattico sulla ionizzazione dei gas in un tubo a scarica 103° *Congresso Nazionale della Società Italiana di Fisica Trento, Book of abstracts 2017*

5 - **A. Embriaco**,V. E. Bellinzona, A. Fontana, A. Rotondi, A novel approach to dose calculation in Hadrontherapy, 2^{nd} *Italian Society for Radiation Research (SIRR) day, Milano, Italy, 2017*

6 - **A. Embriaco**,V. E. Bellinzona, A. Fontana, A. Rotondi, MONET code for the evaluation of the dose in Hadrontherapy, 8^{th} *Young Researcher Meeting Cagliari, 2017*

7 - **A. Embriaco**,V. E. Bellinzona, A. Fontana, A. Rotondi, MONET: an accurate model for the evaluation of the ion dose in water, *ESTRO (European Society for Radiotherapy and Oncology) 36, Vienna, Austria, 2017*, Published on Radiotherapy and Oncology 123, S781, 2017

8 - V. E. Bellinzona, M. Ciocca, **A. Embriaco**, A. Ferrari, A. Fontana, A. Mairani, K. Parodi, A. Rotondi, P. Sala, T. Tessonnier, Lateral dose profile: a new model, *55th Annual Conference of the Particle Therapy Co-operative Group, Prague, Czech Republic, 2016*

9 - EV Bellinzona, G Landry, A Fontana, **A Embriaco**, A Resch, M Ciocca, A Ferrari, F Kamp, A Mairani, P Sala, T Tessonnier, J Wilkens, A

Rotondi, K Parodi, Implementation of an analytical solution to lateral dose prediction in a proton therapy treatment planning system, *ICTR-PHE 2016*, Published on Radiotherapy and Oncology 118 , S8-S9, 2016

10 - **A. Embriaco**, On the parametrization of lateral dose profiles in proton radiation therapy, *International Conference on Nuclear Reaction Mechanism 2015*

11 - V. E. Bellinzona, M. Ciocca, **A. Embriaco**, A. Ferrari, A. Fontana, A. Mairani, K. Parodi, A. Rotondi, P. Sala, T. Tessonnier, An analytic solution to lateral dose prediction in Hadrontherapy, *International Conference on Nuclear Reaction Mechanism 2015*

Bibliography

[1] Martin Jermann. Particle Therapy Statistics in 2014. *International Journal of Particle Therapy*, 2(1):50–54, 2015.

[2] Emmanouil Fokas, Gerhard Kraft, Hanxiang An, and Rita Engenhart-Cabillic. Ion beam radiobiology and cancer: time to update ourselves. *Biochimica et Biophysica Acta (BBA)-Reviews on Cancer*, 1796(2):216–229, 2009.

[3] H. Paganetti. *Proton Therapy Physics*. CRC Press, 2011.

[4] Marco Durante and Jay S Loeffler. Charged particles in radiation oncology. *Nature reviews Clinical oncology*, 7(1):37–43, 2010.

[5] Nuclear physics for medicine. Nupecc report, 2014.

[6] Jay S Loeffler and Marco Durante. Charged particle therapy optimization, challenges and future directions. *Nature reviews Clinical oncology*, 10(7):411–424, 2013.

[7] Harald Paganetti. Relative biological effectiveness (RBE) values for proton beam therapy. variations as a function of biological endpoint, dose, and linear energy transfer. *Physics in medicine and biology*, 59(22):R419, 2014.

[8] Francesco Tommasino and Marco Durante. Proton radiobiology. *Cancers*, 7(1):353–381, 2015.

[9] Rebecca Grün, Thomas Friedrich, Michael Krämer, Klemens Zink, Marco Durante, Rita Engenhart-Cabillic, and Michael Scholz. Physical and biological factors determining the effective proton range. *Medical physics*, 40(11), 2013.

[10] Drosoula Giantsoudi, Clemens Grassberger, David Craft, Andrzej Niemierko, Alexei Trofimov, and Harald Paganetti. Linear energy transfer-guided optimization in intensity modulated proton therapy: feasibility study and clinical potential. *International Journal of Radiation Oncology Biology Physics*, 87(1):216–222, 2013.

[11] Minna Wedenberg and Iuliana Toma-Dasu. Disregarding RBE variation in treatment plan comparison may lead to bias in favor of proton plans. *Medical physics*, 41(9), 2014.

[12] Bleddyn Jones. Towards achieving the full clinical potential of proton therapy by inclusion of let and rbe models. *Cancers*, 7(1):460–480, 2015.

[13] Fada Guan, Lawrence Bronk, Uwe Titt, Steven H Lin, Dragan Mirkovic, Matthew D Kerr, X Ronald Zhu, Jeffrey Dinh, Mary Sobieski, Clifford Stephan, et al. Spatial mapping of the biologic effectiveness of scanned particle beams: towards biologically optimized particle therapy. *Scientific reports*, 5, 2015.

[14] Michael Krämer and Michael Scholz. Treatment planning for heavy-ion radiotherapy: calculation and optimization of biologically effective dose. *Physics in Medicine and Biology*, 45(11):3319, 2000.

[15] Mario P Carante and Francesca Ballarini. Modelling cell death for cancer hadrontherapy. 2017.

[16] Taku Inaniwa, Nobuyuki Kanematsu, Naruhiro Matsufuji, Tatsuaki Kanai, Toshiyuki Shirai, Koji Noda, Hiroshi Tsuji, Tadashi Kamada, and Hirohiko Tsujii. Reformulation of a clinical-dose system for carbon-ion radiotherapy treatment planning at the national institute of radiological sciences, japan. *Physics in medicine and biology*, 60(8):3271, 2015.

[17] Francesco Tommasino, Emanuele Scifoni, and Marco Durante. New ions for therapy. *International Journal of Particle Therapy*, 2(3):428–438, 2015.

[18] Marta Rovituso and Chiara La Tessa. Nuclear interactions of new ions in cancer therapy: impact on dosimetry. *Translational Cancer Research*, 6(S5):S914–S933, 2017.

[19] Joseph R Castro, Jeanne M Quivey, John T Lyman, George TY Chen, Theodore L Phillips, Cornelius A Tobias, and Edward L Alpen. Current status of clinical particle radiotherapy at Lawrence Berkeley Laboratory. *Cancer*, 46(4):633–641, 1980.

[20] JR Castro, JM Quivey, WM Saunders, KH Woodruff, GTY Chen, JT Lyman, S Pitluck, CA Tobias, RE Walton, and TC Peters. Clinical results in heavy particle radiotherapy. Technical report, 1980.

[21] Devron H Char, Stewart M Kroll, and Joseph Castro. Ten-year follow-up of helium ion therapy for uveal melanoma. *American journal of ophthalmology*, 125(1):81–89, 1998.

[22] Joseph R Castro, David E Linstadt, Jean-Paul Bahary, Paula L Petti, Inder Daftari, J Michael Collier, Philip H Gutin, Grant Gauger, and Theodore L Phillips. Experience in charged particle irradiation of tumors of the skull base: 1977–1992. *International Journal of Radiation Oncology Biology Physics*, 29(4):647–655, 1994.

[23] Eleanor A Blakely, IK Daftari, WJ Meecham, LC Alonso, JM Collier, SM Kroll, EL Gillette, AC Lee, JT Lett, AB Cox, et al. Helium-ion-induced human cataractogenesis. *Advances in Space Research*, 14(10):501–505, 1994.

[24] Barbara Knäusl, Hermann Fuchs, Karin Dieckmann, and Dietmar Georg. Can particle beam therapy be improved using helium ions? A planning study focusing on pediatric patients. *Acta Oncologica*, 55(6):751–759, 2016.

[25] M Rovituso, C Schuy, U Weber, S Brons, MA Cortés-Giraldo, C La Tessa, E Piasetzky, D Izraeli, D Schardt, M Toppi, et al. Fragmentation of 120 and 200 MeV/u ^4He ions in water and pmma targets. *Physics in Medicine and Biology*, 62(4):1310, 2017.

[26] Uli Weber and Gerhard Kraft. Comparison of carbon ions versus protons. *The Cancer Journal*, 15(4):325–332, 2009.

[27] Rebecca Grün, Thomas Friedrich, Michael Krämer, Klemens Zink, Marco Durante, Rita Engenhart-Cabillic, and Michael Scholz. Assessment of potential advantages of relevant ions for particle therapy: a model based study. *Medical physics*, 42(2):1037–1047, 2015.

[28] Julia Ströbele, Thomas Schreiner, Hermann Fuchs, and Dietmar Georg. Comparison of basic features of proton and helium ion pencil beams in water using gate. *Zeitschrift für Medizinische Physik*, 22(3):170–178, 2012.

[29] Johanna Kempe, Irena Gudowska, and Anders Brahme. Depth absorbed dose and LET distributions of therapeutic ^1H, ^4He, ^7Li, and ^{12}C beams. *Medical physics*, 34(1):183–192, 2007.

[30] MR Raju, HI Amols, E Bain, SG Carpenter, RA Cox, and JB Robertson. A heavy particle comparative study. part iii: OER and RBE. *The British journal of radiology*, 51(609):712–719, 1978.

[31] Alberto Fassó, Alfredo Ferrari, PR Sala, and J Ranft. Fluka: Status and prospects for hadronic applications. In *Advanced Monte Carlo for Radiation Physics, Particle Transport Simulation and Applications*, pages 955–960. Springer, 2001.

[32] Sea Agostinelli, John Allison, K al Amako, J Apostolakis, H Araujo, P Arce, M Asai, D Axen, S Banerjee, G Barrand, et al. Geant4—a simulation toolkit. *Nuclear instruments and methods in physics research section A: Accelerators, Spectrometers, Detectors and Associated Equipment*, 506(3):250–303, 2003.

[33] Laurie S Waters et al. Mcnpx user's manual. *Los Alamos.(Accesed in Apr 15, 2012 at http://mcnpx. lanl. gov/opendocs/versions/v230/MCNPX_2. 3.0 _Manual. pdf)*, 2002.

[34] Koji Niita, Tatsuhiko Sato, Hiroshi Iwase, Hiroyuki Nose, Hiroshi Nakashima, and Lembit Sihver. PHITS A particle and heavy ion transport code system. *Radiation measurements*, 41(9):1080–1090, 2006.

[35] Harald Paganetti, Hongyu Jiang, Katia Parodi, Roelf Slopsema, and Martijn Engelsman. Clinical implementation of full monte carlo dose calculation in proton beam therapy. *Physics in medicine and biology*, 53(17):4825, 2008.

[36] L Grevillot, D Bertrand, F Dessy, N Freud, and D Sarrut. A monte carlo pencil beam scanning model for proton treatment plan simulation using gate/geant4. *Physics in Medicine and Biology*, 56(16):5203, 2011.

[37] K Parodi, A Mairani, S Brons, J Naumann, F Sommerer, and T Haberer. The application of the FLUKA monte carlo code to basic data generation for clinical treatment planning of scanned proton and carbon ion therapy. In *Second European Workshop on Monte Carlo Treatment Planning*, 2009.

[38] Katia Parodi, Andrea Mairani, Stephan Brons, BG Hasch, Florian Sommerer, J Naumann, Oliver Jäkel, Thomas Haberer, and Jürgen Debus. Monte carlo simulations to support start-up and treatment planning of scanned proton and carbon ion therapy at a synchrotron-based facility. *Physics in medicine and biology*, 57(12):3759, 2012.

[39] JS Li, B Shahine, E Fourkal, and CM Ma. A particle track-repeating algorithm for proton beam dose calculation. *Physics in medicine and biology*, 50(5):1001, 2005.

[40] A Tourovsky, AJ Lomax, U Schneider, and E Pedroni. Monte carlo dose calculations for spot scanned proton therapy. *Physics in medicine and biology*, 50(5):971, 2005.

[41] Matthias Fippel and Martin Soukup. A monte carlo dose calculation algorithm for proton therapy. *Medical physics*, 31(8):2263–2273, 2004.

[42] Xun Jia, Xuejun Gu, Yan Jiang Graves, Michael Folkerts, and Steve B Jiang. GPU-based fast monte carlo simulation for radiotherapy dose calculation. *Physics in medicine and biology*, 56(22):7017, 2011.

[43] Xun Jia, Jan Schümann, Harald Paganetti, and Steve B Jiang. GPU-based fast monte carlo dose calculation for proton therapy. *Physics in medicine and biology*, 57(23):7783, 2012.

[44] Xun Jia, Todd Pawlicki, Kevin T Murphy, and Arno J Mundt. Proton therapy dose calculations on gpu: advances and challenges. *Translational Cancer Research*, 1(3):207–216, 2012.

[45] Xun Jia, Peter Ziegenhein, and Steve B Jiang. GPU-based high-performance computing for radiation therapy. *Physics in medicine and biology*, 59(4):R151, 2014.

[46] Joakim Da Silva, Richard Ansorge, and Rajesh Jena. Sub-second pencil beam dose calculation on GPU for adaptive proton therapy. *Physics in medicine and biology*, 60(12):4777, 2015.

[47] A Mairani, Till Tobias Böhlen, A Schiavi, T Tessonnier, S Molinelli, S Brons, G Battistoni, K Parodi, and V Patera. A monte carlo-based treatment planning tool for proton therapy. *Physics in medicine and biology*, 58(8):2471, 2013.

[48] Till Tobias Böhlen, J Bauer, M Dosanjh, A Ferrari, T Haberer, K Parodi, V Patera, and A Mairani. A monte carlo-based treatment-planning tool for ion beam therapy. *Journal of radiation research*, 54(1):i77–i81, 2013.

[49] Linda Hong, Michael Goitein, Marta Bucciolini, Robert Comiskey, Bernard Gottschalk, Skip Rosenthal, Chris Serago, and Marcia Urie. A pencil beam algorithm for proton dose calculations. *Physics in medicine and biology*, 41(8):1305, 1996.

[50] Kenneth R Hogstrom, Michael D Mills, and Peter R Almond. Electron beam dose calculations. *Physics in medicine and biology*, 26(3):445, 1981.

[51] J Schwaab, Stephan Brons, J Fieres, and Katia Parodi. Experimental characterization of lateral profiles of scanned proton and carbon ion pencil beams for improved beam models in ion therapy treatment planning. *Physics in medicine and biology*, 56(24):7813, 2011.

[52] Michael Krämer, Oliver Jäkel, Thomas Haberer, Gerhard Kraft, Dieter Schardt, and Uli Weber. Treatment planning for heavy-ion radiotherapy: physical beam model and dose optimization. *Physics in Medicine and Biology*, 45(11):3299, 2000.

[53] T. Bortfeld. An analytical approximation of the bragg curve for therapeutic proton beams. *Medical Physics*, 24(12):2024–33, 1997.

[54] Barbara Schaffner, Eros Pedroni, and Antony Lomax. Dose calculation models for proton treatment planning using a dynamic beam delivery

system: an attempt to include density heterogeneity effects in the analytical dose calculation. *Physics in medicine and biology*, 44(1):27, 1999.

[55] B Gottschalk, AM Koehler, RJ Schneider, JM Sisterson, and MS Wagner. Multiple coulomb scattering of 160 MeV protons. *Nuclear Instruments and Methods in Physics Research Section B: Beam Interactions with Materials and Atoms*, 74(4):467–490, 1993.

[56] Michael Lee, AE Nahum, and Steve Webb. An empirical method to build up a model of proton dose distribution for a radiotherapy treatment-planning package. *Physics in Medicine and Biology*, 38(7):989, 1993.

[57] A. Carlsson, P. Andreo, and A. Brahme. Monte carlo and analytical calculation of proton pencil beams for computerized treatment plan optimization. *Phys. Med. Bio.*, 42(6):1033, 1997.

[58] A Brahme, I Lax, and P Andreo. Electron beam dose planning using discrete gaussian beams: mathematical background. *Acta Radiologica: Oncology*, 20(2):147–158, 1981.

[59] David Jette. Electron dose calculation using multiple-scattering theory. a. gaussian multiple-scattering theory. *Medical physics*, 15(2):123–137, 1988.

[60] Paula L Petti. Differential-pencil-beam dose calculations for charged particles. *Medical physics*, 19(1):137–149, 1992.

[61] Kellie R Russell, Ulf Isacsson, Mikael Saxner, Anders Ahnesjö, Anders Montelius, Erik Grusell, Christina Vallhagen Dahlgren, Stefan Lorin, and Bengt Glimelius. Implementation of pencil kernel and depth penetration algorithms for treatment planning of proton beams. *Physics in medicine and biology*, 45(1):9, 2000.

[62] H Szymanowski, A Mazal, C Nauraye, S Biensan, R Ferrand, MC Murillo, S Caneva, G Gaboriaud, and JC Rosenwald. Experimental determination and verification of the parameters used in a proton pencil beam algorithm. *Medical physics*, 28(6):975–987, 2001.

[63] Malin Hollmark, Johan Uhrdin, Dž Belkić, Irena Gudowska, and Anders Brahme. Influence of multiple scattering and energy loss straggling on the absorbed dose distributions of therapeutic light ion beams: I. analytical pencil beam model. *Physics in medicine and biology*, 49(14):3247, 2004.

[64] Gabriel O Sawakuchi, Uwe Titt, Dragan Mirkovic, George Ciangaru, X Ronald Zhu, Narayan Sahoo, Michael T Gillin, and Radhe Mohan. Monte carlo investigation of the low-dose envelope from scanned proton pencil beams. *Physics in medicine and biology*, 55(3):711, 2010.

[65] E Pedroni, S Scheib, T Böhringer, A Coray, M Grossmann, S Lin, and A Lomax. Experimental characterization and physical modelling of the dose distribution of scanned proton pencil beams. *Physics in medicine and biology*, 50(3):541, 2005.

[66] Joakim da Silva, Richard Ansorge, and Rajesh Jena. Fast pencil beam dose calculation for proton therapy using a double-gaussian beam model. *Frontiers in oncology*, 5, 2015.

[67] V.E. E Bellinzona, M. Ciocca, A. Embriaco, A. Fontana, A. Mairani, M. Mori, et al. On the parametrization of lateral dose profiles in proton radiation therapy. *Phys. Med.*, 31(5):1–9, 2015.

[68] Marta Rovituso. *Fragmentation and lateral scattering of 120 and 200 MeV/u ^4He ions on water targets*. PhD thesis, Technische Universität Darmstadt, Darmstadt, April 2016.

[69] A. Embriaco, V.E. Bellinzona, A. Fontana, and A. Rotondi. On the lateral dose profile of 4he beams in water. *Physica Medica*, 40:51 – 58, 2017.

[70] Hermann Fuchs, Julia Ströbele, Thomas Schreiner, Albert Hirtl, and Dietmar Georg. A pencil beam algorithm for helium ion beam therapy. *Medical physics*, 39(11):6726–6737, 2012.

[71] Bernard Gottschalk. On the scattering power of radiotherapy protons. *Medical physics*, 37(1):352–367, 2010.

[72] M. Krämer and M. Durante. Ion beam transport calculations and treatment plans in particle therapy. *Eur. Phys. Jour. D.*, 60(1):195–202, 2010.

[73] Michael Krämer and Michael Scholz. Treatment planning for heavy-ion radiotherapy: calculation and optimization of biologically effective dose. *Physics in Medicine and Biology*, 45(11):3319, 2000.

[74] M Krämer, O Jäkel, T Haberer, E Rietzel, D Schardt, M Scholz, JF Wang, U Weber, and W Weyrather. Treatment planning for scanned ion beams. *Radiotherapy and Oncology*, 73:S80–S85, 2004.

[75] Michael Krämer, Emanuele Scifoni, Christoph Schuy, Marta Rovituso, Walter Tinganelli, Andreas Maier, Robert Kaderka, Wilma Kraft-Weyrather, Stephan Brons, Thomas Tessonnier, et al. Helium ions for radiotherapy? physical and biological verifications of a novel treatment modality. *Medical Physics*, 43(4):1995–2004, 2016.

[76] Christoph Bert and Eike Rietzel. 4d treatment planning for scanned ion beams. *Radiation Oncology*, 2(1):24, 2007.

[77] T. Tessonnier, A. Mairani, S. Brons, T. Haberer, J. Debus, and K. Parodi. Experimental dosimetric comparison of 1h, 4he, 12c and 16o scanned ion beams. *Physics in Medicine and Biology*, 62(10):3958, 2017.

[78] A Embriaco, VE Bellinzona, A Fontana, and A Rotondi. An accurate model for the computation of the dose of protons in water. *Physica Medica*, 38:66–75, 2017.

[79] E. V. Bellinzona, M. Ciocca, A. Embriaco, A. Ferrari, A. Fontana, Mairani, et al. A model for the accurate computation of the lateral scattering of protons in water. *Phys. Med. Bio.*, 61(4):N102–17, 2016.

[80] A. Papoulis. Joint densities with circular symmetry (corresp.). *IEEE Trans. on Inf. Theo.*, 14(1):164–65, 1968.

[81] J. Kempe and A. Brahme. Energy-range relation and mean energy variation in therapeutic particle beams. *Medical Physics*, 35(1):159–70, 2008.

[82] Bernard Gottschalk. Techniques of proton radiotherapy: transport theory. *arXiv preprint arXiv:1204.4470*, 2012.

[83] B. Gottschalk, E. W. Cascio, J. Daartz, and M. S. Wagner. On the nuclear halo of a proton pencil beam stopping in water. *Phys. Med. Bio.*, 60(14):5627, 2015.

[84] F. Van den Heuvel, F. Fiorini, N. Schreuder, and B. George. Using stable distributions to characterize proton pencil beams. *arXiv:1611.08871*, 2016.

[85] HA Bethe. Moliere's theory of multiple scattering. *Physical Review*, 89(6):1256, 1953.

[86] G Bendiscioli, E Lodi Rizzini, and A Rotondi. Coulomb multiple-scattering analysis in the presence of nuclear effects. *Il Nuovo Cimento A (1971-1996)*, 48(3):369–385, 1978.

[87] G Bendiscioli, E Lodi Rizzini, A Rotondi, and A Venaglioni. Coulomb multiple scattering of heavy particles. *Il Nuovo Cimento A (1971-1996)*, 68(2):101–122, 1982.

[88] AM Cormack. The effects of multiple scattering in small-angle nuclear scattering experiments. *Nuclear Physics*, 52:286–300, 1964.

[89] Gert Moliere. Theorie der streuung schneller geladener teilchen ii mehrfach-und vielfachstreuung. *Zeitschrift für Naturforschung A*, 3(2):78–97, 1948.

[90] Hartland S Snyder and William Taussig Scott. Multiple scattering of fast charged particles. *Physical Review*, 76(2):220, 1949.

[91] William T Scott. Correlated probabilities in multiple scattering. *Physical Review*, 76(2):212, 1949.

[92] William T Scott. Mean-value calculations for projected multiple scattering. *Physical Review*, 85(2):245, 1952.

[93] William T Scott. The theory of small-angle multiple scattering of fast charged particles. *Reviews of modern physics*, 35(2):231, 1963.

[94] Saunderson Goudsmit and JL Saunderson. Multiple scattering of electrons. *Physical Review*, 57(1):24, 1940.

[95] HW Lewis. Multiple scattering in an infinite medium. *Physical review*, 78(5):526, 1950.

[96] Leonard Eyges. Multiple scattering with energy loss. *Physical Review*, 74(10):1534, 1948.

[97] Bruno Benedetto Rossi. High-energy particles. 1952.

[98] Nobuyuki Kanematsu. Semi-empirical formulation of multiple scattering for the gaussian beam model of heavy charged particles stopping in tissue-like matter. *Physics in medicine and biology*, 54(5):N67, 2009.

[99] Martin Soukup, Matthias Fippel, and Markus Alber. A pencil beam algorithm for intensity modulated proton therapy derived from monte carlo simulations. *Physics in medicine and biology*, 50(21):5089, 2005.

[100] E Pedroni, S Scheib, T Böhringer, A Coray, M Grossmann, S Lin, and A Lomax. Experimental characterization and physical modelling of the dose distribution of scanned proton pencil beams. *Physics in medicine and biology*, 50(3):541, 2005.

[101] Takeshi Mukoyama and Yoshihisa Watanabe. A monte-carlo method for calculations of the distribution of. *Bull. Inst. Chem. Res., Kyoto Univ*, 56(1), 1978.

[102] George B Arfken and Hans J Weber. *Mathematical methods for physicists international student edition*. Academic press, 2005.

[103] Helge Øverås. On small-angle multiple scattering in confined bodies. Technical report, CERN, 1960.

[104] U Schneider, J Besserer, and P Pemler. On small angle multiple coulomb scattering of protons in the gaussian approximation. *Zeitschrift für Medizinische Physik*, 11(2):110–118, 2001.

[105] U Fano. Inelastic collisions and the moliere theory of multiple scattering. *Physical Review*, 93(1):117, 1954.

[106] W. Ulmer and B. Schaffner. Foundation of an analytical proton beamlet model for inclusion in a general proton dose calculation system. *Radiation Physics and Chemistry*, 80(3):378–89, 2011.

[107] R. Frühwirth and M. Regler. On the quantitative modelling of core and tails of multiple scattering by gaussian mixtures. *Nuc. Instr. Meth. Phys. Res. A*, 456(3):369–89, 2001.

[108] G. Amsel, G. Battistig, and A. L'Hoir. Small angle multiple scattering of fast ions, physics, stochastic theory and numerical calculations. *Nuc. Instr. Meth. Phys. Res. B*, 201(2):325 – 88, 2003.

[109] A Embriaco, EV Bellinzona, A Fontana, and A Rotondi. On Molière and Fermi–Eyges scattering theories in hadrontherapy. *Phys. Med. Biol*, 62:6290–6303, 2017.

[110] Alfredo Ferrari, Paola R Sala, Alberto Fasso, and Johannes Ranft. FLUKA: a multi-particle transport code (program version 2005). Technical report, 2005.

[111] TT Böhlen, F Cerutti, MPW Chin, Alberto Fassò, Alfredo Ferrari, PG Ortega, Andrea Mairani, Paola R Sala, G Smirnov, and V Vlachoudis. The FLUKA code: developments and challenges for high energy and medical applications. *Nuclear Data Sheets*, 120:211–214, 2014.

[112] A Ferrari, PR Sala, R Guaraldi, and F Padoani. An improved multiple scattering model for charged particle transport. *Nuclear Instruments and Methods in Physics Research Section B: Beam Interactions with Materials and Atoms*, 71(4):412–426, 1992.

[113] A Fasso, A Ferrari, J Ranft, and PR Sala. An update about fluka. In *Proc. 2nd workshop on Simulating Accelerator Radiation Environment, SARE-2, CERN-Geneva*, pages 9–11, 1995.

[114] T Goorley, M James, T Booth, F Brown, J Bull, LJ Cox, J Durkee, J Elson, M Fensin, RA Forster, et al. Initial mcnp6 release overview. *Nuclear Technology*, 180(3):298–315, 2012.

[115] Yupeng Li, Ronald X Zhu, Narayan Sahoo, Aman Anand, and Xiaodong Zhang. Beyond gaussians: a study of single-spot modeling for scanning proton dose calculation. *Physics in medicine and biology*, 57(4):983, 2012.

[116] Bernard Gottschalk, Ethan W Cascio, Juliane Daartz, and Miles S Wagner. Nuclear halo of a 177 mev proton beam in water: theory, measurement and parameterization. *arXiv preprint arXiv:1409.1938*, 2014.

[117] Stephen M Seltzer. An assessment of the role of charged secondaries from nonelastic nuclear interactions by therapy proton beams in water. *NIST Interagency/Internal Report (NISTIR)-*, 1993.

[118] T. Tessonnier. *Treatment of low-grade meningiomas with protons and helium ions*. PhD thesis, 2017.

[119] William H Press. *Numerical recipes 3rd edition: The art of scientific computing*. Cambridge university press, 2007.

[120] M. B. WILK and R. GNANADESIKAN. Probability plotting methods for the analysis for the analysis of data. *Biometrika*, 55(1):1–17, 1968.

[121] Alberto Rotondi, Paolo Pedroni, and Antonio Pievatolo. *Probabilità statistica e simulazione: programmi applicativi scritti con Scilab*. Springer Science & Business Media, 2006.

[122] L. Grevillot, D. Bertrand, F. Dessy, N. Freud, and D. Sarrut. A monte carlo pencil beam scanning model for proton treatment plan simulation using gate/geant4. *Phys. Med. Bio.*, 56(16):5203, 2011.

[123] G. Sawakuchi, X. R. Zhu, F. Poenisch, K. Suzuki, G. Ciangaru, U. Titt, et al. Experimental characterization of the low-dose envelope of spot scanning proton beams. *Phys. Med. Bio.*, 55(12):3467, 2010.

[124] Virgil L Highland. Some practical remarks on multiple scattering. *Nuclear Instruments and Methods*, 129(2):497–499, 1975.

[125] K. Parodi, A. Mairani, and F. Sommerer. Monte carlo-based parametrization of the lateral dose spread for clinical treatment planning of scanned proton and carbon ion beams. *Jour. of Rad. Res.*, 54(suppl 1):i91–96, 2013.

[126] T. Inaniwa, N. Kanematsu, Y. Hara, T. Furukawa, M. Fukahori, M. Nakao, et al. Implementation of a triple gaussian beam model with subdivision and redefinition against density heterogeneities in treatment planning for scanned carbon-ion radiotherapy. *Phys. Med. and Bio.*, 59(18):5361, 2014.

Acknowledgements

This project was partially supported by the Institute of Nuclear Physics (INFN) and MC-INFN project.
I would like to thanks Dr. Francesca Fiorini and Prof. Paolo Russo, who were the referees of my thesis, for their helpfull commments.
The experimental data taken at HIT and the phasespace input file for the simulation have been kindly provided by Jürgen Debus, Katia Parodi, Thomas Tessonnier and Andrea Mairani.
I would like to thanks Alfredo Ferrari and Paola Sala for their helpfull comments on the Monte Carlo simulation.
Il primo ringraziamento va al mio relatore, Alberto Rotondi, che mi ha dato l'opportunità di intraprendere questa tesi. Grazie ad Andrea Fontana per la sua disponibilità e il supporto in ogni singolo passo di questa tesi. Vi ringrazio per tutto ciò che mi avete insegnato, ma soprattutto per la vostra contagiosa passione.
Un ringraziamento speciale va ad Elettra con cui ho iniziato questo percorso, per il suo aiuto e la sua positività.
Grazie mille a Francesca per avermi adottato nel suo ufficio, per il suo supporto e i suoi consigli. Grazie a Mario per aver reso divertenti e ricche di sorprese le nostre trasferte. Potrei fare un appendice ricca di aneddoti, ma abbiamo una reputazione da difendere.
Grazie a tutti miei compagni di dottorato e ai nostri aperitivi. Un ringraziamento speciale a Seta e Barbara, con cui ho condiviso weekend estivi in dipartimento a scrivere la tesi, anche se ricordo più volentieri la nostra trasferta passata tra Monte Carlo e spiaggia ad Alghero.
Grazie anche ai colleghi dello studio della BNCT, a Nico coautrice di numerosi progetti più o meno scientifici, a Ian e la sua macchinetta del caffè.
Un grazie speciale va a Gabri, Silva, Andrea e Valerio per avermi coivolto/incastrato nella realizzazione della Notte dei Ricercatori e in altri progetti di divulgazione, ma soprattutto grazie per la vostra fiducia.
The last but not the least... Grazie ai colleghi della pausa pranzo Claudio, Alessandro, Francesco, Nicolò, Francesca e Nico, che con gli innumerevoli pranzi insiemi a base di fisica, barzellette, nerdaggini varie e dolcetti hanno

reso le lunghe giornate di lavoro più allegre. Vi ringrazio per avermi fatto sentire parte di un gruppo (di pazzi, ma questo poco importa).
Grazie ai compagni di studio pavesi e ai figli del Radon, che piano piano hanno scalato la classifica del torneo di pallavolo.
Un ringraziamento speciale va a Serena, compagna di corso e di trasferte (degna di nota è la scelta dello stesso hotel senza neanche discuterne insieme...queste sono affinità elettive!).
Grazie alla squadra dei Diodi: Livia, Ges e Ila, Arri e Impe, che con il nostro appuntamento settimanale hanno riempito di simpatia anche le fredde serate invernali.
Grazie ai canoisti del CUS, in particolar modo a Livia, ad Antonio per le chiacchierate sulla idrodinamicità della canoa e a Ivo per gli innumerevoli giri in canoa.
Ho iniziato a studiare fisica a Genova dove mi sono trovata bene grazie alla simpatia dei ragazzi del DIFI, tra tutti in particolar modo a Fox, Coppe, Marcocci, Lollo, Ruben, Marzia e i Ventu: Andre e Fede.
Grazie alla tenera Simonetta Parodi, compagna di palestra e chiacchiere.
Un grazie speciale va a Vale e Ila con le quali ho condiviso molti momenti: dallo studio disperato agli aperitivi. Grazie ragazze per la vostra amicizia!
Infine, i ringraziamenti agli amici di vecchia di vecchia data di Sanremo, che anche se ultimamente torno raramente, riescono sempre a farmi sentire a casa.
Un affettuoso grazie a tutti gli amici di canoa, con i quali son cresciuta.
Un super grazie alle mie vecchie amiche Gemma e Fede: anche se ultimamente ci vediamo poco, siamo sempre rimaste vicine.
Grazie alla mia amica Guè, vecchia amica del liceo, che anche se la vedo pochissimo, sembra che ci siamo viste ieri.
Un grazie speciale al mio amico Avv. Nicolò, che tutte le volte che torno mi offre un caffè e quattro chiacchiere.
Grazie alla Clem per nostre birre a Soldano.
Infine un grazie speciale va a Marco per tutto, ma soprattutto per aver creduto in me!
Questo risultato non sarebbe stato possibile senza il supporto della mia famiglia.
Grazie Mamma per non aver mai messo in dubbio le mie scelte, per la continua fiducia in me e per tutte volte in cui mi hai detto di non essere troppo severa con me stessa.
Grazie ad Amanda, la mia sorellina, che mi conosce meglio di chiunque altro.
Grazie ad entrambe per essermi state vicine nonostante la lontananza da casa.
E infine grazie Papà per tutto quello che mi hai insegnato e per i nostri momenti insieme. Questa tesi la dedico a te.